

FUSION OF LANDSAT-7, IRS-1D AND RADARSAT-1 DATA
FOR FLOOD DELINEATION

By

SIRIPON KAMONTUM

A DISSERTATION PRESENTED TO THE GRADUATE SCHOOL
OF THE UNIVERSITY OF FLORIDA IN PARTIAL FULFILLMENT
OF THE REQUIREMENTS FOR THE DEGREE OF
DOCTOR OF PHILOSOPHY

UNIVERSITY OF FLORIDA

2009

© 2009 Siripon Kamontum

To my family

ACKNOWLEDGMENTS

My dissertation would not have been possible without kindly guidance and supervision of my advisor, Dr. Scot Smith and the rest of my advisory committee members: Dr. Bon Dewitt, Dr. Grenville Barnes, Dr. Amr Abd-Elrahman and Dr. Kirk Hatfield who always dedicated their precious time to educate me and gave me critical comments. I am truly grateful.

My continued gratitude to organizations in Thailand who supplied data for my study: Geo-informatics and Space Technology Development Agency (GISTDA), Computer Center of Khon Kaen University, Royal Irrigation Department, and Department of Environmental Quality Promotion. Thanks to the Royal Thai Government and GISTDA for giving me an opportunity to pursue my PhD degree.

Special thanks to my friends and family for all supports. Huge thanks to my husband, Ped, for his unceasing love and support.

TABLE OF CONTENTS

	<u>page</u>
ACKNOWLEDGMENTS	4
LIST OF TABLES	7
LIST OF FIGURES	8
ABSTRACT.....	10
CHAPTER	
1 INTRODUCTION	12
Problem Statement.....	12
Objectives	15
Study Area	15
2 LITERATURE REVIEW	18
Image Fusion Techniques	18
Principal Component Analysis	18
Intensity-Hue-Saturation	19
Flood Assessment Using Remote Sensing	21
Landsat	21
IRS	27
Radarsat	30
Flood Models	36
Flood Models and Remote Sensing	41
3 MATERIALS AND METHODS	53
Spatial Data.....	53
Satellite Imageries	53
GIS Data	54
Hydrological Data and HEC-RAS Model	55
Data Preprocessing	55
Speckle Noise Suppression.....	56
Geometric Correction	57
HEC-RAS Data Preparation	58
Data Analysis.....	59
Calculation of Water Surface Elevation Using HEC-RAS	59
Radarsat Image Interpretation	61
PCA	62
Pan-sharpening	62
Classification of Fused Image	63

4	RESULTS	72
	HEC-RAS and HEC-GeoRAS Results	72
	Flood Maps Interpreted from Radarsat Images	72
	Comparison of Radarsat Flood Maps Referencing HEC-RAS Flood Map.....	72
	PCA Results.....	74
	Fused Image and Its Classification	75
	Comparison of Flood Maps from Fused Image and Best Radarsat Image	77
	Underwater Feature Detection.....	79
5	DISCUSSION.....	94
	Flood Prediction Using HEC-RAS.....	94
	Radarsat W1 versus Radarsat S7	95
	The Fused Image.....	96
6	CONCLUSIONS	100
	REFERENCES	103
	BIOGRAPHICAL SKETCH	112

LIST OF TABLES

<u>Table</u>	<u>page</u>
2-1	Sensors and bands of Landsat-1 to 7.....52
2-2	Description of Radarsat imaging modes.....52
3-1	RMS residual errors of the GCPs.....71
3-2	Estimated Manning's n values.....71
4-1	Error matrix of classification of Radarsat W1 image91
4-2	Accuracy totals of classification of Radarsat W1 image91
4-3	Kappa statistics of classification of Radarsat W1 image91
4-4	Error matrix of classification of Radarsat S7 image.....91
4-5	Accuracy totals of classification of Radarsat S7 image.....91
4-6	Kappa statistics of classification of Radarsat S7 image.....91
4-7	Eigen values and eigen vectors.....92
4-8	Percentage of total scene variance92
4-9	Error matrix of flood map interpreted from Radarsat S7 image.....93
4-10	Accuracy totals of flood map interpreted from Radarsat S7 image.....93
4-11	Kappa statistics of flood map interpreted from Radarsat S7 image.....93
4-12	Error matrix of flood map interpreted from fused image93
4-13	Accuracy totals of flood map interpreted from fused image93
4-14	Kappa statistics of flood map interpreted from fused image93

LIST OF FIGURES

<u>Figure</u>	<u>page</u>
1-1 Study area.....	17
2-1 Radarsat imaging modes.....	51
3-1 Radarsat W1 image.....	65
3-2 IRS-1D image.....	65
3-3 Radarsat S7 image.....	66
3-4 Landsat-7 image.....	66
3-5 Topographic maps.....	67
3-6 Hydrological stations.....	67
3-7 Flowchart of my study.....	68
3-8 Geometry data in HEC-RAS.....	69
3-9 Histogram of Radarsat W1.....	70
3-10 Histogram of Radarsat S7.....	70
3-11 Spectral bands of Landsat-7, IRS-1D and Radarsat-1.....	70
4-1 Flooded areas and water surface elevation simulated by HEC-RAS.....	81
4-2 Radarsat images.....	81
4-3 Overlaid flooded areas from HEC-RAS, Radarsat W1 and Radarsat S7 images.....	82
4-4 Inputs of PCA.....	82
4-5 Principal component images and percentages of the total scene variance.....	83
4-6 Fused image of PC4 (red), Radarsat S7 (green), and PC1 (blue) images.....	84
4-7 Fused image classification.....	85
4-8 Water surface elevation measured from hydrological stations.....	86
4-9 Dead vegetation (area X), built up water body (area Y), and a row of trees (area Z).....	86
4-10 Flooded areas of each land cover type.....	87

4-11	Differences caused by changing in water surface elevation.....	88
4-12	Overlaid flooded areas from the reduced flood map of Radarsat S7 and the fused image flood map.	89
4-13	Inspection of underwater features.....	90
5-1	Radarsat S7 images.....	99

Abstract of Dissertation Presented to the Graduate School
of the University of Florida in Partial Fulfillment of the
Requirements for the Degree of Doctor of Philosophy

FUSION OF LANDSAT-7, IRS-1D AND RADARSAT-1 DATA
FOR FLOOD DELINEATION

By

Siripon Kamontum

August 2009

Chair: Scot E. Smith

Major: Forest Resources and Conservation

In my study, the extent of areas inundated by flood water was delineated. Landsat-7, IRS-1D and Radarsat-1 images were used to create a fused image containing essential information of a flood occurring in 2002 in Thailand. This is the first study to address flood analysis using Landsat-7, IRS-1D and Radarsat-1 data acquired during the same flood event. Two flood maps interpreted from two Radarsat images acquired in W1 and S7 modes were compared against a flood map simulated by HEC-RAS, a hydraulic model that calculates water surface elevation from hydrological and topographic data. It was found that classification accuracies of the flood map interpreted from the Radarsat S7 image were higher than those from the Radarsat W1 image with an overall Kappa value of 88.0 percent for S7 compared to 75.2 percent for W1. Therefore, the Radarsat S7 image was chosen to be the input of a pan-sharpening process. Next, principal component analysis was applied to Landsat and IRS data to reduce data redundancy. First principal component (PC1) image that contained 63.5 percent of the total scene variance and clearly portrayed flood boundaries and fourth principal component (PC4) image that contained 4.9 percent of the total scene variance and showed details in flooded areas were selected to be two additional inputs of the pan-sharpening process. A combination of the

Radarsat S7, PC1 and PC4 images was sharpened to a five meter ground sampled distance by fusion with the IRS panchromatic image. The boundary of the 2002 flood was successfully delineated from the fused image. Classification accuracies of flooded areas interpreted from the fused image were slightly higher than those interpreted from the Radarsat S7 image alone. The overall Kappa value was 93.2 percent versus 90.8 percent when visual interpretation was used as a reference. Damaged areas due to the flood and flooded transportation routes were identified from the fused image. Underwater features could not be detected using the fused image.

CHAPTER 1 INTRODUCTION

Problem Statement

Flooding is both a natural and a man-made phenomenon that can damage the environment, property and destroy life. As more people decide to live in flood-prone areas such as deltas and river basins, it is important to accurately assess the location and boundaries of flooded land so that relief efforts can be coordinated. To facilitate this process, remote sensing data have been utilized, such as Landsat (Green *et al.*, 1983; Townsend and Walsh, 1998; Frazier and Page, 2000; Ryu *et al.*, 2002; Wang *et al.*, 2002; Hudson and Colditz, 2003; Wang, 2004; Neuenschwander *et al.*, 2005), SPOT (Toyra and Pietroniro, 2005), and IRS (Kar, 1994; Sharma *et al.*, 1996; Siegel and Gerth, 2000).

These examples used passive remote sensing. Passive sensors require clear atmospheric conditions which is almost never the case during the rainy season. Consequently, active remote sensing systems, which have the ability to penetrate clouds and other attenuating factors, play an important role in the delineation of flooded lands because the data can be acquired regardless of the weather.

A most common example of an active remote sensing system is Radio Detection and Ranging (radar). Radar data have been applied to many flood mapping applications (Townsend and Walsh, 1998; Horritt *et al.*, 2001; Liu *et al.*, 2002; Toyra and Pietroniro, 2005). However, radar has significant drawbacks such as the fact that it is expensive and the spatial quality of the imagery is relatively poor in comparison to passive remote sensing imagery. Furthermore, radar images are not useful in mapping of urban flooding due to large amounts of corner reflection from buildings (Kiage *et al.*, 2005). Therefore, it is best to combine imagery sets of both passive and active systems for flood delineation.

Fusion of radar and optical data acquired during a rainy season to map inundated areas has rarely been studied, especially in monsoonal zone, because there is little opportunity for (1) clear atmospheric conditions during flooding period and (2) both radar and optical satellites acquiring data of the same location during that period.

During the typhoon season of 2002, a flood occurred in the Northeast region of Thailand but the sky remained clear. These conditions enabled the IRS-1D satellite to acquire data on October 14 and Landsat-7 acquired data on October 25. Radarsat-1 was programmed to acquire data of the same location on October 11 and October 15. For this reason, fusion of optical data (IRS-1D and Landsat-7) and radar data (Radarsat-1) for flood delineation in monsoonal area could be performed. These images were acquired during October 11-25 (14-day duration). During this period, water surface elevation dropped gradually causing different flood extents in these satellite images. For the Radarsat wide mode 1 (W1) acquired on October 11, IRS-1D acquired on October 14 and Radarsat standard mode 7 (S7) acquired on October 15 images, surface water extents were not greatly different, but for the Landsat image acquired on October 25, the surface water extent was noticeably smaller. Therefore, when IRS-1D, Landsat-7 and Radarsat-1 data were fused, the influence of different acquisition dates was included in the fused image. Thus, the temporal factor must be carefully considered when the fused image is interpreted (Pohl and Van Genderen, 1998).

Radarsat imageries available for my study were taken in different modes. The image acquired on October 11, 2002 is the W1 with a 30 m spatial resolution and a 25° incidence angle. Another image acquired on October 15, 2002 is the S7 with a 25 m spatial resolution and a 47° incidence angle. Because spatial data in my study are based on 1:50,000 topographic maps, these Radarsat images with 25 and 30 m pixel size are deemed appropriate. Since the images were

taken at different incidence angles, it was considered necessary to determine which image is better for flood delineation. Flooded areas interpreted from both images were compared to a flood map calculated from Hydrologic Engineering Center's River Analysis System (HEC-RAS), a hydraulic model developed by the U.S. Army Corps of Engineers. Inputs for HEC-RAS include hydrological data collected in the field and topographic data.

There are many studies using only radar data to delineate floods (Dwivedi *et al.*, 1999; Horritt *et al.*, 2001; Freeman *et al.*, 2002; Liu *et al.*, 2002; Rosenqvist and Birkett, 2002; Rosenqvist *et al.*, 2002; Kiage *et al.*, 2005; Henry *et al.*, 2006). In my study, it is hypothesized that classification accuracy of flooded areas derived from a fused image of IRS-1D, Landsat-7 and Radarsat-1 data is higher than that derived from Radarsat-1 data alone. Thus flooded areas interpreted from the fused image were compared to that interpreted from the Radarsat-1 image.

Data fusion techniques have been commonly used to improve interpretability of images, increase spatial resolution, enhance certain features not visible in either of the single data alone, complement data sets for improved classification and substitute missing information (Pohl and Van Genderen, 1998). The techniques were applied in many fields, such as underground coal fires detection (Zhang *et al.*, 1999), land use/land cover mapping (Haack and Bechdol, 2000; Zhu and Tateishi, 2006; Santos and Messina, 2008), and landslide inventory (Nichol and Wong, 2005).

In my study, there are Landsat-7 data taken in the blue wavelength that can penetrate clear water and detect underwater features, and Radarsat-1 data that can detect change of water surface roughness caused by underwater features and/or wind. If fusion techniques are applied to these data, underwater features such as submerged aquatic vegetation may be identified and the fusion techniques may prove to be useful in providing more information of flooded areas.

Objectives

Objectives of my study are as follows:

1. Delineate the flood extent in the study area occurring between October 11-25, 2002 using a combination of IRS-1D, Landsat-7 and Radarsat-1 data
2. Compare flooded areas derived from (a) Radarsat wide mode 1 at 25° incidence angle (b) Radarsat standard mode 7 at 47° incidence angle and (c) HEC-RAS calculation
3. Determine if classification accuracy of flooded areas derived from the fused image of IRS-1D, Landsat-7 and Radarsat-1 is higher than that derived from Radarsat-1 alone
4. Determine if underwater features such as submerged aquatic vegetation can be detected using these data

Study Area

In my research, the study area is in the Northeast of Thailand (also known as Korat Plateau), as shown in Figure 1-1, A. This region is 170,226 sq.km., situated around 90 – 1,400 m above mean sea level. The plateau is bounded by Phetchabun Range and flat-topped mountains (Phu Luang, Phu Kra Dung, and Phu Khieo) in the west, bounded by Dong Phrayayen and Dangrek Ranges in the south, and the Mekong River in the north and east. Major rivers of this area are Mun and Chi rivers, which flow eastward. Area inside the plateau is flat with low hills. Average slope of the whole area is less than 0.5%.

The Northeastern region of Thailand has a population of approximately 21 million, one-third of the country's total population (National Statistical Office, 2000). Most of the land is used for agriculture with 70% rice, 17% field crop, and 13% combination of forest, pasture, natural rubber and others (National Statistical Office, 2003). Yield rates per unit area of this region however, are relatively low compared to other regions of the country, leading to low average income (Kermel-Torres, 2004). Only 10% of agricultural land in the area is irrigated (National Economic and Social Advisory Council, 2007) and the rest of the agricultural land depends solely on rainfall. Agricultural areas are also seasonally inundated by floodwater.

The rainy season is from May to October when the Southwest Monsoon wind conveys humid air from the Gulf of Thailand to the region (Figure 1-1, A), however the wind strength is reduced by mountain ranges located in the west (Phetchabun Range) and the south (Dong Phayayen and Dangrek Ranges) of the region. This wind brings small amounts of rain. Larger amounts of rain occur between August and October due to the influence of storms from the South China Sea (Figure 1-1, A) and flooding usually occurs during this period. The floods damage residential and agricultural areas along the floodplains of the Mun and Chi rivers, the most important rivers in the Northeast. The 2002 floods in the Mun and Chi Basins appear in dark tone in the southeast as shown in Figure 1-1, B.

The dry season of the Northeast region runs from November to April and water shortages usually occur between February and April. At this time, a large proportion of land cannot be cultivated.

The study site is the overlapping area of the IRS-1D, Landsat-7 and Radarsat-1 W1 and S7 images as highlighted by a yellow frame in Figure 1-1, B. Latitude and Longitude of upper left corner are 15° 46' 47.76" N, 103° 45' 42.34" E, upper right are 15° 43' 45.90" N, 104° 03' 08.48" E, lower right are 15° 08' 28.65" N, 103° 55' 56.00" E, and lower left are 15° 11' 41.30" N, 103° 38' 46.44" E. The area is approximately 30 × 65 sq.km.

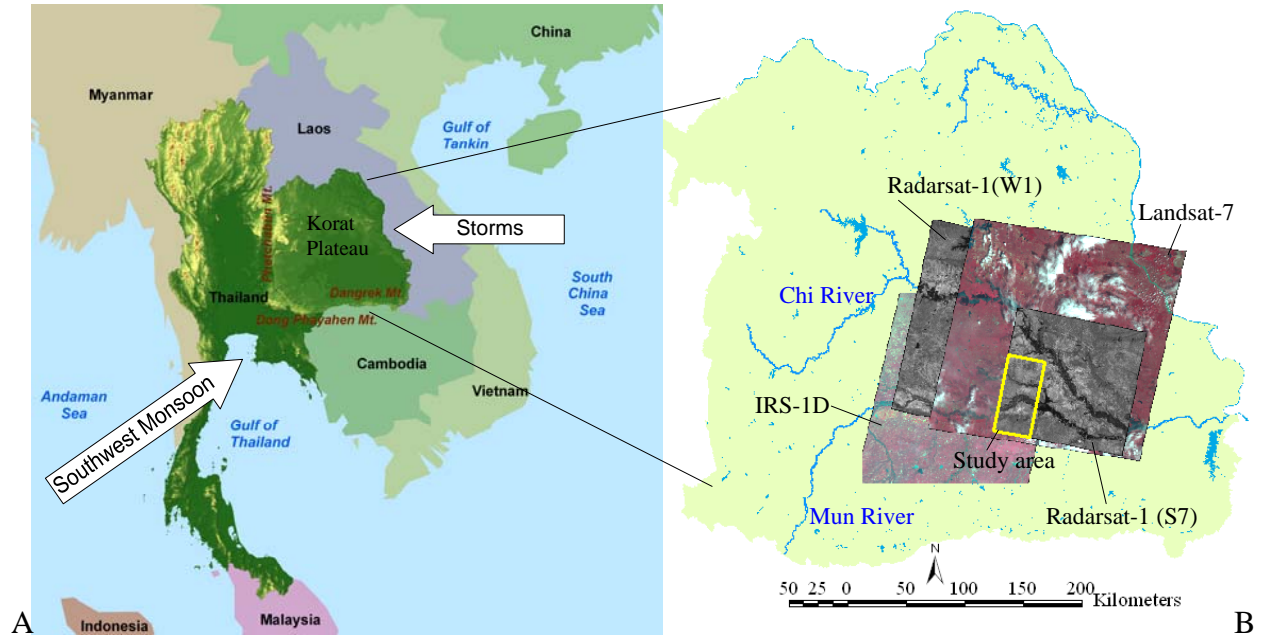


Figure 1-1. Study area. A) Northeast of Thailand and rainfall influences. B) The 2002 flood shown in IRS-1D, Radarsat-1 (W1), Landsat-7, and Radarsat-1 (S7) images.

CHAPTER 2 LITERATURE REVIEW

Image Fusion Techniques

Remote sensing data have been acquired in various wavelengths with different spatial, temporal, and spectral resolution. In my study, Landsat, IRS and Radarsat were used. Due to various input data, image fusion techniques were needed to process the data and create an image containing information of the 2002 flood.

Goshtasby and Nikolov (2007) defined image fusion as “the process of combining information from two or more images of a scene into a single composite image that is more informative and is more suitable for visual perception or computer processing.” Research on image fusion began in the mid-eighties. It was focused on fusing visible and infrared images for surveillance purposes. Many more image fusion techniques were developed in the 1990s and beyond. Image fusion has been successfully applied in medical, industrial, military and civilian remote sensing applications (Goshtasby and Nikolov, 2007).

According to Pohl and Van Genderen (1998), image fusion techniques can be categorized into two groups: (1) statistical/numerical methods, which include Principal Component Analysis (PCA) and (2) color-related techniques, which include Intensity-Hue-Saturation (IHS) color spaces (Pohl and Van Genderen, 1998).

Principal Component Analysis

Redundancy commonly occurs in remote sensing data. For example, images taken in green and red wavelength usually appear similar. They are highly correlated and contain much of the same information. PCA is used to reduce redundancy in remote sensing data by generating fewer bands of non-redundant data from many bands of original data (Lillesand *et al.*, 2007). The first principal component image (PC1) represents the largest percentage of scene variance, while PC2,

PC3, ..., PCn represent successively smaller percentages of the variance. The successive components are chosen to be perpendicular to all previous components to make them uncorrelated. As a result, unnoticed features in PC1 could be identified in PC2 and PC3, for example.

Principal component images can be individually analyzed as black and white images or combined to make a color image and also can be used as input for image classification. Lillesand *et al.* (2007) mentioned that the intrinsic dimensionality of Landsat TM or ETM+ was three. Thus, just PC1, PC2 and PC3 of TM or ETM+ were often used in image classification. PCA has been successfully applied in land use/land cover mapping (Henderson *et al.*, 1998; Saindranath *et al.*, 2000; Saroglu *et al.*, 2004; Santos and Messina, 2008), flood delineation (Hudson and Colditz, 2003), vegetation change detection (Lu *et al.*, 2008), and surface fuel mapping (Mutlu *et al.*, 2008).

In my study, multi-spectral data of Landsat and IRS were inputs. There is redundancy in each sensor data and between both sensor data. Thus, PCA is critical in redundancy reduction.

Intensity-Hue-Saturation

IHS is a color model used for merging images with different spatial resolutions. In an IHS system, color is described in term of intensity, hue and saturation. Intensity characterizes the brightness of a color (lower intensity = darker color; higher intensity = brighter color). Hue defines color. For example 0° or 360° (0 or 255 in 8-bit system) represents red, and 60° (43 in 8-bit system) represents yellow. Saturation indicates purity of a color (Lillesand *et al.*, 2007).

By using an IHS color model, spatial and spectral information of an image can be separated. Intensity represents spatial information, whereas hue and saturation represent spectral information (Pohl and Van Genderen, 1998).

To increase the spatial resolution of a satellite image, the low resolution multispectral image originally in RGB is transformed to the IHS system and then the intensity component is replaced by values from a higher resolution image such as a panchromatic image. This is called “pan-sharpening”. The higher resolution IHS image is transformed back to the RGB color system. In order to produce the best fused image in terms of color balance, the histograms of intensity and the high resolution image must be matched prior to the substitution (Lillesand *et al.*, 2007). A constraint of this method is that number of input bands is limited to only three from a lower resolution image and one band of a higher resolution image.

IHS transformation was successfully applied in geomorphology (Singhroy, 1995; Singhroy *et al.*, 1998; Schetselaar, 2001), wetland delineation (Dwivedi *et al.*, 1999), urban structure classification (Netzband *et al.*, 1999), burned land mapping (Koutsias *et al.*, 2000), flood extent delineation (Srivastava *et al.*, 2000; Spruce and McKellip, 2006; National Emergency System of Uruguay, 2007; Akar *et al.*, 2008; International Charter, 2008), and land use/land cover mapping (Saroglu *et al.*, 2004). Most of these studies used a pan-sharpening, except for studies of Singhroy (1995), Singhroy *et al.* (1998), Dwivedi *et al.* (1999) and Saroglu *et al.* (2004), which C-band radar data were used to replace intensity component of multispectral data.

In my study, a panchromatic image (five m spatial resolution) of IRS was one of input data. Through a pan-sharpening, spatial resolution of the fused image can be increased. Flooded roads can be identified from the pan-sharpened image and this information is necessary for relief effort planning.

PCA and pan-sharpening techniques applied in my study were performed at the pixel level of input images. These pixel level fusion algorithms assume correspondence between pixels in input images; therefore it is critical to accurately co-register all input images to avoid false

classification later on (Pohl and Van Genderen, 1998; Goshtasby and Nikolov, 2007). Pohl and Van Genderen (1998) also commented that fusion of multi-sensor data mostly included temporal factor due to differences in acquisition date/time and users have to be aware of the physical characteristics of the input data in order to be able to judge the resulting data.

Flood Assessment Using Remote Sensing

Flood boundary is important information for flood situation assessment. It is difficult to produce flood extent data through field survey especially for a large area because it is a time consuming process and flood boundary is dynamic. In some cases, a flooded area is inaccessible due to transportation limitation or epidemic in the area. Remote sensing is a powerful technology to acquire flood information of a specific area in a certain time. Furthermore, high temporal resolution remote sensing data can be used to monitor a flood movement. Data from remote sensing satellites, such as Landsat, IRS and Radarsat, are widely used in flood-related applications.

Landsat

The Landsat system has continuously collected data since 1972. Its sensor suite has evolved through several generations. Multispectral Scanner (MSS) on Landsat-1 (launched in 1972), Landsat-2 (launched in 1975), Landsat-3 (launched in 1978), Landsat-4 (launched in 1982) and Landsat-5 (launched in 1984) had four spectral bands (green, red and two bands in near infrared) with 80 m resolution (Lillesand *et al.*, 2007). The thematic Mapper (TM) on Landsat-4 and Landsat-5 had seven spectral bands (blue, green, red, near infrared, two bands in mid infrared, and thermal infrared). The spatial resolution of the thermal band is 60 m while those of the others are 30 m. Landsat-7 (launched in 1999) has an Enhanced Thematic Mapper Plus (ETM+) sensor with eight spectral bands, seven bands like the TM and a new panchromatic band with a 15 m spatial resolution. Details of the Landsat sensor suit are shown in Table 2-1.

The long term record of Landsat data has been particularly useful in flood studies. Green, *et al.* (1983) used a Landsat-1 MSS image (standard color-enhanced combination of green, red and near infrared bands) to define spatial pattern of 1974 flooding in the Darling River floodplain in New South Wales, Australia. The image was acquired four days after the flood peak. Floodwaters (turbid water = light blue tone in the image) were differentiated from stagnant areas (clear water = black tone in the Landsat image). The flood data could be used in planning of roads, levees, and channel construction.

Townsend and Walsh (1998) assessed abilities of Landsat TM, JERS-1 (L-band, HH) Synthetic Aperture Radar (SAR) and ERS-1 (C-band, VV) SAR sensors for detecting flooding in bottomland forests of the lower Roanoke River floodplain, North Carolina. For the classification accuracy assessment, 1126 random sample points were selected. From ANOVA statistics, JERS-1 classification had higher F-value than ERS-1 classification. Thus, JERS-1 had a better ability to identify flooded areas. ERS-1 was less effective than JERS-1 because the shorter wavelength of C-band was scattered by forest canopy. However, for this study area, ERS-1 sensor could detect flooded forest. This might have resulted from open canopies of forests in the study area. For Landsat, the authors recommended that it was suitable for flood detection only during leaf-off periods. The authors also commented that radar data provided independent data that could be used for hydrological model validation, which reduced cost for field-based measurements.

Frazier and Page (2000) compared TM bands 1-7 (not thermal) of Landsat-5 in water body detection. Density slicing classification method was applied to the six bands of Landsat. In classification accuracy assessment, color aerial photographs taken on the same day as the Landsat data were used as reference. The study found that band 5 yielded the highest overall

classification accuracy (96.9%). Band 7 yielded a good result (94.4% overall classification accuracy), but some irrigated crops were misclassified as “water”. Band 4 could be used to identify most of major water bodies (93.6% overall classification accuracy), but some urban areas, hill shadows and paddocks were misclassified as “water”. Band 1, band 2, and band 3 yielded 7.7%, 6.4%, and 8.0% overall classification accuracy, respectively. Band 5 density slicing classification was compared to a 6-band maximum likelihood classification, and found that using only Band 5 to classify water bodies was as successful as using 6 bands of Landsat (96.9% versus 97.4% overall classification accuracy).

Ryu *et al.* (2002) extracted waterline in a tidal flat in Gomso Bay, Korea using Landsat ETM+ data. Density slicing method was used to classify the images. Classification outputs were compared to ground leveling data and waterline tracking using differential GPS observed simultaneously with Landsat-7 acquisition time. It was found that TM band 4, band 5, and band 6 were reliable for waterline extraction during the flood tide. On an ebb tide, band 6 was the most accurate, but it has lower spatial resolution. Thus, the authors recommended using combination of different bands rather than a single band for the waterline classification. Furthermore, the authors found that the Normalized Difference Vegetation Index (NDVI), $(TM4 - TM3) / (TM4 + TM3)$, could be successfully applied to distinguish between turbid water and the tidal flat because reflectance of band 4 was high for both tidal flat and turbid water (reflectance increased as suspended sediment increased) while reflectance of band 3 was low for the tidal flat but high for the turbid water. This band discriminated between clay and silt.

Wang *et al.* (2002) mapped flood extent in a flat terrain along the Tar River, Pitt County, North Carolina using Landsat TM data. TM band 4 was found useful in delineating boundary of land and water, but it was not useful to differentiate between water and asphalt areas because

both areas had low reflectance. In TM band 7 image, water has low reflectance, while asphalt pavement has intermediate reflectance. Thus, the sum of TM band 4 and TM band 7 was used to identify water and non-water areas. A histogram of TM band 4 + TM band 7 was produced and showed that two distinct distributions of wet and dry areas were evident, and a threshold value for water and non-water classification was identified. Cloud shadows, which were initially misclassified as “water”, were later recoded to be non-flooded areas. In the study, a Digital Elevation Model (DEM) was integrated in the classification to identified floodwater under forest canopies, which was an alternative to using radar data. The DEM used in the study was a 30 m USGS DEM with 1 m vertical accuracy. The DEM was filled using flood water elevation recorded at a river gauge. In the study, DEM filling was re-run at ± 1 m of the river gauge reading, but the pattern of the flood did not significantly change. The authors commented that using data from a river gauge to fill DEM only worked for a short distance.

Hudson and Colditz (2003) delineated flooding in a large alluvial valley of the lower Panuco basin, Mexico using Landsat-5 TM acquired eight days after the peak of a large flood in 1993, and Landsat-7 ETM+ acquired in the dry season in 2000. PCA was applied to the Landsat-5 data and input data were bands 1, 2, 3, 4, 5, and 7. It was found that mid-range PCs (PC2 and PC3) were useful for flood mapping. For multi-temporal analysis, band 1, 3, 4, and 7 of Landsat-5 and Landsat-7 were inputs of PCA (band 2 and 5 were excluded because of similarity to other visible and infrared bands) and the result showed that PC2 was the most useful for flood mapping. The authors recommend mid-range PCs for flood delineation, whether using single scene or multi-temporal scenes.

Wang (2004) defined extent of the 1999 flood on a coastal floodplain along the Tar/Pamlico River, North Carolina using Landsat-7 images. The flood peak was on September

21, 1999. Three date data of Landsat were acquired on July 28, 1999 (pre-flood), September 23, 1999 (two days after the peak), and September 30, 1999 (nine days after the peak). The pre-flood image was used for change detection. To delineate flood, various band and band ratio combinations were explored and found that TM band 5 + TM band 7 and TM band 4 + TM band 8 were suitable for wet and dry area discrimination. For the image taken on September 30, flooded areas defined by TM band 4 + TM band 8 were larger than those defined by TM band 5 + TM band 7 because damaged crops still had low reflectance in bands 4 and 8. Therefore, the TM band 4 + TM band 8 of the image acquired days after the peak illustrated the maximum extent of the flood and this method could reduce the requirement of getting simultaneous optical remote sensing data to define maximum extent of a flood. For classification accuracy of TM4+TM8, data from 85 flooded and non-flooded sites were use as reference, and the classification accuracies were calculated for open fields, developed areas, and forested areas. Overall accuracy was highest for classification in open fields: 99.3% for the September 23 image and 96.1% for the September 30 image. For developed areas, the overall accuracy was 89.7% for the September 23 image and 82.5% for the September 30 image. For forested areas, overall accuracy was lower than other areas because the wavelengths used in Landsat cannot penetrate forest canopies (overall accuracy was 84.6% for the September 23 image, and 87.0% for the September 30 image).

Neuenschwander *et al.* (2005) compared ability of Landsat-7 ETM+ sensor to the Advanced Land Imager (ALI) sensor (on the NASA EO-1 satellite) to map flood in the lower Okavango Delta, Botswana. Bayesian Pairwise Classification (a supervised classification that uses a class-dependent band selection technique) was applied to both data, and found that, ALI yielded 100% in both producer's and user's accuracies of water class, whereas ETM+ yielded

99.63% producer's accuracy and 99.26% user's accuracy. In the ETM+ data, swamp was often misclassified as "water" causing overestimation of total flooded area in the delta. For other land cover classes, the ALI sensor also yielded higher classification accuracies than ETM+ sensor.

According to this research, Landsat data alone provide satisfactory results in flood delineation. Using only one band or summation of two bands of Landsat (TM4, TM5, TM6, TM5+TM7, or TM4+TM8), land and water were successfully distinguished and histogram threshold (also known as density slicing) classification method was often used (Frazier and Page, 2000; Ryu *et al.*, 2002; Wang *et al.*, 2002; Wang, 2004). PCA was also applied to Landsat data, and mid-range PCs (PC2 and PC3) were recommended for flood delineation (Hudson and Colditz, 2003)

Like other optical sensor data, cloud contamination caused a discrepancy in flood delineation using Landsat data (Wang *et al.*, 2002). To avoid cloud cover, a Landsat image acquired days after a flood peak could be used to delineate maximum flood extent by using TM4+TM8 (Wang, 2004).

To detect flood under forest canopies, L-band and C-band radar data were found to be superior to Landsat data (Townsend and Walsh, 1998), but the cost of radar data is higher. Thus, Wang *et al.* (2002) used stream gauge data and DEM to estimate flood in a forest and they found that using the stream gauge data to fill the DEM could be used for a short distance. Therefore, using a flood model probably yields a better result and thus can be an alternative to costly radar data to detect flood underneath canopies.

Landsat-7 ETM+ sensor had a limitation to differentiate between water and swamp (Neuenschwander *et al.*, 2005). If Landsat data are fused to other sensor data, certain features not visible in either of the individual data sets can be enhanced. There have been many studies that

fused Landsat and other sensor data to detect features that were hard to discriminate using single sensor data alone. They include fusion of Landsat and airborne SAR data for landslide, erosion and deposition assessment (Singhroy, 1995), fusion of Landsat and SPOT, Landsat and IRS, Landsat and Radarsat, and Landsat and ERS data to differentiate urbanized area, bare ground, and estuarine emergent (Henderson *et al.*, 1998), fusion of Landsat and Radarsat for landslide identification (Singhroy *et al.* 1998), fusion of spaceborne images (Landsat, SPOT, NOAA-AVHRR, and ERS-1), airborne images (optical and thermal infrared), and GIS data to detected underground coal fires (Zhang *et al.*, 1999), fusion of Landsat, and C-band and L-band images of Shuttle Imaging Radar (SIR-C) to differentiate mud-brick houses, scattered agriculture, and natural vegetation in savanna environment (Haack and Bechdol, 2000), fusion of Landsat and SPOT images for urban growth detection (Gluch, 2002), fusion of Landsat and ERS-1 data for land cover mapping (Zhu and Tateishi, 2006), fusion of Landsat and Radarsat for land cover mapping (Huang *et al.*, 2007; Santos and Messina, 2008), and fusion of Landsat and SPOT for land cover change detection (Lu *et al.*, 2008).

IRS

The Indian Remote Sensing (IRS) satellite was first launched in 1988. IRS-1A, the first satellite of the series, carried two types of Linear Imaging Self-scanning Sensor (LISS), LISS-I and LISS-II. Spatial resolution of LISS-I was 72.5 m while that of LISS-II was 36.25 m. Both LISS-I and II had four spectral bands (blue, green, red and near infrared). In 1991 IRS-1B was launched and equipped with the same sensors as IRS-1A. Later, in 1995, IRS-1C was launched and equipped with LISS-III sensor with 23 m spatial resolution and four spectral bands (green, red, near infrared and mid infrared). IRS-1C also carried panchromatic sensor (5.8 m resolution) and Wide Field Sensor (WiFS) with two spectral bands (red and near infrared) at 188 m spatial resolution. In 1997, IRS-1D was launched and equipped with the same sensors as IRS-1C.

IRS data have been applied in many flood applications. Kar (1994) investigated the 1990 flood in Luni-Jawai plains of the Thar Desert in India using false color composites of IRS-1A LISS-I and LISS-II images acquired during pre-flood (October 25, 1988) and post-flood (November 12, 1990) periods. The study found that spatial distribution of flood damages was controlled by lineaments in the study area.

Sharma, *et al.* (1996) delineated the 1993 flood in Punjab, India using IRS-1A LISS-I and ERS-1 SAR (C-band, VV) images. The flood was caused by a heavy rain during July 10-12, 1993 (58% of the annual rainfall). Flooded areas were visually interpreted from false color composite images of IRS-1A (acquired on July 27-29, 1993), and ERS-1 images (acquired on July 19, 1993). The 1993 flood map was then superimposed with the 1988 flood map to generate a general flood prone area map.

Siegel and Gerth (2000) studied 1997 floodwater distribution patterns of the Oder River, Germany. The flood patterns were observed in terms of concentration of suspended matter and sea surface temperature (SST). Data from WiFS sensor (188 m spatial resolution, 774 km swath width) equipped on IRS-P3 and IRS-1C were used to map distribution of suspended matter while infrared data of NOAA-AVHRR were used to create SST maps. The maps were then compared to ship-borne measurements, and both data sets were well matched.

Srivastava *et al.* (2000) interpreted 1998 flood extent in Marigoan district in Assam State, India from two bands (red and near infrared) of WiFS sensor of IRS-1C acquired in September 1998. To assess the damage, the flood map was intersected with a land cover map derived from a pan-sharpened image of IRS-1C LISS-III and panchromatic data acquired before the flood.

Dwivedi and Kandrika (2005) delineated aquaculture areas using fused image of LISS-III and panchromatic sensor data from IRS-1C and IRS-1D. In the fusion, PCA was applied to

multispectral data, and then first principal component was replaced by a high resolution panchromatic image. Next, inverse PCA was applied to the data. In the fused image, bunds of aquaculture ponds were clear and sharp. The image was used to digitize the boundaries of ponds. From field survey, shapes of prawn ponds were narrow and long comparing to fish ponds. To segregate prawn and fish ponds, shape factor (polygon area divided by polygon perimeter) was calculated, and a threshold value of 18.0 was found to be optimal for the segregation. Classified prawn and fish ponds were compared to field survey data. Overall classification accuracy was 82.6%. The data derived from the fused image were important for environmental health studies.

Boruah *et al.* (2008) used IRS LISS-I and LISS-III sensor data acquired in 13 years to detect change in channel planform and physical habitat on the braided Brahmaputra River in Assam, India. ENVI's K-means unsupervised classification was used to map water, sand bar, and riparian vegetation. The authors found that GROW facility in ENVI software was more suitable than the K-means method to classify river water. GROW allowed users to set up a training area and define a specific standard deviation (in this study, standard deviation was 2), and then connected river channel and its branches were reliably mapped. River water in the study area was classified into three sub-classes: deep water, medium water, and shallow water. Overall classification accuracy was 85%, when aerial photographs, local knowledge of the area, and scrutiny of the images were used as references.

Data from three sensors of IRS (WiFS, LISS, and panchromatic) were used in many studies. WiFS sensor data are suitable for flood detection in large areas (Siegel and Gerth, 2000; Srivastava *et al.*, 2000; Bhan and Flood Team, 2001) because of its large coverage and 3-day revisit time (Van der Sanden *et al.*, 2001). LISS sensor data, which has higher spatial and

spectral resolution than WiFS, were also used to differentiate land and water (Kar, 1994; Sharma, *et al.*, 1996; Boruah *et al.*, 2008).

High spatial resolution panchromatic image of IRS plays an important role in image fusion. Fusion of IRS LISS and panchromatic sensor data was proved to be successful in many applications: land cover mapping (Saraf, 1999; Srivastava *et al.*, 2000; Saroglu *et al.*, 2004), settlement structure identification (Netzband *et al.*, 1999), salt-affected soil delineation (Dwivedi *et al.*, 2001) and segregation of prawn and fish ponds (Dwivedi and Kandrika, 2005).

IRS and other sensor data were fused in many studies, such as fusion of IRS-1B LISS-II and ERS-1 data (ERS-1 data replaced intensity component of the IRS image) for wetland mapping (Dwivedi *et al.*, 1999), fusion of IRS-1D LISS-III and ERS-1 data for land use/land cover mapping (Saroglu *et al.*, 2004), and fusion of IRS-P6 and Landsat-5 data for flood mapping (National Emergency System of Uruguay, 2007).

Like other optical sensor data, cloud cover causes missing data in IRS images. In a study of Dwivedi *et al.* (1999), IRS and ERS-1 images were acquired at a concurrent time, and there was cloud contamination in the IRS image. After the two images were fused, wetlands of the Sundaban Delta (West Bengal, India) were successfully mapped. This indicated that missing data in the IRS image were substituted by the ERS-1 data through the fusion process. Therefore, fusion of optical and radar data is not only improve interpretability of the image, but also substitute missing data due to cloud cover.

Radarsat

Radarsat-1 is a Canadian earth observation satellite launched in November 1995. It is equipped with a SAR sensor using a single frequency (C-band at 5.3 GHz frequency), and single polarization (HH). Radarsat-1 can acquire data at various incidence angles and swath widths

(bigger swath width, lower spatial resolution), as shown in Figure 2-1 and Table 2-2 (Canadian Space Agency, 2008).

Radarsat data were used in many flood studies. Yang *et al.* (1999) used Radarsat ScanSAR (50 m spatial resolution) acquired on July 28, 1998 to determine flood extent in Qianshan county, Anhui province, China. Land and water were classified using a histogram threshold method. The study area is mountainous, and mountain shadows appeared in the Radarsat image. These shadows caused confusion in the classification. Furthermore, parts of water in a large lake were misclassified as “dry area” due to rough water surface (caused by wind) that returned large amount of backscatter to the radar antenna. To reduce the misclassification, Landsat TM data (acquired on December 7, 1995, pre-flood period) were used to extract hill shade and water bodies. Histogram threshold classification method was applied to Landsat band 2 to extract hill shade. If digital number (DN) of a pixel was less than 23, that pixel was then classified as hill shade. Next, flooded areas interpreted from the Radarsat image was subtracted by hill shade. Landsat data were also used to classify water bodies during pre-flood period. A pixel was classified as water body, if $TM2 \geq 10$ and $(TM2 + TM3) > (TM4 + TM5) - 10$. The Landsat derived water bodies were included in the flooded areas interpreted from the Radarsat image. In classification accuracy assessment, visual interpretation was used as reference. Overall accuracy for mountainous areas was 85%, and that of flat terrain was 90%. This study shows that merging of information from Landsat can improve classification accuracy of Radarsat data. Information from Landsat reduced misclassification due to hill shadows and rough water surface, which are disadvantages of radar sensor.

Zhou *et al.* (2000) monitored the 1998 flood in the Nenjiang and Songhua River Basins, China using multi-temporal NOAA AVHRR and Radarsat images. Peak discharge of the flood

was on August 12, 1998. Flooded areas were classified from cloud-free AVHRR images acquired on July 30, August 14 and 24. AVHRR images were suitable for monitoring dynamic of flooding due to its high temporal resolution, but the authors required higher spatial resolution images to evaluate flood damages. Landsat TM data acquired during that period could not be used due to serious cloud contamination. Therefore, Radarsat images (ScanSAR, 50 m spatial resolution) acquired on August 15, 23, and 29 were used. To identify flooded areas, a histogram threshold classification method was used. The authors concluded that multi-temporal images from both optical and radar sensors were successfully applied to monitor the dynamics of flooding.

Townsend (2001) mapped seasonal flooding in forested wetlands of the Roanoke River floodplain in North Carolina using multi-temporal Radarsat S1, S2 and S6 images taken at 23.1°, 27.5° and 44.0° incidence angles, respectively. Eleven Radarsat images were acquired in 1996 – 1998 during both leaf-on and leaf-off periods. Threshold values were used to classify flooded and non-flooded forest. Overall classification accuracy of leaf-off images was higher than that of leaf-on images (98.11% versus 89.09%), when data from 13 U.S. Geological Survey wells were used to validate the results. This study showed that Radarsat data could be used to map flooded forests in temperate regions regardless of season and water stage. The author did not comment influence of different incidence angles on the outputs.

Toyra *et al.* (2001) mapped extent of standing water in the Peace-Athabasca Delta, Canada from Radarsat S2 (27.5° incidence angle) and SPOT multispectral images. Mahalanobis distance supervised classification was applied to the data. To validate the classification output, data from field measurements, aerial photos, and maps were reference data, and then Kappa coefficients were calculated. Kappa coefficient of combination of Radarsat and SPOT, Radarsat alone, and

SPOT alone were 0.92, 0.76, and 0.80 respectively. At 95% confident level, Kappa coefficient of combination of Radarsat and SPOT was significantly different from that of Radarsat and SPOT alone, but Kappa coefficient of Radarsat and SPOT were not significantly different. The study found that the Radarsat image taken at small incidence angle (20° - 31°) could penetrate canopies of willow, grasses or sedges and detect standing water under the vegetation canopies.

Furthermore, this study examined the effect of incidence angle on flood mapping by comparing combination of Radarsat S1 (23.5° incidence angle) and SPOT to combination of S7 (at 47.0° incidence angle) and SPOT. Kappa coefficient of Radarsat S1 and SPOT was higher than that of Radarsat S7 and SPOT (0.83 versus 0.74), and the Kappa coefficients were significantly different at 95% confident level. The Radarsat S7 taken at bigger incidence angle had longer path length through the canopies; therefore its signal was more attenuated. By using the same data set, a study of Toyra and Pietroniro (2005) found that signal of Radarsat S1 and S2 (small incidence angle) were very sensitive to waves on water surfaces, and many pixels in Lake Claire was misclassified as “dry vegetation”. To eliminate this confusion, SPOT data were combined with the Radarsat data, but for areas outside coverage of the SPOT image, the misclassified areas were manually recoded as open water. The study also found that Radarsat S7 (big incidence angle) image was not sensitive to wave action.

Kiage *et al.* (2005) used Radarsat ScanSAR narrow (50 m spatial resolution) images to assess flooding in coastal Louisiana due to Hurricane Lili causing flood peak during October 3-4, 2002. Three Radarsat images used in the study were acquired on September 23 and 28 (pre-flood), and October 3 (during the flood). The study found a new method to identify flooded areas. First of all, mean values of pixels from the two pre-flood images were calculated to create a mean image, and then subtracted the mean image from the Radarsat image acquired during the

flood period. Flooded areas appeared as darker regions and were easily identified. The study confirmed that Radarsat ScanSAR data were suitable for delineate flood in coastal marshes following hurricanes. However, the ScanSAR images were not useful in mapping of urban flooding in New Orleans after Hurricane Katrina, August 2005, due to large amounts of backscatter from the buildings, and combination of Radarsat and SPOT data to map the flood after Hurricane Katrina was in progress.

Lang *et al.* (2008) examined influence of different incidence angles (23.5°, 27.5°, 33.5°, 39.0°, 43.5°, and 47.0°) of Radarsat images to detect flood underneath forest canopies during leaf-on and leaf-off periods. The study area was the lower Roanoke and Cashie River floodplain, North Carolina. To discriminate flooded and non-flooded areas in each image, a threshold value was used. Flood extents interpreted from the Radarsat images were verified using flood extents estimated by a flood simulation model of Roanoke River floodplain developed by Townsend and Foster (2002), and the data were used only when flood extents from both sources were in agreement (no comparison detail was described in the literature). A hypothesis of the study was that an image taken at a larger incidence angle was less sensitive to flooding. The study found that the sensitivity slightly decreased with increasing incidence angle, but the sensitivity did not significantly decrease as found in the study of Toyra *et al.* (2001).

According to these studies, Radarsat data were very useful for flood mapping due to cloud penetration ability. To differentiate between flooded and non-flooded areas, a threshold value was often used (Yang *et al.*, 1999; Zhou *et al.*, 2000; Townsend, 2001; Liu *et al.*, 2002; Lang *et al.*, 2008). Flooded areas interpreted from Radarsat images were so reliable that they were used to validate ability of MODIS to detect flood in Cambodia and Vietnamese Mekong Delta (Sakamoto *et al.*, 2007)

However, using Radarsat data alone to delineate flood was not suitable for some study areas, where mountain shadows, waves on water surface, and large amount of corner reflections caused confusions in Radarsat images (Yang *et al.*, 1999; Toyra and Pietroniro, 2005; Kiage *et al.*, 2005; Song *et al.*, 2007). To eliminate these confusions, Radarsat data were combined with local slope information (Song *et al.*, 2007) or data from optical sensors, such as Landsat (Yang *et al.*, 1999) and SPOT (Toyra and Pietroniro, 2005; Kiage *et al.*, 2005).

Radarsat can acquire data at various incidence angles. Staples *et al.* (1998) suggested that a Radarsat image taken at large incidence angle (more than 40°) was appropriate for land and water differentiation. To detect flood water under vegetation canopies, Toyra *et al.* (2001) found that a Radarsat image taken at a small incidence angle was significantly better than one taken at a big incidence angle, but Lang *et al.* (2008) found that different incidence angles of Radarsat images did not significantly affect ability to detect flood under forest canopies. This may result from different study areas.

A Radarsat image taken at a big incident angle was used to detect submerged reef in a study of Staples *et al.* (1998). Submerged reef caused turbulent water, and large amounts of backscatter were returned to the antenna, but its surroundings had lower backscatter due to smoother water surface. Thus, the reef was detected in the Radarsat image.

Radarsat data have been combined with other sensor data in many applications. They include fusion of Landsat and Radarsat data to differentiate urbanized area, bare ground, and estuarine emergent (Henderson *et al.*, 1998), combination of Radarsat, airborne SAR, and Landsat TM data to identify landslide features (Singhroy *et al.*, 1998), fusion of Radarsat and ERS-2 data for land cover mapping (Saindranath *et al.*, 2000), combination of Radarsat and JERS-1 data for land cover mapping (Souza Filho *et al.*, 2005), combination of Radarsat and

Landsat data for land cover mapping (Huang *et al.*, 2007), and combination of Radarsat texture information, Landsat, and digital video data for land cover mapping (Santos and Messina, 2008).

For Thailand, a country in monsoonal zone, Radarsat plays a crucial role in flood detection because of cloud penetration ability. Flood extent and marooned villages can be identified from a Radarsat image. However, decision makers require more information to evaluate flood situation. To provide a range of helps to flood victims, up-to-date information of roads that may be damaged by the flood is needed, and this information can be derived from panchromatic data of IRS. Most Thai people do not have flood insurance; therefore, the government has to provide flood compensation. Land cover types affected by the flood can be extracted from multi-spectral data of Landsat and IRS. This information can be used as an input for flood compensation calculation. For these reasons, data of Landsat, IRS, and Radarsat acquired during the flood period have to be fused to create an image containing necessary information for decision makers. According to literature review, there is no research that fuses data of Landsat, IRS, and Radarsat acquired in the same flood period to create an image illustrating the flood situation. Therefore, fusion of these data needed to be done.

Flood Models

To prevent flood damage, information of flood risk areas should be provided to people settling in those areas. A historical record of past floods allows these people to understand the level of risk they face. To prepare this information, a flood model can be used to simulate different flood scenarios. Also, flood models are important in flood management analysis because they are essential to simulate flow before a flood control structure is built. Flood models are critical in historic flood studies as well.

Flood forecasting methods have been continuously developed. For the Nile, Hurst (1952) concluded that two successful methods included: (1) “railway time-table” method where if the

water surface elevation at an upstream is measured, the time that this volume of water would reach a downstream point could be calculated and (2) forecasting based on the concept that after the end of a rainy season at headstream area, the discharge of one month influences the discharge of the following month. Then correlations of the discharge can be calculated and were used in the forecasting. This method worked well during November – May before the beginning of the next rainy season.

For the Mississippi River, the U.S. Army Corps of Engineers (USACE) has applied several hydraulic models to calculate water surface elevation. According to Haestad Methods (2007), during 1950s - 1960s calculation of the Mississippi Basin Model (MBM) was initially done by hand until the mid to late 1960s when computers began to be used, and Hydrologic Engineering Center (HEC) was formed in 1964 (U.S. Army Corps of Engineers, 2007). In 1970s, flow parameters were statistically analyzed to predict 5 - 500 year return period of floods and cross sections along the 300 mi. (483 km.) reach of the Mississippi were surveyed. In 1980s, the cross section data were used to develop HEC family software: HEC-1 (watershed hydrology), HEC-2 (river hydraulics), HEC-3 (reservoir analysis for conservation), and HEC-4 (stochastic streamflow generation program) (Haestad Methods, 2007; U.S. Army Corps of Engineers, 2007). In 1995, HEC-2 was superseded by HEC-RAS that can calculate water surface elevation based on one-dimensional steady and unsteady flow regimes (U.S. Army Corps of Engineers, 2002).

For my study, the focus is on depth and boundary of flood water, not in water quality or sediment transportation. Therefore, models for flow simulation were considered. According to U.S. Geological Survey (2008), flow simulation models could be categorized into three groups: one dimensional (1D), two dimensional (2D), and three dimensional (3D). The 1D model considers flow parameters (such as velocity) only in the same direction of the flow (longitudinal

direction). The 2D model considers flow parameters in longitudinal direction and another direction, vertical or horizontal direction. The 3D model considers flow parameter in longitudinal, vertical, and horizontal directions. Higher dimensional models can thoroughly simulate flow characteristics, but they need more input data. Correia *et al.* (1998) suggested that more complex models were not necessarily better for some specific uses. On the other hand, a simpler model requiring less input data might be more suitable for a study area that lacks input data. Di Baldassarre *et al.* (2009) also commented that 1D models were suitable for flood simulation in natural rivers when hydraulic situation was not dominated by 2D phenomena, such as dam or levee failure.

A study of Horritt and Bates (2002) confirmed that the ability to predict river flood inundation of a 1D model was equal to a 2D model. In the study, HEC-RAS (1D model), LISFLOOD-FP (2D model), and TELEMAC-2D (2D model) were compared on a 60 km reach of the Severn river, UK with 19 ground surveyed cross sections and a LiDAR derived DEM. Test flood events were the 1998 (435 m³/s peak flow) and 2000 (391 m³/s peak flow) floods. Flooded areas were interpreted from a 1998 Radarsat-1 (C-band, HH) image and a 2000 ERS-2 (C-band, VV) image. There were six calibration/validation combinations for the three models:

- (1) calibrated on the 1998 flood wave travel time and validated by the 1998 Radarsat image,
- (2) calibrated on the 1998 flood wave travel time and validated by the 2000 ERS-2 image,
- (3) calibrated on the 1998 Radarsat image and validated by the 2000 ERS-2 image, (4) calibrated on the 2000 flood wave travel time and validated by the 2000 ERS-2 image, (5) calibrated on the 2000 flood wave travel time and validated by the 1998 Radarsat image, and (6) calibrated on the 2000 ERS-2 image and validated by the 1998 Radarsat image. After the calibration, optimum friction coefficients of main channel and floodplain were designed for each model and each flood

event. The study found that HEC-RAS and TELEMAC-2D yielded equally good predictions, and were better than LISFLOOD-FP. The authors commented that performances of the models were different because they were differently sensitive to changes in friction coefficients.

Although 1D models are widely used to simulated river flood inundation, they are not appropriate for all kinds of study areas. Mark *et al.* (2004) found that 1D models had limitations for predicting floods in an urban area, where both overland flow and flow in underground pipe systems existed and interacted to each other.

In my study, the study area was a rural area dominated by non-irrigated agricultural land. Flooding in the study area occurred along natural rivers, Mun and Lam Sieo Yai rivers.

Available hydrological data were daily discharge and daily water surface elevation collected from ground-based stations situated far away from each other, and some river reaches did not have stations. Due to physical characteristics of the study area and limitation of available hydrological data, 1D model was deemed an appropriate model for my study. One dimensional flood simulation models widely applied to study areas in Thailand were HEC-RAS (developed by the U.S. Army Corps of Engineers) and MIKE11 (developed by Danish Hydraulic Institute).

Weesakul (1995) set up a real time flood forecasting model of Klong Utaphoa River Basin in Songkhla province. In the study a rainfall-runoff model, NAM, was used to calculate runoff from rainfall data, and MIKE11 was used to simulate flow in the river. A limitation of the study was insufficient input data. Only daily hydrological data were available, while 6-hour hydrological data were recommended, and more rainfall stations in the study area were needed.

Petchprayoon (2001) predicted flood wave characteristics and estimated damaged areas caused by failure of Tha Dan dam in Nayok province using MIKE11. In the study, damaged areas from dam failure and overflow through spillway were predicted in four different severities.

To estimate flood damage of each land cover type, flooded areas were overlaid to land cover data interpreted from a Landsat-5 image.

Taragsa et al. (2004) used HEC-RAS to predicted flood along Chi river floodplain in Maha Sarakham, Kalasin and Roiet provinces. A HEC-RAS result was compared to a flood map interpreted from a Radarsat image, and found that both flooded areas were in agreement by 52.26%. Minimum, normal, and maximum Manning's n values of each land cover type were tested, and found that normal values yielded a better result. The authors commented that the model needed more input data and more calibration.

Kidson et al. (2005) used HEC-RAS to estimate discharge of two palaeofloods (84-year and 49-year floods) of the Mae Chaem River, Northern Thailand, based on palaeo-stage indicators (sand and silt terraces located independently, wood debris deposited in three separate caves). The authors commented that HEC-RAS, a 1D model, was suitable for the calculation because a greater dimensional model requires more input data, which were difficult to identify from palaeoflood evidence.

Sansena and Bhaktikul (2007) created flood risk maps of 5, 10, 25, 50,100 year return periods of Mae Klong River in Ratchaburi province. In the study, hydrological data collected during 1985-2002 were used for frequency analysis, and 2-parameter log normal distribution was found to be the best fit for the data set. HEC-GeoRAS and HEC-RAS were used to create flood risk maps. The 1996 flooded areas predicted by HEC-RAS was compared to 1996 flood map of the Royal Irrigation Department, and found that both flooded areas were in agreement by 60.52%. The authors also commented that the DEM was the most important factor for flood simulations, and a higher resolution DEM was required to obtain more accurate results.

According to these studies, HEC-RAS and MIKE11 were successfully applied in Thailand for flow simulation in Northern region (Kidson et al., 2005), Northeastern region (Taragsa et al., 2004), Central region (Petchprayoon, 2001; Sansena and Bhaktikul, 2007), and Southern region (Weesakul, 1995). In my study, HEC-RAS was chosen because it yielded a good result and the software (HEC-RAS and HEC-GeoRAS) are free for download, while MIKE11 is a commercial software.

Advantages of HEC-RAS are not only its ability to produce an accurate result, but also its availability and accessibility for all users to download it through the internet. As a result, HEC-RAS was widely used to simulate water flow in many study sites, such as the Livramento catchment in Setubal, Portugal (Correia *et al.*, 1998), Ste. Agathe in Manitoba, Canada (Ahmad and Simonovic, 2001), the river Möhne in Germany (Dose et al., 2002), the Tagus Basin in Central Spain (Benito *et al.*, 2003), the Areias creek catchment in Brazil (Diniz *et al.*, 2003), San Antonio River Basin (Knebl *et al.*, 2005), Tabunganen Scheme in South Kalimantan, Indonesia (Wignyosukarto, 2006), the South Nation watershed in Canada (Yang *et al.*, 2006), Manoa Valley (El-Kadi and Yamashita, 2007), Shitalakhya River in Bangladesh (Islam, 2007), and Atrato River in northwest of Colombia (Mosquera-Machado and Ahmad, 2007).

Flood Models and Remote Sensing

Remotely sensed data have been used in hydrological models as a direct input (such as LiDAR DEM), a source of information for parameter setting, and reference data for model calibration/validation. Van de Griend and Engman (1985) commented that remote sensing data enhanced ability of hydrological models based on partial area concept, a method dividing watershed into contributing areas. Temporal and spatial characteristics of these contributing areas (such as vegetation types, temperature and soil moisture) could be identified using remote sensing data instead of laborious field survey.

Schultz (1988) concluded that information from remote sensing have been used as input for hydrological models or used to estimate parameters in hydrological models. Model parameters based on watershed characteristics, such as drainage density, land use/land cover, and soil types could be interpreted from Landsat and SPOT images, and slope could be obtained from a stereo pair of SPOT images. The author also used NOAA infrared data with a long time record to calculate historic runoff values of catchments in Southern France. One-year period of concurrent data from both field survey and NOAA were used to calibrate a model. By using input from NOAA data alone, the model could estimate historic runoffs that were useful for planning purposes. Remote sensing data from ground-based C-band weather radar were used as an input for real time flood forecasting of Gunz River catchment, Germany.

Blyth (1993) concluded that remote sensing data were used to aid hydrological models in three ways: site selection for instrument setting, illustrating physical characteristics of catchments, and hydrological variable estimation. Location of ground-based measurement devices could be designed properly based on information from remote sensing that showed variation and homogeneity of a study area. Physical characteristics of catchments (such as stream length, surface water extent, drainage ditches, slope and land cover) could be extracted from Landsat and SPOT data, and surface roughness information could be derived from a radar image. Hydrological variables (such as precipitation, vegetation moisture and soil moisture) could not be directly measured using remote sensing data, but the variables could be estimated using a transfer function relating ground-based data to remote sensing data. By applying the transfer function to remote sensing data, spatial variation of hydrological variables could be illustrated.

Sharma *et al.* (1996) simulated rainfall-runoff process of the Divisadero Largo basin in Argentina using a 1D raster-based hydrological model, SWAMREG. Input data of the model

were soil type, slope, vegetation (interpreted from a Landsat TM image), and rainfall data.

Thirteen rainfall-runoff events were used to calibrate the model, and other 13 events were used to validate the model. The model divided inflow (direct rainfall and inflow from the upstream) into infiltration and outflow, and simulated rainfall excess and outflow hydrographs. Outputs of the model were overall hydrograph, peak discharge, runoff volume, and flow duration. Relative square errors of the 13 validation events were between 3.7% - 13.2%.

Profeti and Macintosh (1997) used Landsat TM images (acquired on January 27, August 7, and October 26, 1991) to estimate soil water content of the Fucecchio Marsh in Tuscany, Italy. Band5/band7 (correlating to soil water content) was compared to band1/band2 (decorrelating to soil water content). Validation data were calculated from the Fucecchio Marsh hydrological model, developed by Civil Engineering Department, Florence University. The model is raster-based using cumulative daily rainfall and soil moisture data measured in the field as inputs. Correlation coefficient between the Landsat band ratios and model outputs were calculated based on each soil type. The study found that band1/band2 had higher average correlation coefficient than that of band5/band7 (0.727 versus 0.639). Highest correlation coefficients obtained from soil types those had low vegetation cover. This study also monitored the 1992 flood in the study area using ERS-1 and ERS-2 data acquired on October 16, 1992 (pre-flood) and November 4, 1992 (four days after the flood). Both images were inputs of a supervised classification to identify flooded and non-flooded areas.

Bates and De Roo (2000) developed a new flood simulation model, LISFLOOD-FP. The model is raster-based, and was designed to operate with high resolution and high accuracy DEMs (such as LiDAR DEM) that represent physical characteristics of channel and other elements (such as dykes, embankments, depressions, and former channels). The test site was the River

Meuse in The Netherland, where a large flood occurred in January 1995 and validation data from aerial photos and ERS-1 were available. The model yielded percentage correct at 81.9%, when it was compared to flooded/non-flooded areas interpreted from the aerial photos and the ERS-1 image.

Fox and Collier (2000) presented a method to calculate probability of a flood caused by heavy convective rain. The prediction could be done at a lead-time of up to seven days. The test site was the River Irwell catchment in the Northwest of England. Inputs of the model were sensible heat flux data estimated from NOAA-AVHRR, precipitable water content of the atmosphere, and velocity of ascending air. The model was tested using data acquired in the second half of July 1996, and found that predicted convective rainfall had some correlation with observed convective rainfall. However, the proposed method required a longer trial period to evaluate reliability of the model.

Biftu and Gan (2001) developed a physically based hydrological model, named DPHM-RS, of the Paddle River Basin, Central Alberta in Canada. DPHM-RS was designed to incorporate remote sensing data in the model. Input data of the model were obtained from both field measurement and remote sensing (Landsat TM/MSS, NOAA-AVHRR, and Radarsat). The remotely sensed data yielded information of land cover, surface albedo, and vegetation index. The model could simulate runoff, surface temperature, net radiation, and soil moisture of the Paddle River Basin. Simulated and observed runoffs were in agreement of 60-85%. Simulated surface temperatures were close to those derived from Landsat TM and NOAA-AVHRR (discrepancies were less than 2 °K), but for cloudy day discrepancies were 3-7 °K because the surface temperature derived from the images represented temperature of clouds, which was lower than temperature of the ground surface. Simulated net radiation agreed well with observed

except for rainy days due to cloud cover. Daily mean soil moisture data estimated from the model agreed well with those estimated from Radarsat images.

Bjerklie *et al.* (2005) developed a method to estimate river discharge using remotely sensed data. The test sites were 17 single channel rivers (in New Hampshire, Vermont, Connecticut, Illinois, Maryland, South Dakota, Colorado, Montana, Kansas, Oregon, Delaware and Washington) and three braided rivers (in Alaska and British Columbia). Inputs data were water surface width and maximum channel width (measured from Digital Orthophoto Quadrangles and airborne SAR images), and channel slope data (obtained from 1:24,000 topographic maps). To improve accuracy of the estimated discharges, observed discharges were used to create a correction function for single channels and another function for braided channels. After applying the correction function to the estimated discharges, largest log residuals were at two reaches, where flow activity was managed (the Mississippi River at Thebes in Illinois and the Sacramento River near Red Bluff in California). Furthermore, the authors proposed another method to estimate discharge by using width, slope and velocity. In this method, water surface velocity (converted to mean velocity) was used as a correction function instead of creating a new correction function. A test site was the Missouri River in Sioux City, Iowa. Water surface velocity was derived from interferometry airborne SAR. Estimation accuracy was improved as the estimated value was within ten percent of the observed value. The methods using remote sensing data to estimate discharge could be useful for a study area lacking ground-based data.

Knebl *et al.* (2005) developed a flood modeling framework including NEXRAD (weather radar) data, GIS and hydrological models (HEC-HMS and HEC-RAS) for San Antonio River Basin in Central Texas. Study period was June 30 – July 9, 2002 covering summer storm season

of the area. HEC-HMS, a rainfall-runoff model, was used to estimate overland flow and channel runoff from excess precipitation. HEC-HMS made a prediction based on 4×4 sq.km. spatial resolution according to input from NEXRAD. To calibrate HEC-HMS, predicted runoffs and predicted hydrographs were compared to observed data, and then, watershed parameters were manually adjusted for each subbasin. The calibrated model was used to estimate hydrological data, which later on were inputs of HEC-RAS to predict flooded areas. The predicted flooded areas were validated against flooded areas interpreted from a Landsat TM image, and then, a map illustrating matched, overestimated and underestimated areas was produced. From the Landsat data, it could be implied that actual infiltration and dispersal of runoff was faster than that represented in the model.

Bates *et al.* (2006) observed dynamic movement of flooded areas in the River Severn, west-central England during November 8-17, 2000 using 1.2 m spatial resolution airborne radar images. By combining series of inundated area data with topographic data (obtained from LiDAR), discharge, flooded area, reach storage and rate of reach dewatering since last image could be calculated. Comparison of these calculated data to those observed in the field yielded more insight into understanding of factors controlling flood pattern (such as local drainage networks, embankments and culverts). Furthermore, the flooded areas interpreted from the airborne radar images were used to validate ability of LISFLOOD-FP model to perform flood prediction. The study found that the model performed well during the peak flow (November 8), but performance decreased during low flow (November 17). This might be resulted from increasing influence of small-scale features (not represented at the model grid scale) during the low flow period.

Paz and Collischonn (2007) presented a new method to automatically extract length and slope of river reaches from a 90 m DEM produced by the Shuttle Radar Topography Mission (SRTM). The extracted data could be used as inputs of a large-scale raster-based hydrological model. In the study, the test site was the Uruguay River basin and the extracted outputs were validated against vector data of the river network. Quality of the extracted river length was improved using a stream burning method that conditioned the extracted river length by vector data of the river. Quality of calculated slope was not validated because no reliable slope data were available for comparison.

Schumann *et al.* (2007) used remote sensing data to estimate roughness value of each cross section in HEC-RAS, based on a concept that roughness values were spatially heterogeneous. The study site was River Alzette in Luxembourg. LiDAR derived DEM was used in the study. HEC-RAS was calibrated using data from the 2003 flood event ($70.5 \text{ m}^3/\text{s}$ peak discharge). Water levels were identified for 55 cross sections from integration of flood boundaries (interpreted from ENVISAT acquired near the time of peak discharge) and the DEM. By assessing model error at each cross section, local roughness and correlation between cross sections were analyzed. Roughness values at each cross section were adjusted, and this adjustment compensated for all kinds of errors in the prediction. The calibrated model was validated using flooded boundaries interpreted from ERS data acquired ten hours prior to the peak of the 2003 flood, and flood boundaries interpreted from aerial photos acquired during the 1995 flood that had a much higher peak discharge ($95.6 \text{ m}^3/\text{s}$). The study found that the calibrated model performed very well for both validation events. This indicated that the model calibration was robust because it was independent from different flood magnitudes and different

sources of remote sensing data. This study showed potential of remote sensing in flood model configuration.

Di Baldassarre *et al.* (2009) used a near real time Envisat image (C-band, VV, approximately 100 m resolution) to verify a flood simulation model, UNET (a package for unsteady flow calculation in HEC-RAS), and then made a prediction of the 2008 flood in a time shorter than the flood water travel time. The study site was a 98 km reach of the River Po in Italy. Topography data were derived from LiDAR and sonar. The flood simulation model was previously calibrated using data of the 2000 high magnitude flood, and absolute relative error between simulated and observed water surface did not exceed four percent. When a flood occurred in 2008, the authors received the near real time Envisat image, interpreted the inundation width, and made a flood prediction using the calibrated model. However, the prediction was not correct, which confirmed that a well calibrated model based on a flood event (the 2000 high magnitude flood, approximately 60 year return period) might give an incorrect prediction for another flood event (the 2008 low magnitude flood, three – four year return period).

According to these studies, remote sensing data have been used as direct inputs of flood models. Those data were DEM obtained from LiDAR (Bates and De Roo, 2000; Bates *et al.*, 2006; Schumann *et al.*, 2007; Di Baldassarre *et al.*, 2009), and channel topography from sonar (Di Baldassarre *et al.*, 2009). Remote sensing data also provided physical data of a basin, which were river network (Blyth, 1993; Paz and Collischonn, 2007), Slope (Schultz, 1988; Blyth, 1993; Paz and Collischonn, 2007), and land cover (Schultz, 1988; Blyth, 1993; Sharma *et al.*, 1996; Biftu and Gan, 2001). For some study areas lacking ground-based data, remote sensing data were utilized to estimate hydrological variables: precipitation (Schultz, 1988; Sharma *et al.*, 1996;

Knebl *et al.*, 2005), river discharge (Schultz, 1988; Sharma *et al.*, 1996; Bjerklie *et al.*, 2005; Knebl *et al.*, 2005), runoff (Sharma *et al.*, 1996; Biftu and Gan, 2001; Knebl *et al.*, 2005), soil moisture (Profeti and Macintosh, 1997; Biftu and Gan, 2001), and sensible heat flux (Fox and Collier, 2000). Remote sensing has proved to be useful for hydrological variable estimation. However, using optical sensor data to estimate surface temperatures and net radiation was reliable only on cloud-free days, while accuracy of soil moisture estimated from radar data was more consistent owing to atmospheric independence (Biftu and Gan, 2001).

Remote sensing has played a significant role in flood model calibration and validation. Both optical sensor (Knebl *et al.*, 2005; Schumann *et al.*, 2007) and radar data (Bates and De Roo, 2000; Bates *et al.*, 2006; Schumann *et al.*, 2007; Di Baldassarre *et al.*, 2009) have been used. Because flooding usually occurs during storm seasons, radar data were more popular due to cloud penetration ability. Furthermore, Townsend and Walsh (1998) and Toyra and Pietroniro (2005) recommended using radar images in flood model validation. However, when interpreting flooded areas from a radar image; ambiguity may happen due to waves on water surface, which usually occurs in the middle of rivers or large lakes. Horritt and Bates (2002) suggested that uncertainty areas in the middle of a river could be corrected using output from a flood model. Thus, flooded areas predicted by a flood model can be used to complement radar data (uncertainty is caused by waves) and optical sensor data (uncertainty is caused by clouds).

In a study of Profeti and Macintosh (1997), outputs from a hydrological model were used to validate soil water content calculated from different band ratios of Landsat TM data. This is an example that a model can be used to determine a suitable method to obtain information from remote sensing. Also, Lang *et al.* (2008) used flood extents calculated by a flood simulation model of Roanoke River floodplain to verify flood extents interpreted from Radarsat images.

Only Radarsat flood extents in agreement with the model outputs were used to detect flood underneath forest canopies. Likewise, in my study, flooded areas simulated by HEC-RAS were used to validate flooded areas interpreted from two Radarsat images. An image yielded higher classification accuracy of flooded and non-flooded areas was deemed the best Radarsat image in my study, and was then selected to be an input in the image fusion.

According to previous studies, there is no research that fuses Landsat, IRS and Radarsat data acquired during the same flood event. Therefore, fusion of these data to create an image illustrating the flood situation is necessary. When a flood occurs, information of flood boundaries, flooded transportation routes, and damaged areas are necessary to provide a range of helps and compensation. This information could be obtained from a fused image of Landsat, IRS and Radarsat through PCA and pan-sharpening techniques. A flood map calculated by HEC-RAS was used to validate flooded areas interpreted from Radarsat W1 and Radarsat S7 images.

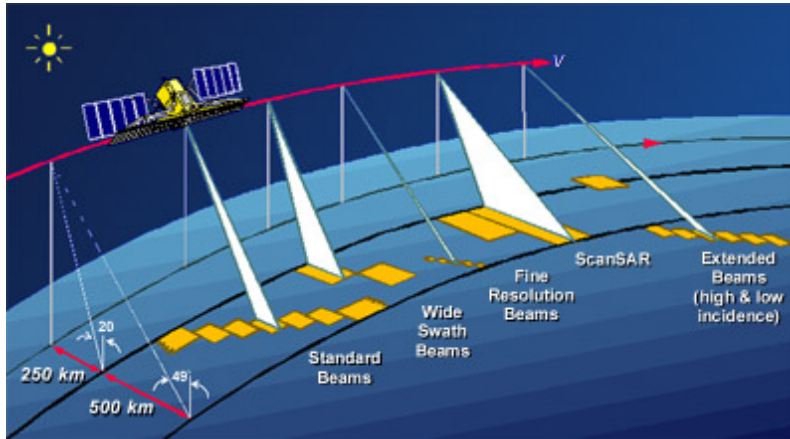


Figure 2-1. Radarsat imaging modes. (Source: <http://www.asc-csa.gc.ca/eng/satellites/radarsat1/components.asp>. Last date accessed November 2008).

Table 2-1. Sensors and bands of Landsat-1 to 7

Sensor	Satellite	Band number	Spectral band	Wavelength (μm.)	Spatial resolution (m.)
MSS	Landsat-1 to 5	4	Green	0.5-0.6	80
		5	Red	0.6-0.7	80
		6	Near infrared	0.7-0.8	80
		7	Near infrared	0.8-1.1	80
TM	Landsat-4 to 5	1	Blue	0.45-0.52	30
		2	Green	0.52-0.60	30
		3	Red	0.63-0.69	30
		4	Near infrared	0.76-0.90	30
		5	Mid infrared	1.55-1.75	30
		6	Thermal infrared	10.4-12.5	120
		7	Mid infrared	2.08-2.35	30
ETM+	Landsat-7	Same as TM	Same as TM	Same as TM	30, 60 for thermal band
			Panchromatic	0.52-0.90	15

Table 2-2. Description of Radarsat imaging modes

Mode	Nominal resolution (m.)	Number of positions/beams	Swath width (km.)	Incidence angles (degrees)
Fine	8	15	45	37-47
Standard	25	7	100	20-49
Wide	30	3	150	20-45
ScanSAR narrow	50	2	300	20-49
ScanSAR wide	100	2	500	20-49
Extended high	18-27	3	75	52-58
Extended low	30	1	170	10-22

CHAPTER 3 MATERIALS AND METHODS

Spatial Data

Satellite Imageries

Satellite imageries used in my study were sponsored by GISTDA, a major data provider of Landsat, SPOT, IRS, and Radarsat in Thailand. Ideally, Landsat, SPOT, IRS, and Radarsat images covering a flooded area in the Northeast of Thailand acquired on the same date were needed. However, the probability of achieving this ideal is low. This is largely due to cloud cover, which typically accompanies a flood event. Therefore, an attempt was made to find the narrowest range of image dates in order to minimize the effects the temporal variation. Also, processing techniques were used in the analysis to mitigate these effects. Among the available sensors, Radarsat plays the most important role in flood detection in monsoonal areas. Therefore, the availability of Radarsat data was checked first. Unlike those optical sensors that continuously acquire data, Radarsat acquires data only when it is programmed in advance. As a result, archived Radarsat data were available for certain areas in certain times according to requests in the past. Fortunately, the archive had several images with different imaging modes and incidence angles illustrating flooding in the study area since 2002.

Next, the availability of Landsat, SPOT and IRS data was investigated for images taken on the same dates as the available Radarsat images. In the investigation, it was found that cloud contamination was a serious problem for the optical sensor data taken during rainy seasons, and there were no optical data taken on the same date of the Radarsat that has acceptable cloud cover. However, on October 14, 2002 the sky was clear and IRS-1D obtained data over the study area, and on October 25, 2002, the sky was partly clear, and the flooded area could be seen from Landsat-7 image. No SPOT image, however, was available during this period. As a result, the

images used in my study were Radarsat-1 (W1), IRS-1D, Radarsat-1 (S7) and Landsat-7 acquired during October 11-25, 2002.

On October 11, 2002, Radarsat-1 acquired data of the study area in W1 mode at 25° incidence angle with 30 m spatial resolution using C-band and HH polarization. The original data were stored in 16-bit unsigned format. A full scene image of the Radarsat W1 is shown in Figure 3-1.

On October 14, 2002, atmospheric conditions over the study area were clear enough for IRS-1D to acquire data. A full scene image of path 125, row 62 of IRS-1D in a false color composite is illustrated in Figure 3-2. In my study, all bands of LISS-III sensor (green, red, near infrared, and mid infrared) with 23 m spatial resolution, and a panchromatic image with 5.8 m resolution were used. The original data were stored in 8-bit unsigned format.

On October 15, 2002, Radarsat-1 obtained data in S7 mode at 47° incidence angle, 25 m spatial resolution, and 16-bit unsigned pixel depth. A full scene image of the Radarsat S7 (C-band, HH polarization) is shown in Figure 3-3.

On October 25, 2002, Landsat-7 acquired data of the study area. At that time, a storm hit the Northeast of Thailand, but sky over the study area was clear enough to identify flooded areas. A full scene image of Landsat (path 127, row 49) covering the study area in a false color composite is shown in Figure 3-4. All bands of ETM+ sensor were used in my study. The original data were stored in 8-bit unsigned format.

GIS Data

A land cover layer used in my study was supported by Department of Environmental Quality Promotion, Ministry of Natural Resources and Environment, Thailand. Scale of this layer is 1:50,000 referencing UTM projection, and Indian 1975 datum.

Other GIS layers such as administration boundary, transportation, river network, and river basin boundary were supported by Computer Center, Khon Kaen University, Thailand. These data were created based on 1:50,000 map scale, UTM projection, and Indian 1975 datum.

A DEM with metric vertical units and 30 m pixel size referencing UTM projection and Indian 1975 datum was supported by GISTDA. A set of 1:50,000 digital topographic maps (UTM, WGS 1984) covering the study area were also supported by GISTDA (Figure 3-5).

Hydrological Data and HEC-RAS Model

For my study, the Royal Irrigation Department of Thailand provided river cross section and daily hydrological data: discharge (m^3/s) and water surface elevation (m above mean sea level). Data stored in text files were collected at hydrological stations along the Mun and Lam Sieo Yai Rivers (Figure 3-6).

HEC software used in my study were HEC-GeoRAS version 4.1.1 for ArcGIS 9.1 and HEC-RAS version 4.0 Beta, downloaded from U.S. Army Corps of Engineers' website (<http://www.hec.usace.army.mil/software/hec-ras/>). The website also provided a set of practical manuals, such as HEC-GeoRAS user's manual, HEC-RAS user's manual, Hydraulic reference manual and HEC-RAS application guide.

Data Preprocessing

Data were manipulated in raster-based environment of Erdas Imagine software and vector-based-environment of ArcGIS software. In raster-based environment, all satellite imageries and the DEM were co-registered (Figure 3-7, upper part), but for Radarsat images, speckle noise was suppressed before the registration. In vector-based environment, geometry data of HEC-RAS were prepared using ArcGIS software and exported to HEC-RAS for water surface elevation calculation, and then, a HEC-RAS flood map was produced (Figure 3-7, upper right portion). The HEC-RAS flood map was used to validate two flood maps interpreted from

Radarsat W1 and S7 images to determine best Radarsat image in my study, which was objective 2 (Figure 3-7, middle portion). The best Radarsat image was an input of a pan-sharpening process, while three other input images were IRS panchromatic image and two images from PCA, which input data were Landsat and IRS multispectral (Figure 3-7, middle left portion). The fused image was then created. By using unsupervised classification, a flood map was interpreted from the fused image, which was objective 1 (Figure 3-7, lower left portion). The fused image flood map and the best Radarsat flood map were validated against my visual interpretation, which was objective 3 (Figure 3-7, bottom right portion). To detect under-water features (objective 4), areas in flooded zone were compared to land cover layer to determine relationship between colors in the fused image and land cover types (Figure 3-7, bottom left portion).

Data preprocessing was divided into three parts: speckle noise suppression, geometric correction and HEC-RAS data preparation. The first two processes were done in raster-based environment, while the last was done in vector-based environment.

Speckle Noise Suppression

Like other radar images, the Radarsat images used also have speckle noise. By using a radar speckle suppression module in Erdas Imagine software, this noise was reduced. Erdas Imagine provides seven speckle noise filters: mean filter, median filter, Lee-sigma filter, local region filter, Lee filter, Frost filter and Gamma map filter.

A study of Yongwei and Zong-Guo (1996) evaluated performance of the seven speckle noise filters in Erdas Imagine using five criteria: speckle suppression index, edge enhancing index, feature preserving index, image detail preserving coefficient, and speckle image statistical analysis. They found that Frost and Lee filters were good in preserving edges and features, but the Frost filter had lowest ability in speckle suppression. Therefore, the Lee filter was chosen to

be applied because it can suppress speckle and preserve edges of wet and dry areas, which is most important for flood delineation.

Geometric Correction

To avoid discrepancy in the fused image, all images used must be tightly fitted to each other. Thus geometric correction is a very important step. First of all, the panchromatic image of IRS was geometrically corrected referencing 1:50,000 digital topographic maps (UTM, WGS84), as shown in top left portion of Figure 3-7. In the rectified panchromatic image, linear features (such as roads and man-made channels) were more up to date than in topographic maps. These obvious features made finding ground control points (GCPs) easier. As a result, the rectified panchromatic image was used as a reference to register IRS multispectral, Landsat and Radarsat images, and DEM. First order polynomial coordinate transformation was applied to all images and the DEM due to the flat topography in the study area. Bicubic spline resampling method was used to avoid a blocky appearance in rectified images. Table 3-1 describes root mean square (RMS) residual errors of the GCPs in the rectification of IRS panchromatic and multispectral, Landsat, Radarsat W1 and S7 images, and DEM. Total RMS error of each rectification was less than half pixel of input data.

Rectified IRS multispectral and Landsat images were input in PCA later on (middle left portion of Figure 3-7). Because PCA requires equal pixel size for all inputs, pixel size of rectified IRS multispectral (originally 23 m) and Landsat (originally 30 m) was changed to five m during the registration process. For the radar images, the pixel size of the Radarsat W1 (30 m) and Radarsat S7 (25 m) did not change because these images were later on classified to produce flood maps (middle portion of Figure 3-7). The original spatial resolution of these Radarsat images was one factor considered when their ability to illustrate flooded areas was evaluated. However, the pixel depth of the Radarsat images was changed from 16 bits to eight bits to reduce

data volume. Moreover, one of these Radarsat images was an input in a pan-sharpening process (middle left portion of Figure 3-7) requiring same pixel depth for all inputs, and pixel depth of other inputs (IRS panchromatic and principal component images) was eight bits. After the geometric correction, all satellite images (IRS panchromatic and multispectral, Landsat, and both Radarsat W1 and S7 images) and DEM were tightly fit to each other.

HEC-RAS Data Preparation

Input data for HEC-RAS are geometry and steady flow data. Geometry data were prepared in ArcGIS environment, but steady flow data (discharge and water surface elevation) were directly input in HEC-RAS software (top right portion of Figure 3-7). HEC-GeoRAS, an ArcGIS extension, was used to prepare geometry data. These included stream center lines, bank lines, flow path center lines, cross section cut lines, and roughness coefficients according to land cover categories.

Stream center lines were digitized from upstream to downstream according to a topology rule of HEC-RAS. A junction was formed where endpoints of three or more rivers/reaches connected. Next, the stream center lines were copied as a flow path of the main channel. Left and right bank lines were also digitized, but direction of these lines was not important.

Cross section cut lines were generated using an XS Cut Line tool in HEC-GeoRAS. These lines started from left overbank to right overbank when facing downstream, and were perpendicular to the flow path lines. Next, length of the cross section cut lines was manually adjusted to cover the floodplain. In this step, all rectified satellite imageries were used as backgrounds to estimate the flood boundary. Some cross section cut lines were modified to comply with rules of HEC-RAS (cut lines must cross the main channel only once, and cross section cannot intersect each other), as shown in Figure 3-8 A. Elevations of cross section surfaces were generally extracted from the DEM, except for cross sections at hydrological

stations, where elevation data were available. Figure 3-8 B shows a profile of a cross section in a circle of Figure 3-8 A.

Roughness coefficients used in HEC-RAS are values of Manning's n estimated using land cover data. Manning's n of each land cover type applied was estimated based on values proposed by Chow (1959). For example, Mun River was comparable to main channel (clean, winding, some pools and shoals), thus Manning's n was estimated to be 0.040. Estimated Manning's n value for each land cover type applied in my study is shown in Table 3-2. After geometry data were ready, these data were exported from ArcGIS, and then imported to HEC-RAS for calculation of water surface elevation later on.

Data Analysis

Calculation of Water Surface Elevation Using HEC-RAS

HEC-RAS calculates water surface elevation using geometry and steady flow data. Geometry data included stream center lines, bank lines, flow path center lines, cross section cut lines and roughness coefficients (Manning's n). After using HEC-GeoRAS to create geometry data in the ArcGIS environment, data were then imported to HEC-RAS (top right portion of Figure 3-7). If number of elevation points at a cross section was more than 500, exceeding the HEC-RAS limitation, those elevation points were filtered using cross section point filter, a tool in geometric data section. In addition, if number of values of Manning's n at a cross section was more than 20, then values covering a small area farthest from the main channel were manually deleted. In other word, small land cover areas were merged into larger land cover type dominating that area.

Steady flow data for HEC-RAS were (1) average daily discharge collected on October 11 and 15, 2002, and (2) average daily water surface elevation collected on October 11 and 15, 2002. The average values were representatives of hydrological data of October 11 and 15, 2002,

when Radarsat W1 and S7 images were acquired consecutively. A flood map calculated by HEC-RAS was later compared to flood maps interpreted from Radarsat W1 and S7 images (objective 2 of my study), as shown in middle right portion of Figure 3-7).

In HEC-RAS, each reach must have at least one discharge data point, but in my study, some reaches did not have hydrological station, and consequently no discharge data. As a result, discharge values were estimated using addition of upstream discharges because conservation of mass was assumed and the flow regime was assumed steady (no temporal change in velocity). After a discharge value was entered for each reach, HEC-RAS assumed that discharge remained constant for a reach. Next, water surface elevation at the downstream ends of the river system was entered. Additional data, such as known water surface elevations at hydrological stations, were also entered.

Computational starting point was a cross section at the downstream end of the river system. HEC-RAS computed water surface elevation from one cross section to the next one upstream using the standard step method. During computation, HEC-RAS did not compute water surface elevation of cross sections where water surface were previously entered. The program used the known water surface to calculate water surface elevation of the next upstream cross section. The calculation process continued until water surface elevation of every cross section was computed.

After the calculation was finished, the result was exported from HEC-RAS to HEC-GeoRAS. The data were stored in an ArcGIS geodatabase. The calculated water surface elevation was stored as an attribute at each cross section cut line. Next, water surface Triangulated Irregular Network (TIN) was generated using the data from each cross section. To create a flood map, the water surface TIN was overlaid with the 30 m DEM. The flood map was

in raster format with the same ground cell size of DEM. Afterward, the flood map calculated by HEC-RAS was used as a reference in a comparison of flood maps interpreted from Radarsat W1 and S7 images (middle right portion of Figure 3-7).

Radarsat Image Interpretation

To identify wet and dry pixels in Radarsat W1 and S7 images, a threshold value of each image was determined using histogram investigation. If the DN of a pixel was less than or equal to the threshold, that pixel was classified as a wet (flooded), and otherwise a dry (non-flooded) pixel when its DN was bigger than the threshold.

For the Radarsat W1 image, the histogram distribution is nearly bimodal, as shown in Figure 3-9. The first mode with a lower DN represents wet areas, where water surface was a specular reflector reflecting radar signal away from the antenna. The second mode with brighter tone (higher DN) represents dry areas, which were diffuse reflectors returning large proportion of microwave energy to the antenna. In the classification, threshold values from 16 to 25 were tested because from the histogram, these values were potential thresholds separating between wet and dry areas. After these thresholds were used to classify wet and dry areas, visual evaluation was used to identify an appropriate threshold. The tested thresholds smaller than 20 were not suitable because many wet pixels in water bodies were misclassified as dry pixels. The tested threshold bigger than 20 were not suitable because plenty of pixels representing shadow of forest canopy in high land areas were misclassified as wet pixels. As a result, 20 was deemed the most appropriate threshold to discriminate between wet and dry areas in the Radarsat W1 image.

For the Radarsat S7 image, the histogram distribution is bimodal representing wet and dry areas (Figure 3-10). Threshold values from 18 to 27 were tested, and visual evaluation was used to identify an appropriate threshold. It was found that 24 was the most suitable threshold to separate between wet and dry areas in the Radarsat S7 image.

After two flood maps were interpreted from Radarsat W1 and S7 images, they were compared to the HEC-RAS flood map (reference data), and error matrix and Kappa statistics were calculated. This comparison of flood maps derived from Radarsat W1 and S7 images to the HEC-RAS result constitutes objective 2 of my study.

In the classification accuracy assessment, a stratified random sampling method was used to place 250 sample points in each class (wet and dry). A Radarsat image that yielded higher classification accuracy of flooded areas was deemed the best Radarsat image in my study. Then, it was selected as an input in a pan-sharpening process (middle portion of Figure 3-7).

PCA

Due to the high spectral redundancy in Landsat and IRS data (Figure 3-11), PCA was applied to compress data into fewer bands. Inputs of PCA were the IRS multispectral acquired on October 14, 2002 and Landsat acquired on October 25, 2002 data (upper left portion of Figure 3-7). These images were acquired on different dates. Thus outputs from PCA did not only show compressed data, but also showed changes detected during the twelve-day period. Output images from the PCA were separately analyzed as black and white images. A principal component image that showed the clearest boundary of flood extent was selected to be an input in the pan-sharpening. Another principal component image that showed the greatest variation in gray levels over flooded areas was chosen to be another input for pan-sharpening.

Pan-sharpening

Inputs of the pan-sharpening process were (1) the best Radarsat image that yielded the highest classification accuracy of the flooded areas comparing to HEC-RAS results, (2) the principal component image that clearly showed flood boundaries, (3) the principal component image that showed various gray levels in flooded areas and (4) the IRS panchromatic image (middle left part of Figure 3-7). A color image combining the best Radarsat image and two

principal component images was transformed from RGB to IHS color model. The intensity component was replaced by the IRS panchromatic image, and then the image in IHS color model was transformed back to RGB color model. The result was a fused image containing data of IRS, Landsat, and Radarsat with five m spatial resolution.

Classification of Fused Image

To classify the fused image, unsupervised classification was used to obtain 250 classes. These classes were manually grouped into eleven land cover classes comparing to the IRS, Landsat and Radarsat images, and QuickBird images acquire during January – February 2006 in GoogleEarth. A 7×7 median filter was applied to the classified image, and any area smaller than 30×30 m (Landsat pixel size that was the largest pixel size of the input data) was eliminated from the classified image. Finally, classification of the fused image was obtained. Of the eleven land cover classes was water body and flooded area. This class represented flood water extent delineated from the fused image, which was objective 1 in my study (lower left portion of Figure 3-7).

Next, flooded areas interpreted from the fused image were compared to flooded areas interpreted from the best Radarsat image, and my visual interpretation based on the IRS, Landsat and Radarsat images was used as a reference. In this step, a HEC-RAS flood map was not suitable to be used as a reference because the fused image included data acquired during October 14-25 (twelve-day period), whereas the best Radarsat image (later found to be Radarsat S7) was acquired on October 15, and using a HEC-RAS flood map of October 19 or 20 (mid-point of the twelve-day period), or October 15 (acquisition date of the Radarsat S7 image) was not well represent the flood during that period. On the other hand, visual interpretation and flood movement knowledge was more suitable to be used as the reference.

In the classification of the best Radarsat image, stratified random sampling method was used to place 250 sample points in each class (wet and dry). By using coordinates of these sample points, their locations could be identified in IRS, Landsat, and Radarsat S7 images, and then visual interpretation was used to identify if the sample points fell in wet or dry areas. Next, an error matrix, classification accuracies and Kappa statistics were calculated. This method was also used to assess classification accuracy of the fused image. Next, classification accuracies and Kappa statistics of the fused image were compared to those of the best Radarsat image to determine if classification accuracy of flooded areas derived from the fused image was higher than that from the best Radarsat image alone, which was objective 3 of my study (lower right portion of Figure 3-7).

According to objective 4 of my study, identifying underwater features were expected to be a derivative of the fused image. Areas within flood boundaries were scrutinized comparing to the land cover layer to identify underwater features (bottom left portion of Figure 3-7). The principal component image that showed various gray levels in flooded areas and the best Radarsat image showing water surface roughness were anticipated to provide information of underwater features.

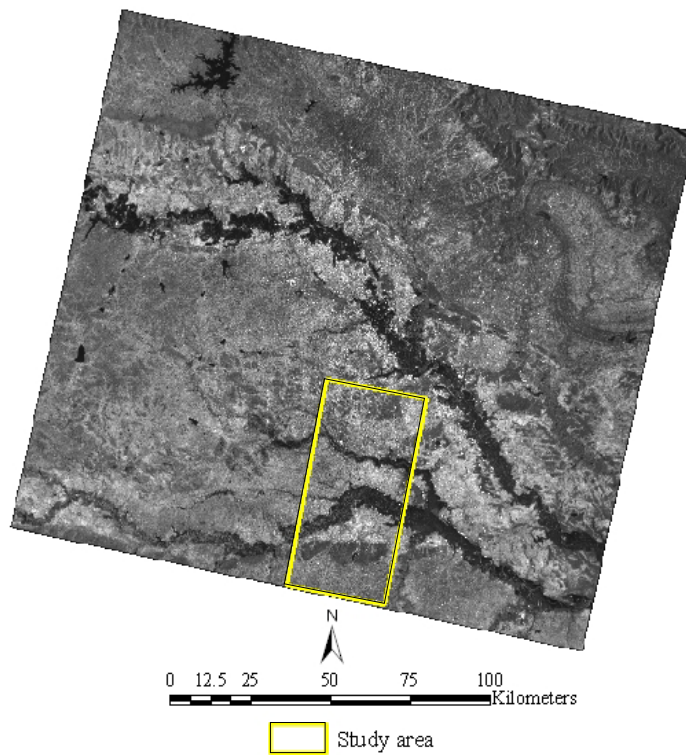


Figure 3-1. Radarsat W1 image taken on October 11, 2002 at 25° incidence angle, 30 m resolution.

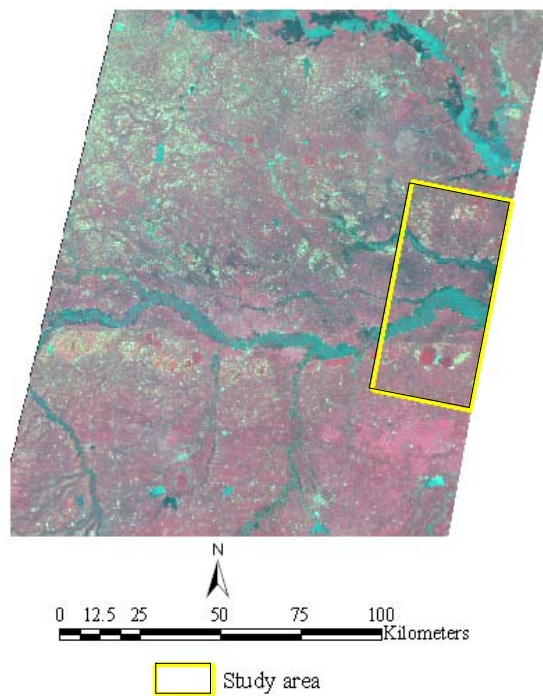


Figure 3-2. IRS-1D image taken on October 14, 2002, 23m resolution.

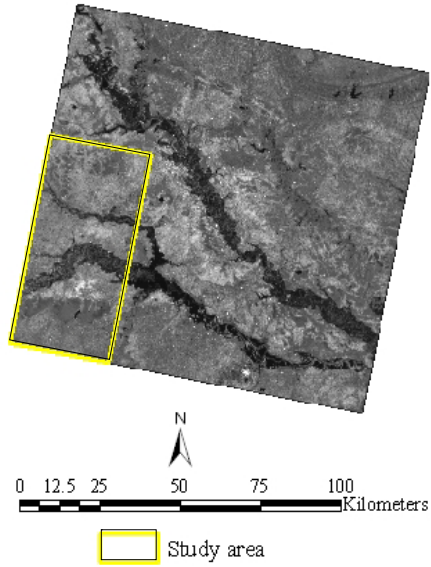


Figure 3-3. Radarsat S7 image taken on October 15, 2002 at 47° incidence angle, 25 m resolution.

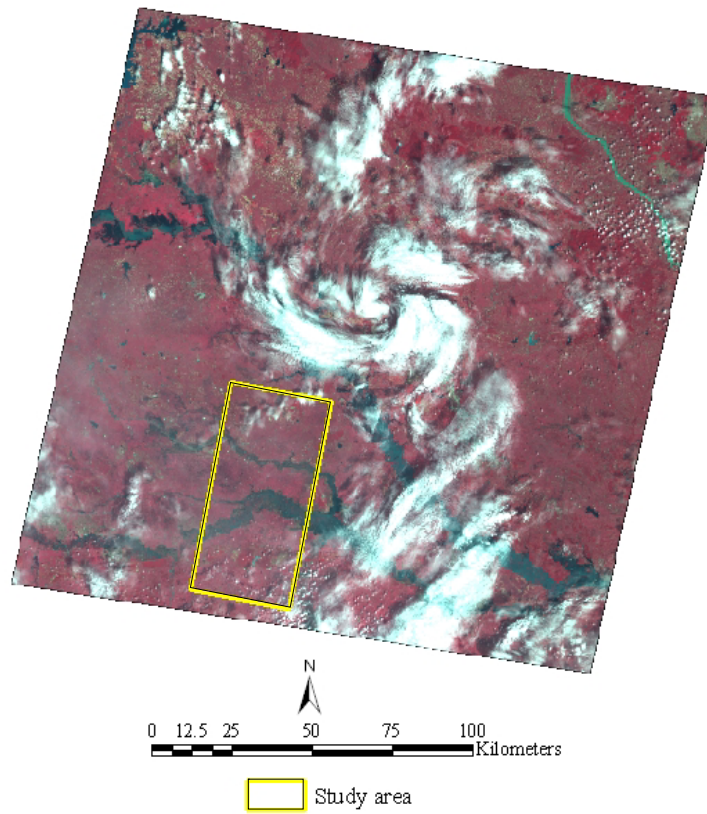


Figure 3-4. Landsat-7 image taken on October 25, 2002, 30 m resolution.

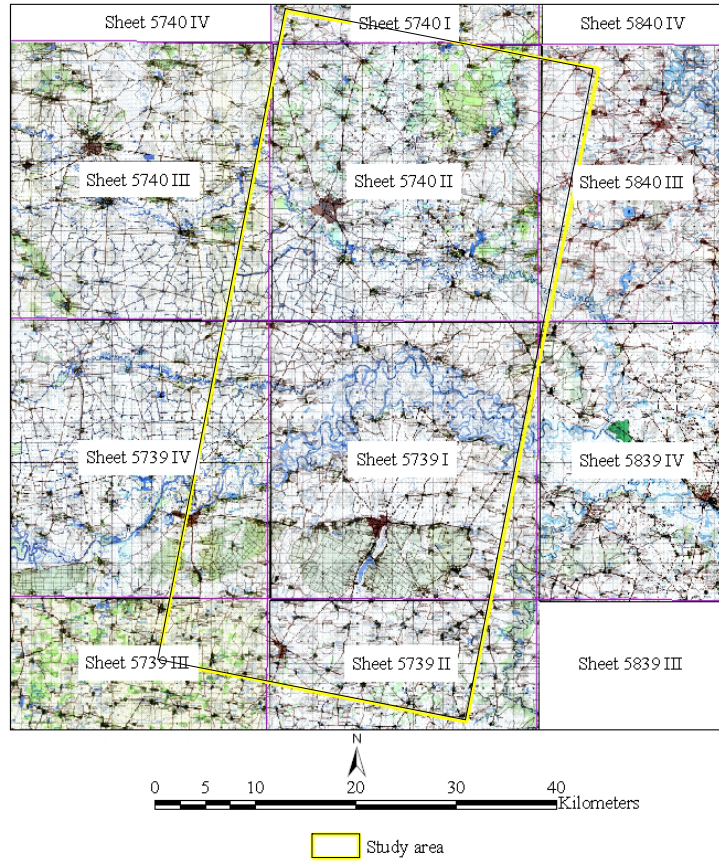


Figure 3-5. Topographic maps.

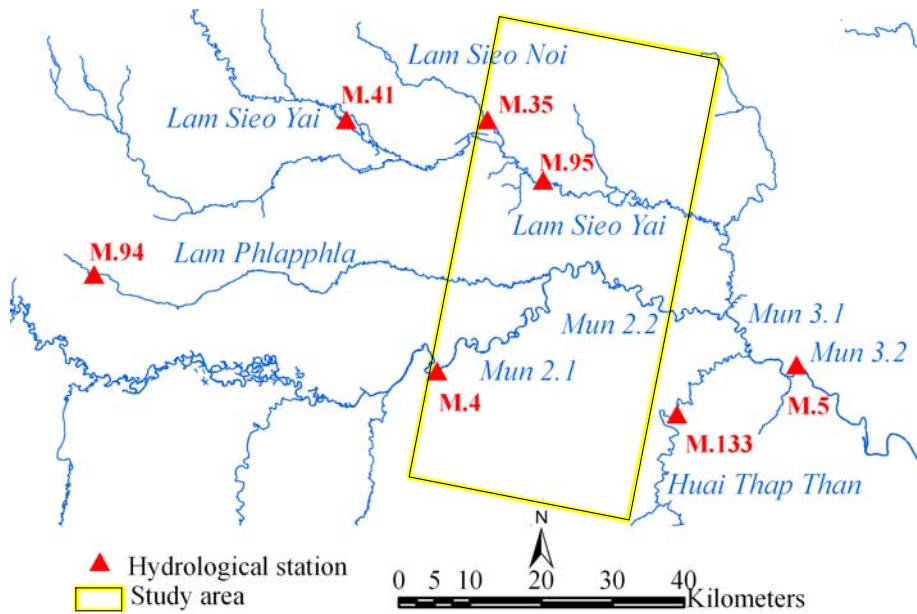


Figure 3-6. Hydrological stations.

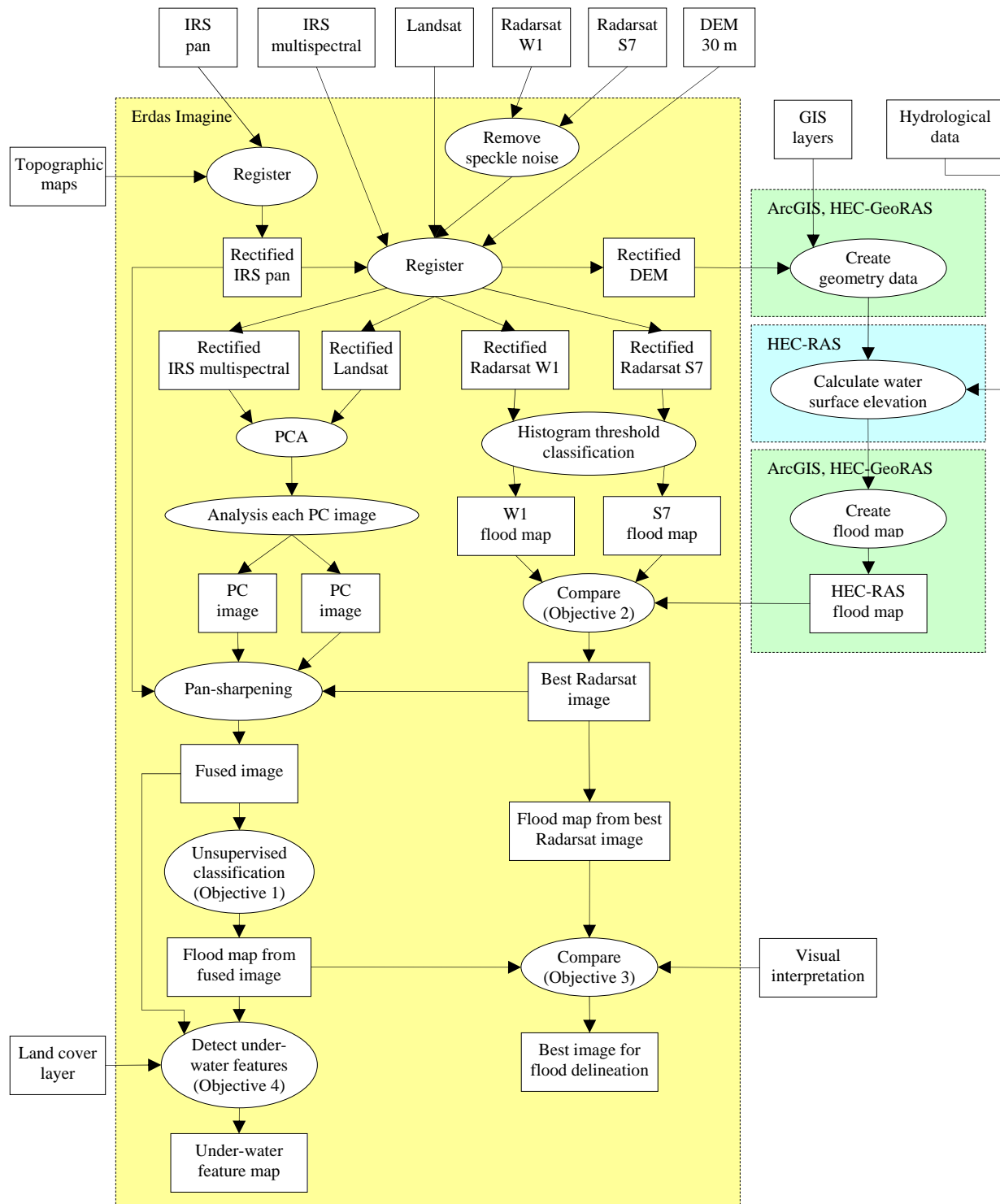


Figure 3-7. Flowchart of my study.

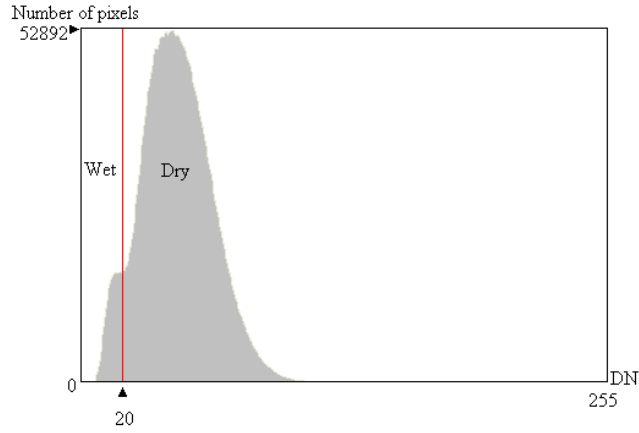


Figure 3-9. Histogram of Radarsat W1. Threshold of 20 between wet and dry pixels is shown.

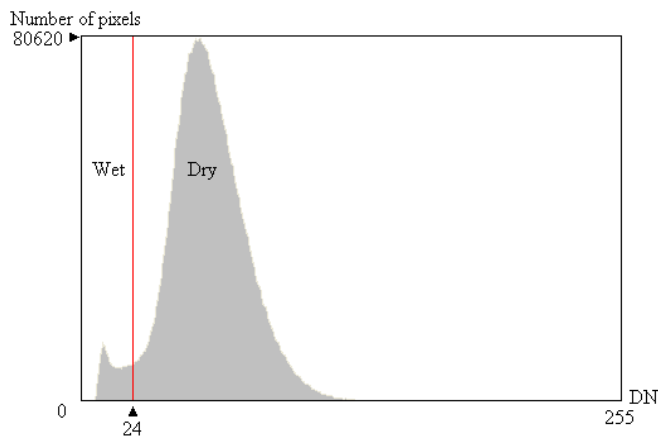


Figure 3-10. Histogram of Radarsat S7. Threshold of 24 between wet and dry pixels is shown.

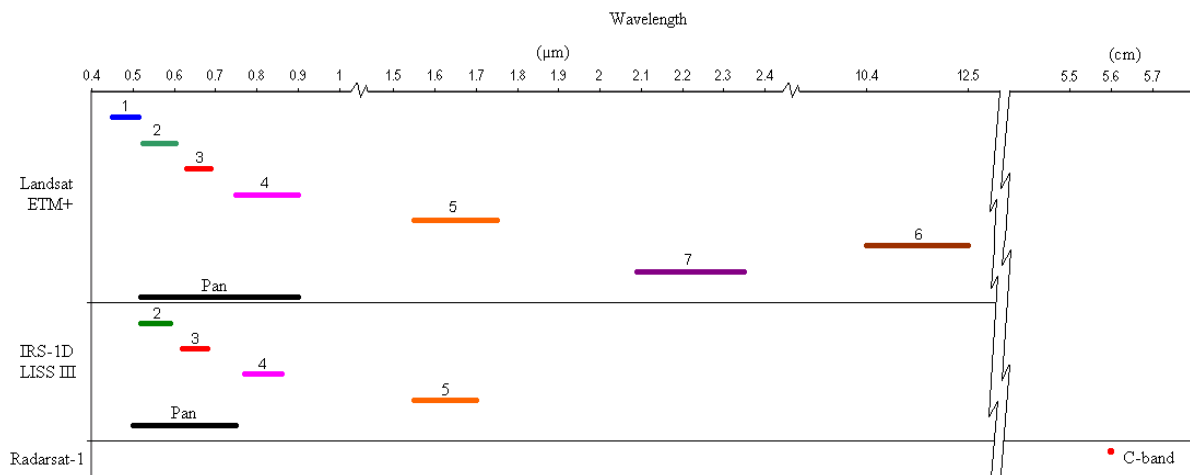


Figure 3-11. Spectral bands of Landsat-7, IRS-1D and Radarsat-1 showing high redundancy in Landsat and IRS spectral bands.

Table 3-1. RMS residual errors of the GCPs

Data	Input cell size (m)	Number of GCPs	RMS residual errors (m)			Output cell size (m)
			X	Y	Total	
IRS panchromatic	5.8	419	1.72	1.65	2.48	5
IRS multispectral	23	413	3.89	3.99	5.57	5
Landsat	30	378	6.04	5.27	8.01	5
Radarsat W1	30	175	4.49	4.20	6.15	30
Radarsat S7	25	158	2.44	2.49	3.48	25
DEM	30	17	4.02	3.93	5.62	30

Table 3-2. Estimated Manning's n values (adapted from Chow, 1959)

Land cover	Manning's n	Comparable to
Built-up area	0.017	Unfinished concrete
Grass land	0.030	Short grass
Non-forested wetland	0.030	Short grass
Paddy field	0.035	High grass
Horticulture	0.035	Mature row crops
Field crops	0.040	Mature field crops
Water body	0.040	Natural streams, clean, winding, some pools and shoals
Orchard	0.080	Heavy stand of timber, a few down trees, little undergrowth, flood stage below branches (minimum Manning's n value)
Forest plantation	0.080	Heavy stand of timber, a few down trees, little undergrowth, flood stage below branches (minimum Manning's n value)
Riverine trees	0.100	Heavy stand of timber, a few down trees, little undergrowth, flood stage below branches (normal Manning's n value)
Deciduous forest	0.100	Heavy stand of timber, a few down trees, little undergrowth, flood stage below branches (normal Manning's n value)
Forested wetland	0.100	Heavy stand of timber, a few down trees, little undergrowth, flood stage below branches (normal Manning's n value)

CHAPTER 4 RESULTS

HEC-RAS and HEC-GeoRAS Results

A result from HEC-RAS was a calculated water surface elevation. This output was stored as an attribute of each cross section line. To create a flood map, the calculated water surface elevation was exported from HEC-RAS, and then imported to HEC-GeoRAS in ArcGIS environment. Next, water surface elevation data at each cross section line was used to create a water surface TIN, which was then overlaid with the 30 m DEM and finally the HEC-RAS flood map was created. Flooded areas and water surface elevation simulated by HEC-RAS were shown in Figure 4-1. The flooded areas were within coverage of cross section lines.

Flood Maps Interpreted from Radarsat Images

Radarsat W1 and S7 images (Figure 4-2, A and B respectively) were classified using threshold values of 20 and 24 respectively, and flood maps were produced. The ground cell size of the flood map interpreted from Radarsat W1 image was 30 m, while that interpreted from Radarsat S7 was 25 m according to pixel size the original images. Figure 4-3 shows overlaid flooded areas interpreted from the Radarsat W1 and S7 images and those simulated by HEC-RAS.

Comparison of Radarsat Flood Maps Referencing HEC-RAS Flood Map

To compare the flood maps interpreted from the Radarsat W1 and S7 images, the HEC-RAS flood map was used as a reference. In the Radarsat W1 and S7 flood maps, flooded areas outside the floodplain were masked out because coverage of the HEC-RAS flood map was the floodplain area (within the coverage of cross section lines).

In the Radarsat W1 flood map, 250 sample points were randomly placed in areas classified as wet, and other 250 sample points were randomly placed in areas classified as dry. Locations of

these 500 sample points were projected on the HEC-RAS flood map (the reference data) to evaluate classification accuracy of the Radarsat W1, and then, an error matrix, classification accuracies and Kappa statistics were calculated. This method was also applied to evaluate classification accuracy of the Radarsat S7 image.

For the classification of the Radarsat W1 image, overall classification accuracy was 87.60%. Because the primary purpose of my study was to map flooded areas, wet category was in focus. Producer's accuracy of the wet category was 95.63% that was 95.63% of flooded areas was correctly identified as wet areas. User's accuracy of the wet category was 78.80% that was only 78.80% of pixels classified as wet were really wet areas (Table 4-1 and 4-2). Kappa value of the wet class was 0.6395 (Table 4-3) that was classification of flooded areas was 63.95% better than randomly classify pixels as wet pixels. The overall Kappa statistic was 0.7520 (this classification was 75.20% better than a random classification).

For the classification of the Radarsat S7 image, overall classification accuracy was 94.00%. For the wet category, producer's accuracy was 97.01%, and user's accuracy was 90.80%, which were 97.01% of wet areas were correctly identified, and 90.80% of pixels classified as wet were truly wet (Table 4-4 and 4-5). Kappa value of the wet class was 0.8271 (Table 4-6) that was classification of flooded areas was 82.71% better than a random classification. The overall Kappa statistic was 0.8800 (this classification was 88.00% better than a random classification).

Considering only the wet class (flooded), producer's and user's accuracies of the Radarsat S7 classification were higher than those of the Radarsat W1 classification. Moreover, kappa value of the wet class and the overall kappa statistic of the Radarsat S7 classification were higher than those of the Radarsat W1 classification. Thus, the Radarsat S7 image yielded higher

classification accuracies of flooded areas than the Radarsat W1 image referencing the HEC-RAS flood map, and objective 2 of my study was completed. The Radarsat S7 image was then chosen to be an input of pan-sharpening process.

PCA Results

Outputs of the PCA were 12 black and white images because inputs of PCA were four bands of IRS and eight bands of Landsat data. False color composite images of IRS and Landsat, input data of the PCA, are shown in Figure 4-4, A and B respectively. Eigen values and eigen vectors were shown in Table 4-7. Eigen values were used to calculate percentage of the total scene variance of each principal component, shown in Table 4-8. PC1 image contained 63.53% of the total scene variance, while PC2, PC3, ..., PC12 contained successively smaller percentages.

In PC1 image (Figure 4-5, A), flooded areas appeared as dark areas, while dry areas and clouds appeared as brighter tone. This image clearly showed flood boundaries. For PC2 image that contained 21.32% of the total scene variance (Figure 4-5, B), flooded areas and clouds appeared as dark areas causing confusion in flood delineation. PC3 image contained 6.22% of the total scene variance (Figure 4-5, C). Both flooded areas and dry areas appeared as bright tone and flood boundaries were not obvious. Road networks were obvious in this image. For PC4 image that contained 4.91% of the total scene variance (Figure 4-5, D), details in flooded areas were illustrated. There were various gray levels in the floodplain and the meandering river (dark tone) was differentiated from its surroundings.

The PC1, PC2, PC3 and PC4 explained 95.98% of the variance in the Landsat and IRS images. PC5 to PC12 images contained only 4.02% of the total scene variance. Although PC5 to PC12 images were individually examined, no image showed flood boundaries or details in flooded areas.

Among the principal component images, the PC1 image showed the most obvious flood boundary, while the PC4 showed details in the flooded areas. As a result, the PC1 and PC4 images were selected to be inputs of the pan-sharpening. Although the PC3 showed obvious road networks, it was not chosen because the IRS panchromatic image illustrated road networks better.

Fused Image and Its Classification

In order to create a fused image containing all necessary information about flooding, the Radarsat S7, PC1 and PC4 images were selected, and then were sharpened by five m IRS panchromatic image. The fused image of PC4 (in red), Radarsat S7 (in green), and PC1 (in blue) is shown in Figure 4-6.

The fused image was classified into 250 classes and finally grouped into eleven land cover classes including water body and flooded area, paddy field, field crops, orchard, horticulture, forest plantation, deciduous forest, forested wetland, non-forested wetland, built-up area, and dead vegetation, as shown in Figure 4-7. The water body and flooded area class represented flooded areas delineated from the fused image, which was objective 1 of my study.

Dead vegetation appears in the fused image because during October 11-25, 2002 (when Radarsat, IRS, and Landsat acquired the data) water surface elevation of the Mun River decreased gradually (Figure 4-8). On October 14, 2002 when IRS acquired the data, water surface elevation was approximately one m higher than that on October 25, 2002 when Landsat acquired the data. As a result, some flooded areas in the IRS image were exposed dead vegetation in the Landsat image. In the IRS image (Figure 4-9, A) roads and villages are in bright tone, paddy field appears as red, and flooded area appears in darker tone. After flood water receded, dead vegetation exposed. An example of dead vegetation area is area X in the Landsat image (Figure 4-9, B). Also, a built up water body (area Y) can be seen from the

Landsat image. After applied PCA to the IRS and Landsat data, dead vegetation showed as a very bright tone in PC4 image (area X in Figure 4-9, C). In Radarsat S7 and PC1 images (Figure 4-9, D and E respectively), dead vegetation (area X) is not different from its surroundings, but the built up water body (area Y) is obvious. After the PC4, Radarsat S7, and PC1 images were assigned in red, green, and blue channels respectively, dead vegetation became visible as red areas in the fused images (area X in Figure 4-9, F, for example). The built up water body is visible in the fused image (area Y). A row of trees that appeared as a bright line in the Radarsat S7 image (area Z in Figure 4-9, D) showed in the fused image as a green line (area Z in Figure 4-9, F). The row of trees appeared in green because this information only showed in the Radarsat S7 image (in green channel of the fused image).

Another important category in my study is water body and flooded areas. To get truly flooded areas from the water body and flooded area class, areas in this class were subtracted by water body polygons from the land cover layer. Next, the truly flooded areas and the dead vegetation areas were combined and total damaged areas were obtained. To assess damage of the 2002 flood, the total damaged areas were overlaid with the land cover layer. Finally, damaged areas of each land cover category were derived, as shown in Figure 4-10. The 2002 flood mainly inundated paddy field (73.31 sq.km.) and horticulture (23.99 sq.km.), which were 63% and 20% of the flooded areas, respectively. Although 7% and 8% of flooded areas were forested and non-forested wetland, these areas were not considered damaged because they were seasonally flooded. A total flooded area of other land cover categories (orchard, grass land, riverine tree, and built up area) was 1.80 sq.km. (2% of the flooded areas).

Comparison of Flood Maps from Fused Image and Best Radarsat Image

Because the Radarsat S7 image was considered the best Radarsat image in my study, the flood map interpreted from the Radarsat S7 was compared to that interpreted from the fused image according to objective 3 of my study.

However, flooding condition on October 15, 2002 when Radarsat acquired data in S7 mode was different from the condition on October 25, 2002 when Landsat acquired data in that the water surface elevation when the Landsat data were taken was lower than that when the Radarsat S7 data were taken. Accordingly, some flooded areas in the Radarsat S7 image (area X in Figure 4-11, A) appear as dry areas in the Landsat image (area X in Figure 4-11, B), and also in the fused image (area X in Figure 4-11, C). These dry areas were dead vegetation. The classification of the Radarsat S7 and fused images also showed that some parts of Radarsat S7 flooded areas were dead vegetation in the fused image (area X in Figure 4-11, D and E). Thus, before flooded areas interpreted from the Radarsat S7 image were compared to those interpreted from the fused image, the Radarsat S7 flooded areas were needed to be reduced by the dead vegetation areas. A purpose of this reduction was to eliminate influence of difference in water surface elevation on October 15 and 25, 2002. Figure 4-12 shows overlaid flooded areas of the reduced flood map of Radarsat S7 and the flood map from the fused image.

The two flood maps were compared referencing my visual interpretation of the IRS, Landsat, and Radarsat S7 images. In the reduced flood map of Radarsat S7, 250 sample points were randomly placed in areas classified as wet, and other 250 sample points were randomly placed in areas classified as dry. Locations of these 500 sample points were projected on overlaid IRS, Landsat, and Radarsat S7 images, and visual interpretation was used to design if the sample points fell in wet or dry areas. Then, an error matrix, classification accuracies and Kappa

statistics were calculated. This classification accuracy assessment method was also applied to the fused image.

For the flood map interpreted from Radarsat S7 image, overall classification accuracy was 95.40%. Because the primary purpose of my study was to map flooded area, wet category was in focus. Producer's accuracy of the wet category was 98.30% meaning that 98.30% of flooded areas were correctly identified as wet areas. User's accuracy of the wet category was 92.40%, which meant that 92.40% of pixels classified as wet were really wet areas (Table 4-9 and 4-10). Kappa value of the wet class was 0.8566 (Table 4-11) meaning classification of flooded areas was 85.66% better than randomly assigned pixels as flooded pixels. The overall Kappa statistic was 0.9080 (this classification was 90.80% better than a random classification).

For the flood map interpreted from the fused image, overall classification accuracy was 96.60%. For the wet category, producer's accuracy was 99.16%, and user's accuracy was 94.00%, which meant that 99.16% of wet areas were correctly identified, and 94.00% of pixels classified as wet were truly wet (Table 4-12 and 4-13). Kappa value of the wet class was 0.8859 (Table 4-14), which meant that classification of flooded areas was 88.59% better than a random classification of flooded areas. The overall Kappa statistic was 0.9320 (this classification was 93.20% better than a random classification).

Comparing between two flood maps derived from the Radarsat S7 and fused images, overall classification accuracy, producer's accuracy of the wet class, and user's accuracy of the wet class of that interpreted from the fused image were slightly higher than that interpreted from the Radarsat S7. Moreover, the overall Kappa value and the Kappa value of the wet class also confirmed that the classification of the fused image was better. Therefore, classification accuracy

of flooded areas derived from the fused image was higher than that derived from the Radarsat S7 alone and object 3 of my study was completed.

Underwater Feature Detection

To detect underwater features in the fused image, non-flooded areas were masked out and only areas classified as water body and flooded areas were inspected and compared to the land cover layer. In the land cover layer and the fused image (Figure 4-13, A and B), flooded areas including paddy field, horticulture, forested wetland and non-forested wetland appears in three major colors, black, green and orange. The black areas were completely flooded zones because these areas appeared dark in PC4 (red), Radarsat S7 (green) and PC1 (blue). The green areas were high moisture content vegetations or dikes surrounding paddy fields that had high backscatter. These objects appeared only in the Radarsat S7 image (Figure 4-13, D) that was displayed through green channel in the fused image. The orange tone areas were wet areas (wet vegetation and wet soil) appearing in both Radarsat S7 image (in green channel) and PC4 image (in red channel).

For the completely flooded areas, which appeared black in the fused image, it provided only flood boundary data, but did not provide information about underwater features. For green areas, which were high moisture vegetations or dikes surrounding paddy fields, they were not submerged features. Therefore, they did not provide information of underwater features. However, pattern of green lines (dikes) showed that the flooded areas were paddy fields (area X in Figure 4-13, B). Wet vegetation and wet soil appeared orange in the fused image (Figure 4-13, B). When the fused image was compared to the land cover data (Figure 4-13, A), the orange areas could be flooded paddy field, horticulture, forested wetland or non-forested wetland. They did not exclusively relate to any land cover category. A relationship between land cover types

and the three colors (black, green and orange) in flooded areas of the fused image could not be found. Therefore, underwater features could not be detected using the fused image.

At first, data of Landsat blue band (Figure 4-13, C) was expected to yield underwater information. Also, the Radarsat data (Figure 4-13, D) was supposed to show change in water surface roughness caused by different kinds of underwater features. However, the expected information did not show in the Landsat blue band, Radarsat and fused images. Therefore, we cannot detect underwater features from the fused image, and objective 4 of my study was completed.

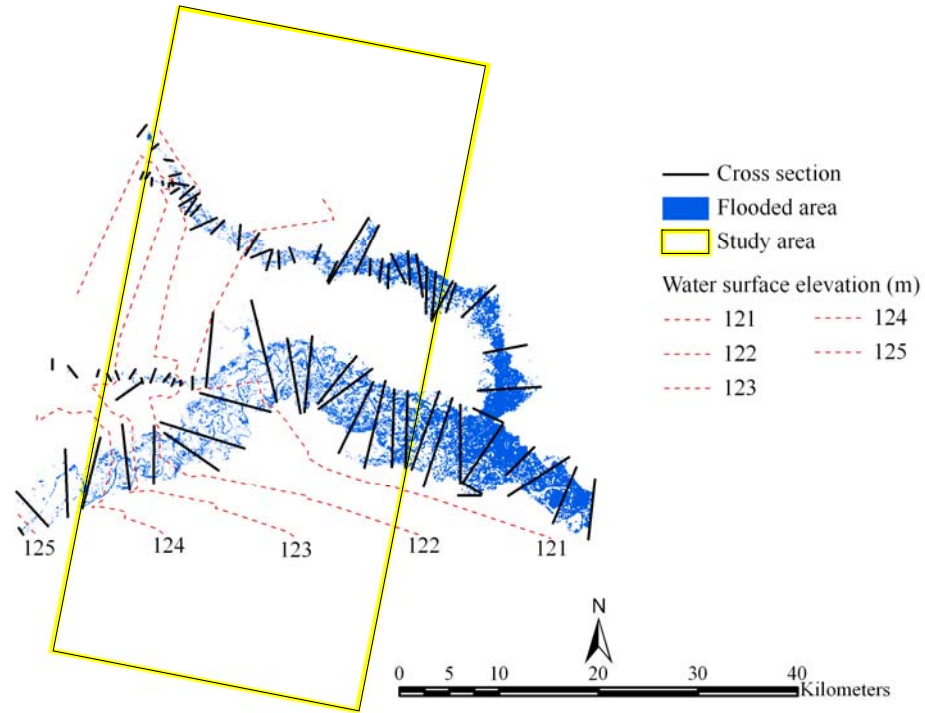


Figure 4-1. Flooded areas and water surface elevation simulated by HEC-RAS.

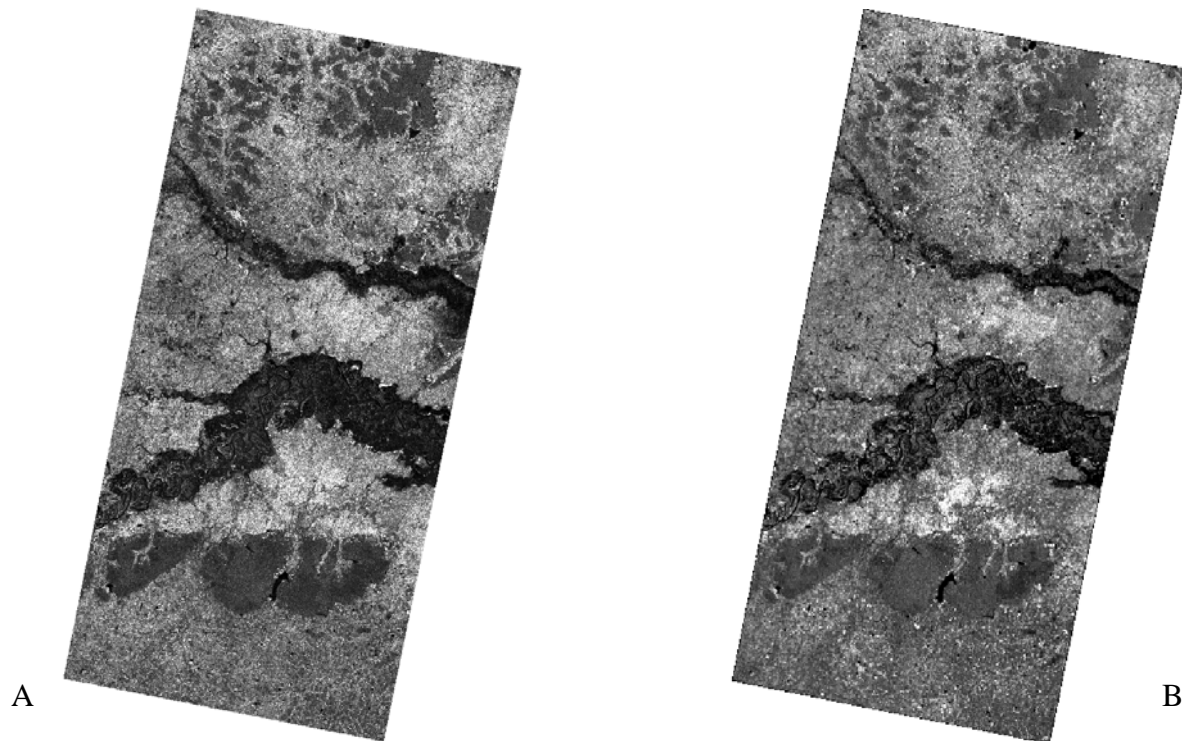


Figure 4-2. Radarsat images. A) Radarsat W1 acquired on October 11, 2002 at 25° incidence angle. B) Radarsat S7 acquired on October 15, 2002 at 47° incidence angle.

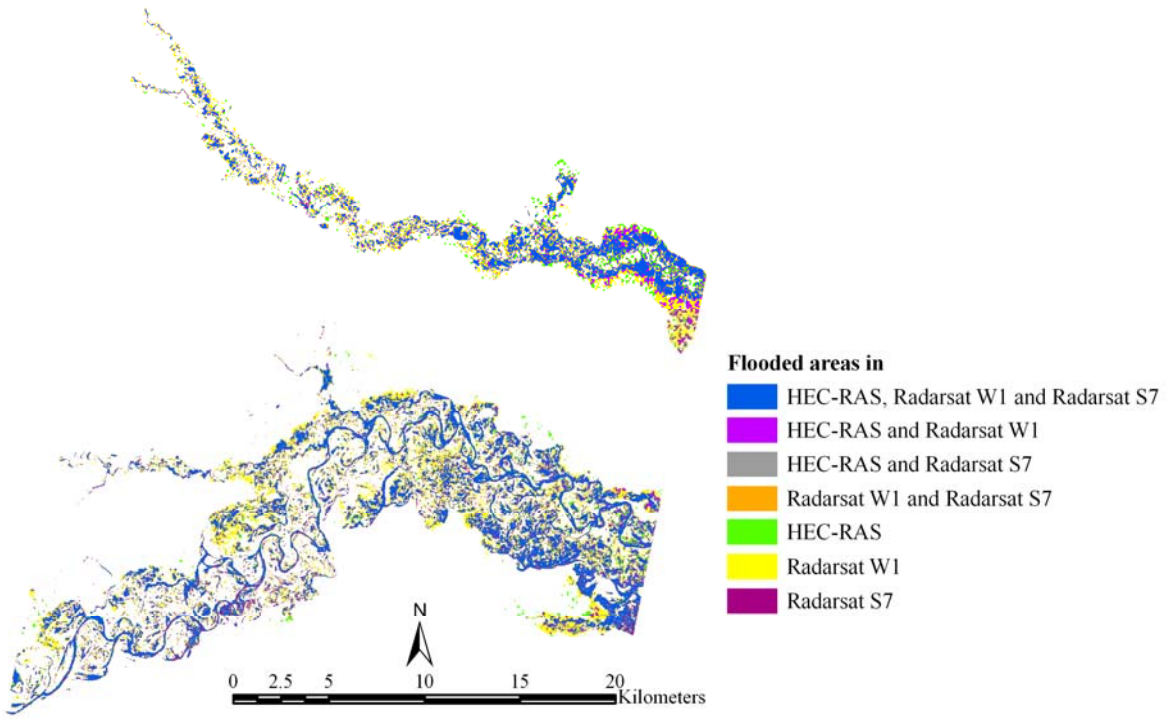


Figure 4-3. Overlaid flooded areas from HEC-RAS, Radarsat W1 and Radarsat S7 images.

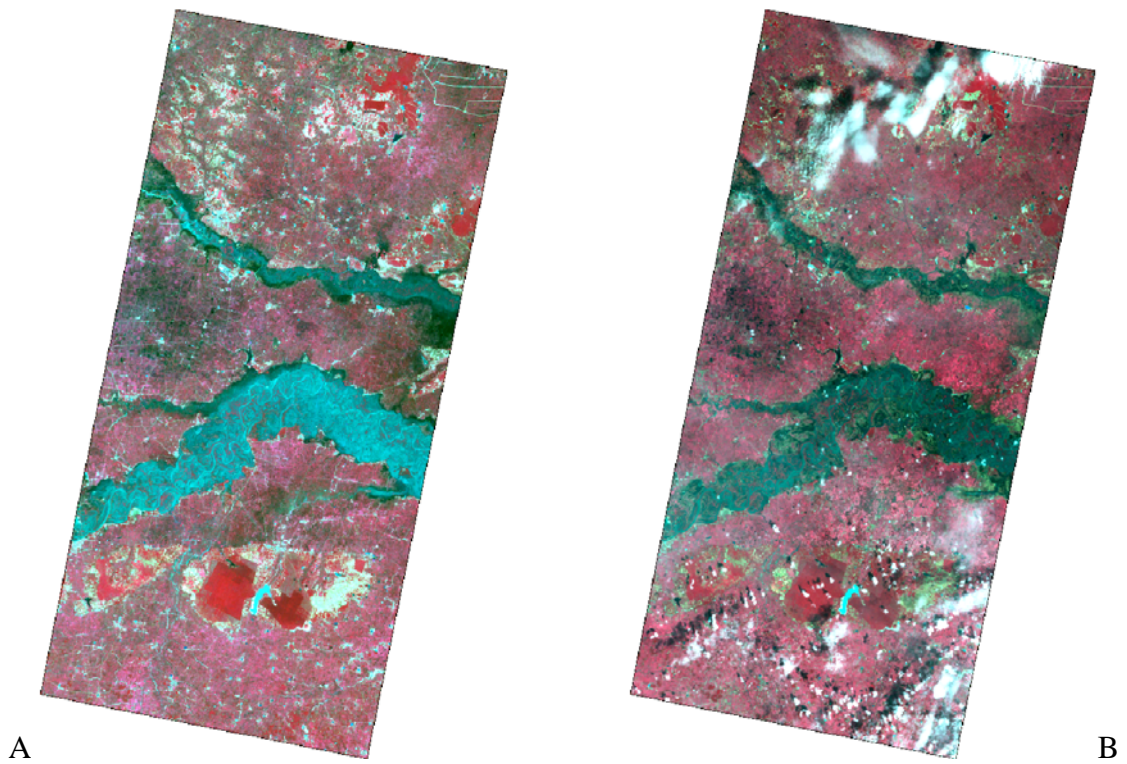


Figure 4-4. Inputs of PCA. A) IRS multispectral acquired on October 14, 2002. B) Landsat acquired on October 25, 2002.

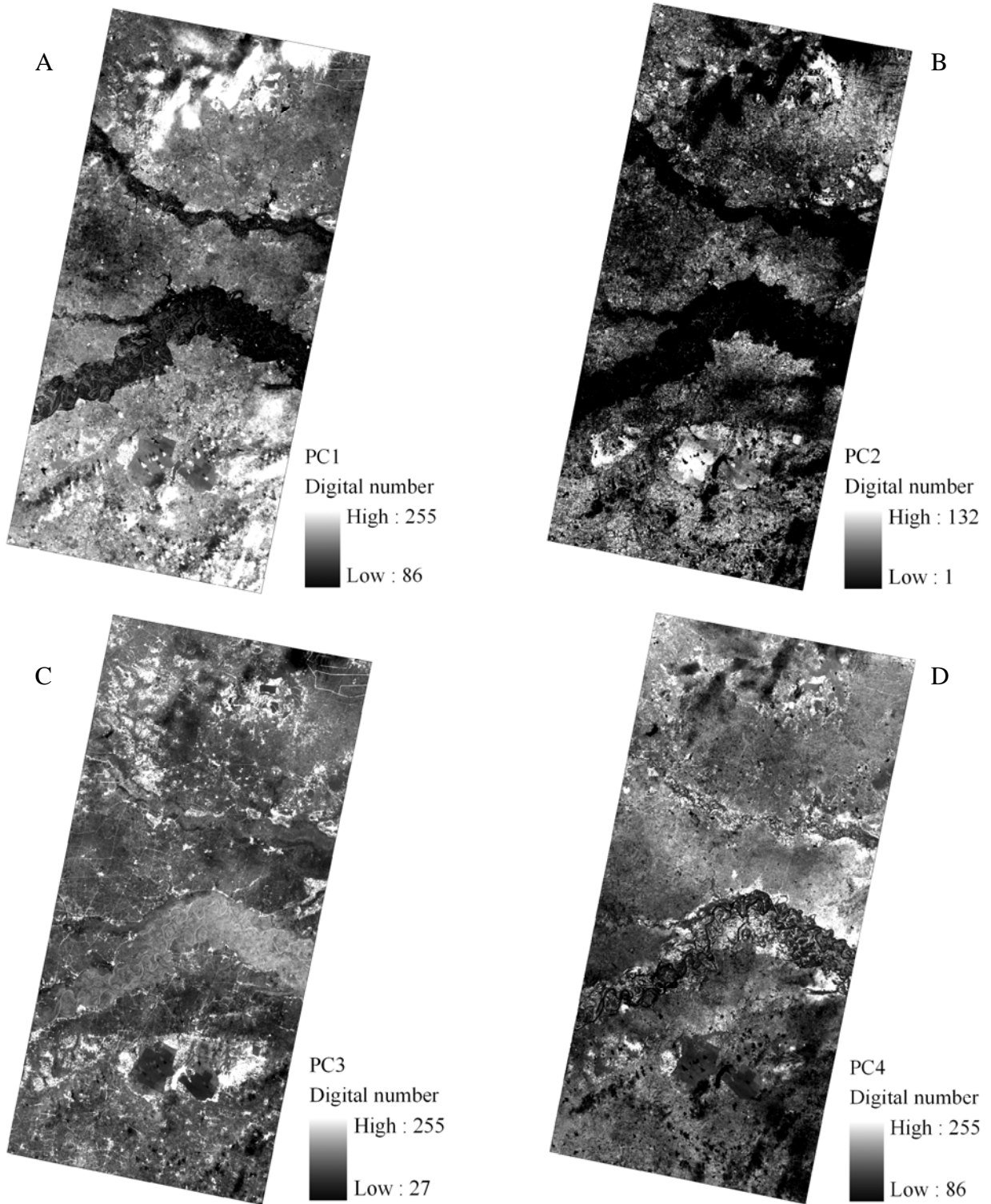


Figure 4-5. Principal component images and percentages of the total scene variance. A) PC1 contained 63.53%. B) PC2 contained 21.32%. C) PC3 contained 6.22%. C) PC4 contained 4.91%.

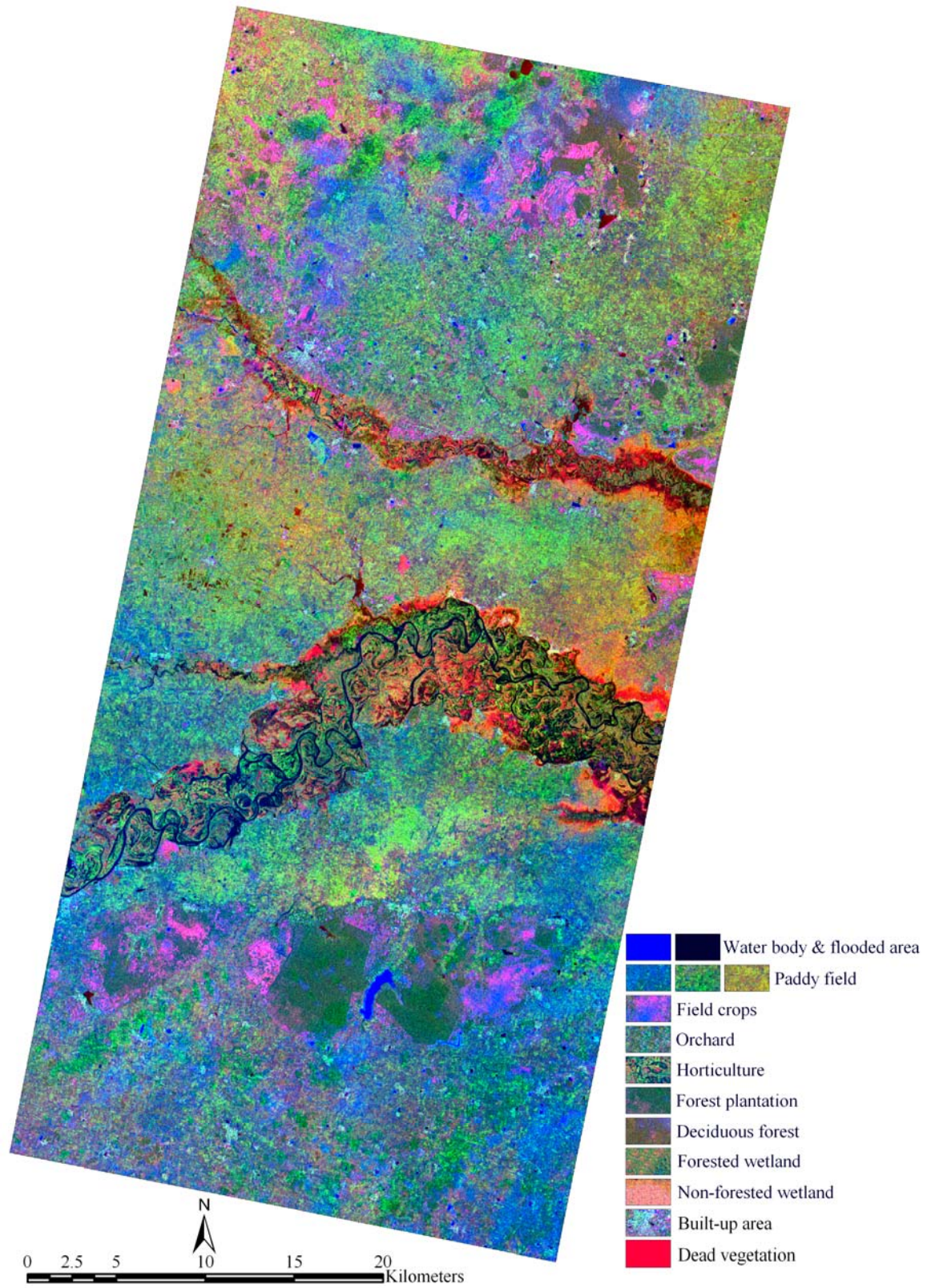


Figure 4-6. Fused image of PC4 (red), Radarsat S7 (green), and PC1 (blue) images.

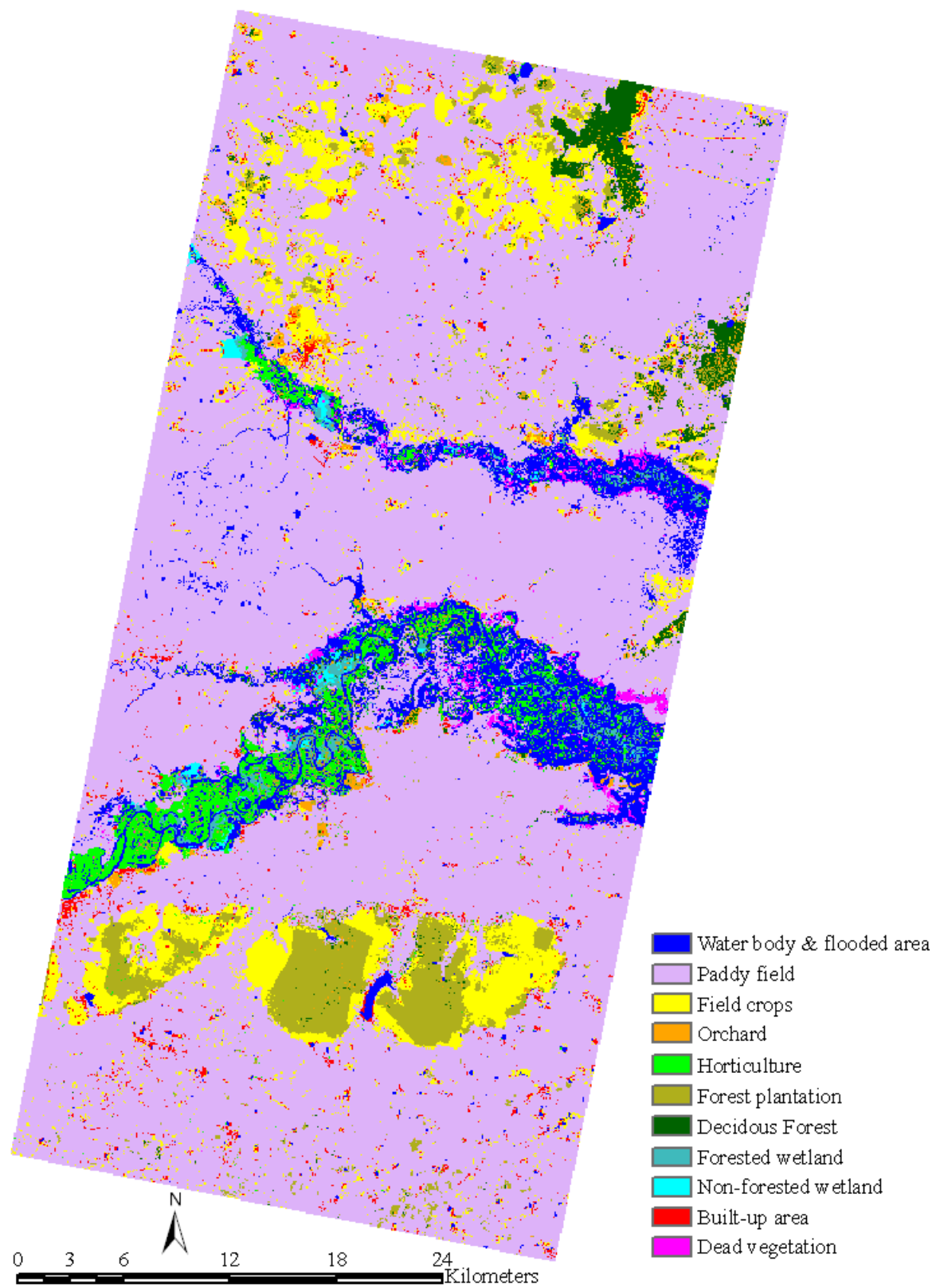


Figure 4-7. Fused image classification.

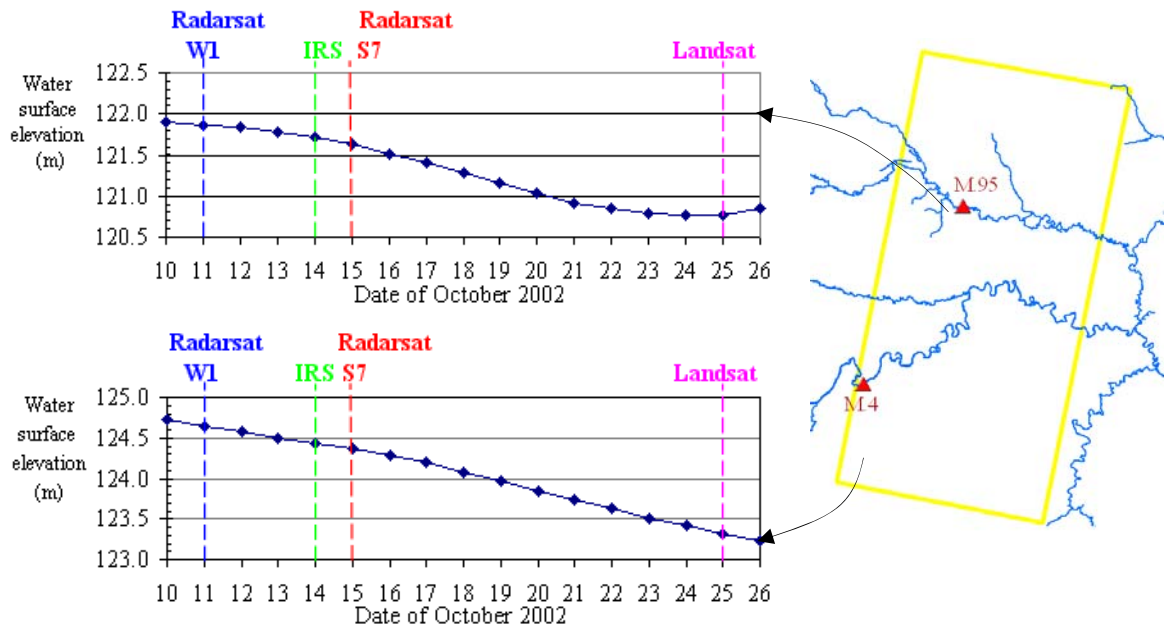


Figure 4-8. Water surface elevation measured from hydrological stations during October 11-25, 2002, dates of data acquisition.

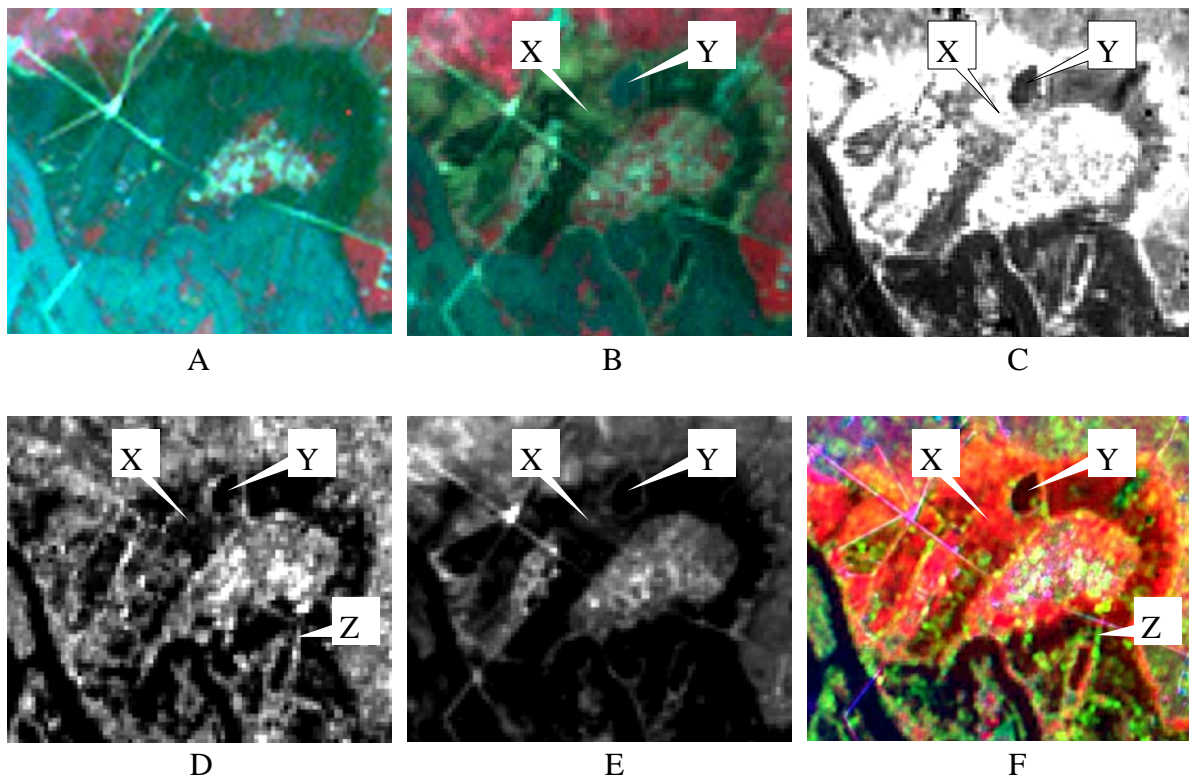


Figure 4-9. Dead vegetation (area X), built up water body (area Y), and a row of trees (area Z). A) IRS image. B) Landsat image. C) PC4 image. D) Radarsat S7 image. E) PC1 image. F) Fused image (PC4 in red, Radarsat S7 in green, and PC1 in blue).

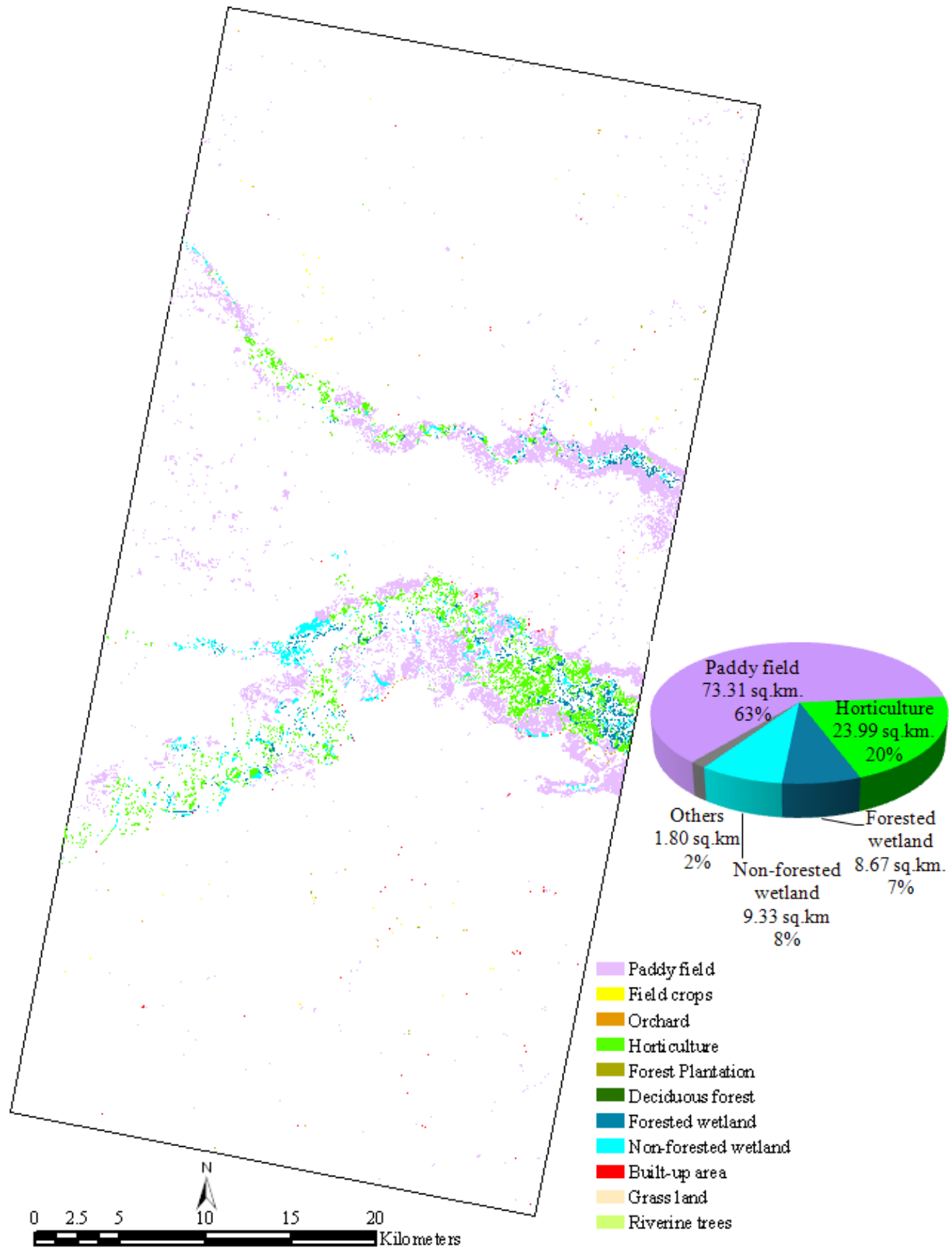


Figure 4-10. Flooded areas of each land cover type.

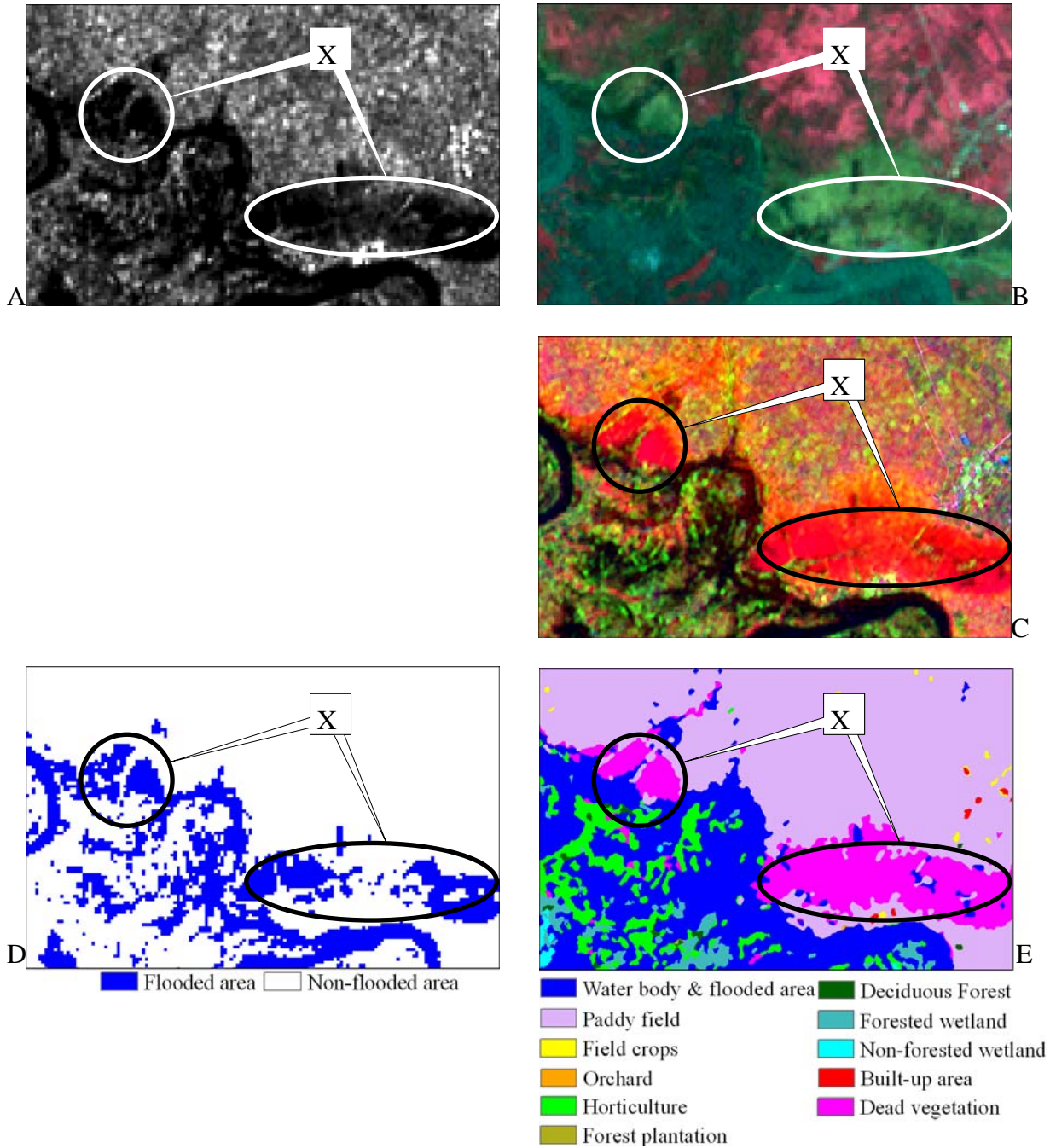


Figure 4-11. Differences caused by changing in water surface elevation. A) Larger flooded areas in Radarsat S7 image. B) Smaller flooded areas and exposed dead vegetation in Landsat image. C) Flooded areas (in black) and dead vegetation (in red) in fused image. D) Flooded areas classified from Radarsat S7 image. E) Classification of fused image.

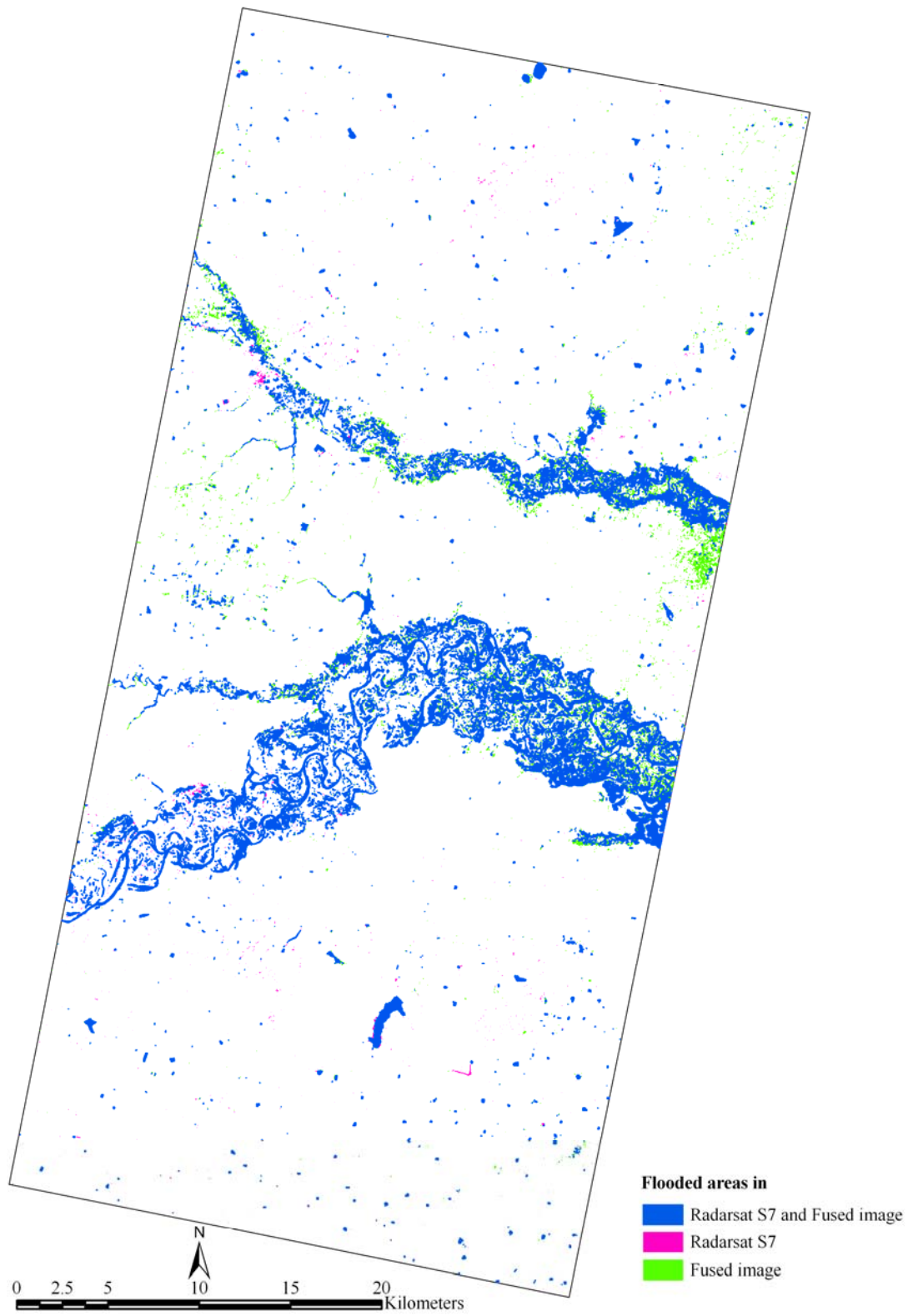


Figure 4-12. Overlaid flooded areas from the reduced flood map of Radarsat S7 and the fused image flood map.

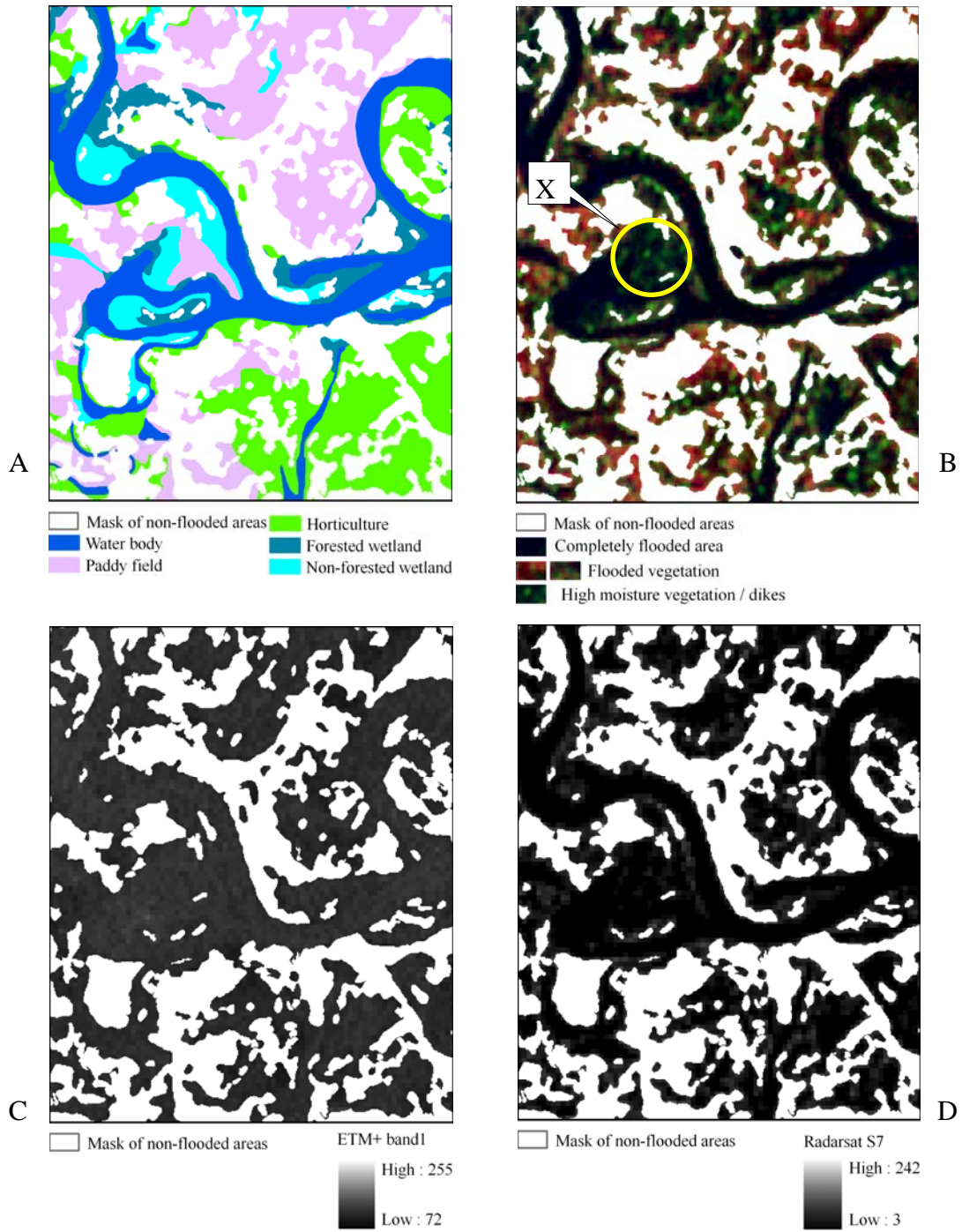


Figure 4-13. Inspection of underwater features. A) Land cover layer. B) Fused image. C) Blue band image of Landsat ETM+. D) Radarsat S7.

Table 4-1. Error matrix of classification of Radarsat W1 image

Classified Data	Wet	Dry	Row Total
Wet	197	53	250
Dry	9	241	250
Column Total	206	294	500

Table 4-2. Accuracy totals of classification of Radarsat W1 image

Class name	Reference totals	Classified totals	Number corrected	Producer's accuracy (%)	User's accuracy (%)
Wet	206	250	197	95.63	78.80
Dry	294	250	241	81.97	96.40
Totals	500	500	438	-	-

Overall Classification Accuracy = 87.60%

Table 4-3. Kappa statistics of classification of Radarsat W1 image

Class name	Kappa
Wet	0.6395
Dry	0.9126

Overall Kappa Statistics = 0.7520

Table 4-4. Error matrix of classification of Radarsat S7 image

Classified Data	Wet	Dry	Row Total
Wet	227	23	250
Dry	7	243	250
Column Total	234	266	500

Table 4-5. Accuracy totals of classification of Radarsat S7 image

Class name	Reference totals	Classified totals	Number corrected	Producer's accuracy (%)	User's accuracy (%)
Wet	234	250	227	97.01	90.80
Dry	266	250	243	91.35	97.20
Totals	500	500	470	-	-

Overall Classification Accuracy = 94.00%

Table 4-6. Kappa statistics of classification of Radarsat S7 image

Class name	Kappa
Wet	0.8271
Dry	0.9402

Overall Kappa Statistics = 0.8800

Table 4-7. Eigen values and eigen vectors.

PC	Eigen value	Eigen vector											
		ETM+1	ETM+2	ETM+3	ETM+4	ETM+5	ETM+6	ETM+7	ETM+8	IRS2	IRS3	IRS4	IRS5
PC1	1914.87	0.30012	0.31707	0.35545	0.32802	0.47208	-0.04567	0.32914	0.28538	0.03955	0.03913	0.38836	-0.08247
PC2	642.52	-0.34110	-0.27820	-0.39885	0.24251	0.05198	0.05308	-0.13202	0.01483	-0.06612	-0.11552	0.73369	0.09575
PC3	187.59	-0.14832	-0.11258	0.10416	-0.34432	0.13347	0.12218	0.15520	-0.18420	0.50815	0.63452	0.18908	0.22040
PC4	147.98	-0.26336	-0.21986	-0.17080	0.11979	0.59482	0.19343	0.32655	-0.02851	-0.19037	-0.10341	-0.41403	0.34893
PC5	46.92	-0.10471	0.20230	-0.01916	0.54643	-0.20329	0.20902	-0.32874	0.37189	0.29223	0.20289	-0.22133	0.37711
PC6	46.78	0.23642	0.15828	0.21148	-0.27097	-0.22402	0.36298	0.06901	-0.08033	-0.21243	-0.28664	0.22842	0.65444
PC7	8.01	0.17105	0.18653	-0.00237	0.36894	0.15679	0.01533	-0.20160	-0.82342	0.20218	-0.12084	-0.00928	0.02792
PC8	6.20	0.31925	-0.13931	-0.19203	0.30003	-0.27351	0.02122	0.27901	-0.15505	-0.49857	0.56978	0.00312	0.03742
PC9	5.77	-0.45093	-0.00620	0.62090	0.04592	0.09109	-0.01397	-0.35157	-0.11967	-0.46161	0.21753	0.03990	-0.02440
PC10	4.58	0.46972	-0.09819	-0.20716	-0.23751	0.44399	0.03778	-0.62301	0.14491	-0.15136	0.18732	0.00473	0.06843
PC11	2.70	-0.28320	0.79448	-0.40515	-0.20979	0.08052	-0.01388	0.02124	-0.03827	-0.20891	0.16379	0.02861	-0.02351
PC12	0.21	0.00049	-0.00062	0.00006	0.00020	-0.00030	-0.87453	0.00039	0.00008	0.00008	-0.00003	0.00002	0.08497

Table 4-8. Percentage of total scene variance

Principal component image	Percentage of total scene variance
PC1	63.53
PC2	21.32
PC3	6.22
PC4	4.91
PC5	1.56
PC6	1.55
PC7	0.27
PC8	0.21
PC9	0.19
PC10	0.15
PC11	0.09
PC12	0.01

Table 4-9. Error matrix of flood map interpreted from Radarsat S7 image

Classified Data	Wet	Dry	Row Total
Wet	231	19	250
Dry	4	246	250
Column Total	235	265	500

Table 4-10. Accuracy totals of flood map interpreted from Radarsat S7 image

Class name	Reference totals	Classified totals	Number corrected	Producer's accuracy (%)	User's accuracy (%)
Wet	235	250	231	98.30	92.40
Dry	265	250	246	92.83	98.40
Totals	500	500	477	-	-

Overall Classification Accuracy = 95.40%

Table 4-11. Kappa statistics of flood map interpreted from Radarsat S7 image

Class name	Kappa
Wet	0.8566
Dry	0.9660

Overall Kappa Statistics = 0.9080

Table 4-12. Error matrix of flood map interpreted from fused image

Classified Data	Wet	Dry	Row Total
Wet	235	15	250
Dry	2	248	250
Column Total	237	263	500

Table 4-13. Accuracy totals of flood map interpreted from fused image

Class name	Reference totals	Classified totals	Number corrected	Producer's accuracy (%)	User's accuracy (%)
Wet	237	250	235	99.16	94.00
Dry	263	250	248	94.30	99.20
Totals	500	500	483	-	-

Overall Classification Accuracy = 96.60%

Table 4-14. Kappa statistics of flood map interpreted from fused image

Class name	Kappa
Wet	0.8859
Dry	0.9831

Overall Kappa Statistics = 0.9320

CHAPTER 5 DISCUSSION

Discussion chapter is divided into three parts. The first part is flood prediction using HEC-RAS, which explains limitations of my study due to lack of input data, and using remotely sensed data to properly adjust geometry data of HEC-RAS. The second part is Radarsat W1 versus Radarsat S7 discussing influence of incidence angle and spatial resolution of the Radarsat images on classification accuracy. The last part of this chapter is the fused image discussion about its information and limitation.

Flood Prediction Using HEC-RAS

An important data requirement of HEC-GeoRAS is a high resolution DEM because ground cross section data are mainly extracted from the DEM, and the DEM is also used to overlay with a water surface TIN (simulated by HEC-RAS) to produce a flood map. In my study, a 30 m DEM with elevation values to the whole meter was used. However, spatial pattern of flooded areas in the HEC-RAS result was still similar to the pattern of flooded areas in the Radarsat images because the DEM was good enough to represent topography of the study area, a rural area with flat topography (slope < 0.5%). If the same DEM was to be used to predict flood in an urban area, the result likely would be unacceptable because the DEM, at this resolution, does not well represent roads, buildings, or other objects obstructing the flow.

Other inputs of HEC-RAS are hydrological data. The model requires at least one discharge for a reach, but in my study area, some reaches did not have discharge data. These missing data were estimated from addition of upstream discharges, and the estimated input discharges affected the output of HEC-RAS. Furthermore, hydrological stations in my study area are too far apart. As a result, spatial variation of hydrological data may not be measured well. Due to these

limitations, HEC-RAS might not yield its best output in my study. However, flooded areas simulated by HEC-RAS still had spatial patterns similar to those of the Radarsat images.

HEC-RAS delineates inundated areas only within coverage of cross sections. At a location, a cross section should long enough to cover the entire floodplain. If cross sections are too short, predicted flooded areas may be narrower than what they should be. On the other hand, if cross sections are too long, the number of elevation points of a cross section may exceed 500 and/or number of Manning's n values may exceed 20, and then data modification (such as applying cross section point filter to the data, and grouping land cover class of a smaller area into a bigger area) is required. If cross section lines are too long, this will lead to a larger area of interest and longer calculation time. Also, false flooded areas may appear as many small polygons due to depressions or sinks in DEM data. In my study, satellite imagery was used as a background in cross section length adjustment. Therefore, length of cross section lines could be properly adjusted to cover the flooded areas, and remotely sensed data could facilitate users in defining boundary of HEC-RAS calculation.

Radarsat W1 versus Radarsat S7

It has been shown that a Radarsat image taken at large incidence angle (more than 40°) is useful for land and water differentiation. For flooded forests, a small incidence angle (20° to 31°) of Radarsat signal could penetrate canopies of willow, grasses or sedges, and detect standing water under the vegetation. However, it has also been shown that increasing incidence angle of Radarsat signal did not substantially decrease distinction between flooded and non-flooded forest.

According to my study, the Radarsat S7 image (47° incidence angle and 25 m pixel size) was found to give higher classification accuracy of flooded and non-flooded areas than the Radarsat W1 image (25° incidence angle and 30 m pixel size). This may have resulted from two

factors: (1) an advantage of the Radarsat S7 image that it has higher spatial resolution than the Radarsat W1 image (25 m versus 30 m) and (2) an influence of land cover types in the flooded zones. In my study area, 63% of flooded areas was paddy field, 20% was horticulture, 8% was non-forested wetland, 7% was forested wetland, and 2% was other land cover types (orchard, grass land, riverine tree, and built up area). If the major land cover type in flooded areas is forest, the Radarsat S7 image taken at a large incidence angle may give lower classification accuracy, and the Radarsat W1 taken at a small incidence angle may give higher classification accuracy.

Although classification accuracy derived from the Radarsat W1 image was lower than that from the Radarsat S7 image, the Radarsat W1 data were still valuable for flood monitoring. In a study of flooding, high temporal resolution data are important. Therefore, various incidence angles and/or various spatial resolutions of radar images may unavoidable because a radar satellite has to take images at different incidence angles in order to obtain data of the same study site as frequently as possible.

The Fused Image

The primary purpose of the fused image was to include all necessary information about flooding into one image, and a more obvious flood boundary (compared to a Radarsat image alone) was expected. When considering only a pan-sharpened image of the Radarsat S7 (one of three bands in the fused image), the sharpened image yielded more distinct flood boundaries (area X in Figure 5.1, A) compared to the original 25 m Radarsat S7 image (area X in Figure 5.1, B). Furthermore, the sharpened image showed a more obvious bridge across the river and clearer floodwater over the ends of the bridge (area X in Figure 5.1, A and B). Boundary of a man-made pond was more apparent in the sharpened image (area Y in Figure 5.1, A and B). Roads and a man-made channel could be seen from the sharpened image, while these features could not be identified in the original Radarsat S7 image (area Z in Figure 5.1, A and B).

Classification accuracies and kappa statistics also confirmed that the classification accuracy of flooded areas derived from the fused image of IRS-1D, Landsat-7 and Radarsat-1 was higher than that derived from Radarsat-1 alone. In classification accuracy assessment of the fused image and the Radarsat S7 image, my visual interpretation of the IRS, Landsat and Radarsat S7 images and flood movement knowledge were used as the reference. Overall classification accuracy of the fused image (96.60%) was slightly higher than that of the Radarsat S7 (95.40%). For the flooded area category, producer's accuracy of the fused image was 99.16% while that of the Radarsat S7 was 98.30% (0.86% difference). User's accuracy of the fused image and the Radarsat S7 image were 94.00% and 92.40%, respectively (1.60% difference). Kappa value of the flooded area category derived from the fused image was 0.8859 while that obtained from the Radarsat S7 image was 0.8566 (0.0293 difference). Therefore, if the flood boundary is the only point of interest, use of the Radarsat image alone is a fast and convenient way to produce the result. However, from point of view of decision makers, more information relating to the flood situation is required, and the fused image from my study, for instance, is not only to provide a slightly better flood boundary, but also give information about damaged areas that were classified as dead vegetation in my study. The IRS panchromatic image (a component of the fused image) also provided information of flooded transportation routes (for example, a flooded bridge showed in area X of Figure 5.1, A).

Although the fused image contains various information of flooding, some other land cover information were neglected because second and third principal components (containing 21.32% and 6.22% of scene variance respectively) of IRS and Landsat data were left out during the fusion process. As a result, some land cover types could not be identified in the fused image. Comparing to land cover layer, grass land and riverine trees were two land cover categories that

were not identified in the fused image. Information that can be used to differentiate these two land cover classes may appear in the omitted principal component images. Thus, the fused image is suitable for a flood study, but is not appropriate for a land cover classification.

In my study, underwater features were not illustrated in the fused image. This may be because flood water was too turbid for the blue band of Landsat to penetrate and detect underwater features. Besides, flooded areas were mainly agricultural land (paddy field and horticulture). This vegetation is not a large object as are coral reefs or sand bars, which cause breaking waves or changes in water surface roughness, which could be detected by radar signal. Moreover, the study area is not a windy area and water surface appeared smooth in the Radarsat image. Information of underwater features did not show in the Radarsat image. Therefore, underwater features in my study area could not be detected using the fused image of IRS-1D, Landsat-7 and Radarsat-1.

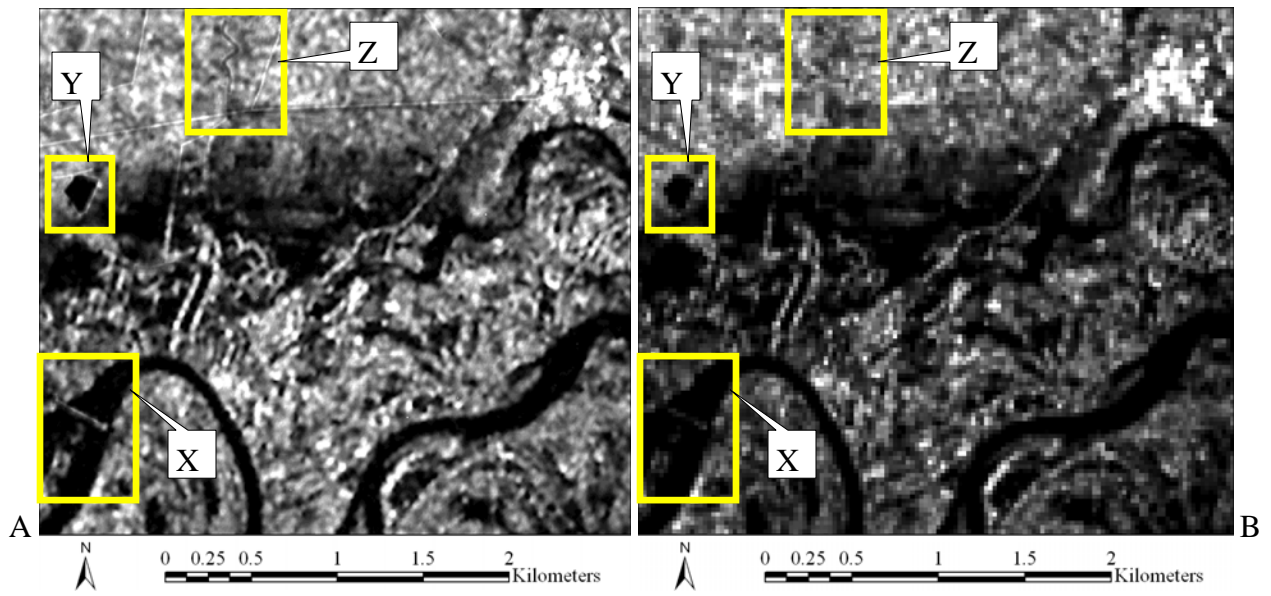


Figure 5-1. Radarsat S7 images. A) Pan-sharpened image. B) Original 25 m image.

CHAPTER 6 CONCLUSIONS

It is important to accurately delineate flooded areas because these data can be used as inputs for flood compensation calculation. Optical remote sensing data, such as Landsat and IRS, have been used to delineate flood, but optical sensor data are limited because flooded areas usually have extensive cloud cover, especially at the time of the flood. Radar data are suitable for flood delineation due to cloud penetration ability. However, it has been shown that radar data are not useful to detect flood in urban areas. Therefore, in my study, optical sensor data of Landsat and IRS were fused with radar data (Radarsat) to create a fused image, and flooded areas of the 2002 flood in the Mun River Basin were successfully delineated.

Flooded and non-flooded areas illustrating the 2002 inundation in the Mun River Basin were interpreted from two Radarsat images: Radarsat W1 (25° incidence angle, 30 m pixel size) acquired on October 11, 2002 and Radarsat S7 (47° incidence angle, 25 m pixel size) acquired on October 15, 2002. Classification accuracy of these Radarsat images was validated against the HEC-RAS flood map, for which required input data included hydrological data (average water surface elevation and average discharge of October 11 and 15, 2002) and topographic data of the study area. The Radarsat S7 yielded higher classification accuracy than the Radarsat W1 (overall Kappa value 88.0% versus 75.2%). This has resulted from the higher spatial resolution of the Radarsat S7 image and land cover types in the flood zones, dominated by paddy field and horticulture. Therefore, the Radarsat S7 image was deemed the best Radarsat image for flood detection in my study, and was chosen to be an input for image fusion.

Another input of the image fusion was the IRS panchromatic image with five m spatial resolution, acquired on October 14, 2002. This image illustrated the road networks in the study area and how the flood situation affected transportation routes. Two other inputs of the image

fusion, derived from PCA of Landsat (acquired on October 25, 2002) and IRS multispectral (acquired on October 14, 2002) data, were (1) PC1 (the image that showed the most obvious flood boundary) and (2) PC4 (the image that showed details in the flooded areas). The color composite image of PC4 (red), Radarsat S7 (green) and PC1 (blue) was sharpened by the IRS panchromatic image to create the fused image containing information of the 2002 flood in the Mun River Basin.

The fused image was classified using unsupervised classification to obtain eleven land cover classes including water body and flooded area, paddy field, field crops, orchard, horticulture, forest plantation, deciduous forest, forested wetland, non-forested wetland, built-up area, and dead vegetation. The fused image contained a temporal factor due to different acquisition dates of the input data (twelve-day period during October 14 – 25, 2002). Exposed dead vegetation due to decreasing of water surface elevation during the twelve-day period was identified in the fused image.

The water body and flooded area class was used to create the flood map from the fused image, and was then compared to the flood map from the Radarsat S7 image (the best Radarsat image in my study). In the comparison, my visual interpretation based on the IRS, Landsat and Radarsat S7 images was used as the reference. It was found that classification accuracy of flooded and non-flooded areas derived from the fused image was slightly higher than that of the Radarsat S7 image alone (overall Kappa value 93.2% versus 90.8%). Therefore, if the flood boundary is the only point of interest, use of the Radarsat image alone is a fast and convenient way to produce the result. Nevertheless, the fused image provided a slightly better flood boundary, damaged area information (dead vegetation), and flooded transportation routes.

Although the fused image illustrated information relating to the flood, it did not show underwater features because flood water was too turbid for the blue band of Landsat to penetrate and detect underwater features. Also, submerged vegetation (flooded paddy field and horticulture) did not cause change in water surface roughness. Thus, Radarsat signal could not detect turbulent water caused by the submerged vegetation in the study area.

In my study, components of the fused image were selected based on a flood study. The same data set of Landsat, IRS and Radarsat can be used for other purposes, such as a road network study, for which the most useful information was shown in the PC3 image.

For future studies, fusion of optical sensor and radar data to detect flooding in a monsoonal zone will be continued because flood information is necessary for providing relief efforts. Flood boundary data is an important input for flood compensation calculation, and fusion of multispectral and radar data with higher spatial resolution panchromatic imagery will be needed. As more optical sensor satellites become available, the opportunities to gather data on flooded areas under clear atmospheric conditions during a rainy season increase. For Thailand, its first optical sensor satellite, Theos, was launched in October 2008. It provides 2 m spatial resolution panchromatic data and 15 m spatial resolution of multispectral data in blue, green, red and near infrared. With a steerable mirror like that of the SPOT satellite, Theos can acquire data of a location every three days. The high temporal resolution makes a flood movement study possible. These data can be fused with radar data acquired regardless of weather conditions. In addition, fusion of optical sensor data with various polarizations of radar data should be studied to determine information content of each polarized image for a flood study.

REFERENCES

- Ahmad, S., and S. P. Simonovic, 2001. Integration of heuristic knowledge with analytical tools for the selection of flood damage reduction measures, *Canadian Journal of Civil Engineering*, 28(2):208-221.
- Akar, I., C. Uysal, and D. Maktav, 2008. Determination of natural disaster by integration of remote sensing and GIS: the Yeniçiftlik stream basin model in Istanbul, Turkey, *Proceeding of the the XXIth ISPRS Congress*, Beijin, China.
- Bates, P. D., and A. P. J. De Roo, 2000. A simple raster-based model for flood inundation simulation, *Journal of Hydrology*, 236(1-2):54-77.
- Bates, P. D., M. D. Wilson, M. S. Horritt, D. C. Mason, N. Holden, and A. Currie, 2006. Reach scale floodplain inundation dynamics observed using airborne synthetic aperture radar imagery: Data analysis and modelling, *Journal of Hydrology*, 328(1-2):306-318.
- Benito, G., A. Diez-Herrero, and M. F. de Villalta, 2003. Magnitude and frequency of flooding in the Tagus Basin (central Spain) over the last millennium, *Climatic Change*, 58(1/2):171-192.
- Bhan, S. K., and Flood Team, 2001. Study of floods in West Bengal during September, 2000 using Indian Remote sensing satellite data, *Journal of the Indian Society of Remote Sensing*, 29(1-2):1-3.
- Biftu, G. F., and T. Y. Gan, 2001. Semi-distributed, physically based, hydrologic modeling of the Paddle River Basin, Alberta, using remotely sensed data, *Journal of Hydrology*, 244(3-4):137-156.
- Bjerklie, D. M., D. Moller, L. C. Smith, and S. L. Dingman, 2005. Estimating discharge in rivers using remotely sensed hydraulic information, *Journal of Hydrology*, 309(1-4):191-209.
- Blyth, K., 1993. The use of microwave remote sensing to improve spatial parameterization of hydrological models, *Journal of Hydrology*, 152(1-4):103-129.
- Boruah, S., D. Gilvear, P. Hunter, and N. Sharma, 2008. Quantifying channel planform and physical habitat dynamics on a large braided river using satellite data - the Brahmaputra, India, *River Research and Applications*, 24(5):650-660.
- Canadian Space Agency, 2006. Radarsat-1. URL: <http://www.asc-csa.gc.ca/eng/satellites/radarsat1/components.asp> (last date accessed: 26 November 2008)
- Chow, V. T., 1959. *Open-channel hydraulics*, McGraw-Hill, New York.
- Correia, F. N., F. C. Rego, M. D. G. Saraiva, and I. Ramos, 1998. Coupling GIS with hydrologic and hydraulic flood modeling, *Water Resources Management*, 12(3):229-249.

- Di Baldassarre, G., G. Schumann, and P. D. Bates, 2009. Near real time satellite imagery to support and verify timely flood modelling, *Hydrological Processes*, 23(5):799-803.
- Diniz, M. G. M., N. d. O. Nascimento, and M. B. Baptista, 2003. Risk assessment of flood control failure in a storm water drainage system incorporating multiple detention basins, *Proceeding of the Discharged urban waters : Ressource or Risk ? 2nd WWW-YES*, Vitry sur Seine, France.
- Dose, T., G. Morgenschweis, and T. Schlurmann, 2002. Extrapolating stage-discharge relationships by numerical modeling. (last date accessed: 7 May 2009)
- Dwivedi, R. S., and S. Kandrika, 2005. Delineation and monitoring of aquaculture areas using multi-temporal space- borne multispectral data, *Current Science*, 89(8):1414-1421.
- Dwivedi, R. S., K. V. Ramana, S. S. Thammappa, and A. N. Singh, 2001. The utility of IRS-1C LISS-III and Pan-merged data for mapping salt-affected soils, *Photogrammetric Engineering & Remote Sensing*, 67(10):1167-1175.
- Dwivedi, R. S., B. R. M. Rao, and S. Bhattacharya, 1999. Mapping wetlands of the Sundaban Delta and its environs using ERS-1 SAR data, *International Journal of Remote Sensing*, 20(11):2235-2247.
- El-Kadi, A. I., and E. Yamashita, 2007. Modeling stream flows and flood delineation of the 2004 flood disaster, Manoa, O'ahu, Hawai'i, *Pacific Science*, 61(2):235(21).
- Fox, N. I., and C. G. Collier, 2000. Estimating medium-range catchment flood potential, *Journal of Hydrology*, 237(1-2):1-16.
- Frazier, P. S., and K. J. Page, 2000. Water body detection and delineation with Landsat TM data, *Photogrammetric Engineering & Remote Sensing*, 66(12):1461-1467.
- Freeman, A., B. Chapman, and P. Siqueira, 2002. The JERS-1 Amazon Multi-season Mapping Study (JAMMS): Science objectives and implications for future missions, *International Journal of Remote Sensing*, 23(7):1447-1460.
- Gluch, R., 2002. Urban growth detection using texture analysis on merged Landsat TM and SPOT-P data, *Photogrammetric Engineering & Remote Sensing*, 68(12):1283-1288.
- Goshtasby, A. A., and S. Nikolov, 2007. Image fusion: Advances in the state of the art, *Information Fusion*, 8(2):114-118.
- Green, A. A., G. Whitehouse, and D. Outhet, 1983. Causes of flood streamlines observed on Landsat images and their use as indicators of floodways, *International Journal of Remote Sensing*, 4(1):5-16.
- Haack, B., and M. Bechdol, 2000. Integrating multisensor data and radar texture measures for land cover mapping, *Computers & Geosciences*, 26(4):411-421.

- Haestad Methods, 2007. Hydraulic models on the Mississippi River. URL:
<http://www.haestad.com/library/books/FMRAS/FloodplainOnlineBook/javascript/wwhelp/wwhimpl/java/html/wwhelp.htm?href=Floodplain%20with%20HEC-RAS-05-1.html> (last date accessed: 5 October 2007)
- Henderson, F. M., T. F. Hart, Jr., R. Chasan, and J. Portolese, 1998. Analysis of optical-SAR data fusion and merged data set procedures in highly developed urbanized coastal ecosystems, *Proceeding of the Geoscience and Remote Sensing Symposium Proceedings*, 1998. IGARSS '98. 1998 IEEE International.
- Henderson, F. M., and A. J. Lewis (editors), 1998. *Principles and Applications of Imaging Radar*, John Wiley & Sons, New York.
- Henry, J. B., P. Chastanet, K. Fellah, and Y. L. Desnos, 2006. Envisat multi-polarized ASAR data for flood mapping, *International Journal of Remote Sensing*, 27(10):1921-1929.
- Horritt, M. S., and P. D. Bates, 2002. Evaluation of 1D and 2D numerical models for predicting river flood inundation, *Journal of Hydrology*, 268(1-4):87-99.
- Horritt, M. S., D. C. Mason, and A. J. Luckman, 2001. Flood boundary delineation from synthetic aperture radar imagery using a statistical active contour model, *International Journal of Remote Sensing*, 22(13):2489-2507.
- Huang, H., J. Legarsky, and M. Othman, 2007. Land-cover classification using Radarsat and Landsat imagery for St. Louis, Missouri, *Photogrammetric Engineering & Remote Sensing*, 73(1):37-43.
- Hudson, P. F., and R. R. Colditz, 2003. Flood delineation in a large and complex alluvial valley, lower Pa'nuco Basin, Mexico, *Journal of Hydrology*, 280(1-4):229-245.
- Hurst, H. E., 1952. *The Nile: A General Account of the River and the Utilization of its Waters*, Constable, London.
- International Charter, 2008. Flooding in Namibia and Angola.
http://www.disasterscharter.org/disasters/CALLID_197_e.html (last date accessed: 5 May 2009)
- Islam, M. A., 2007. Flood hazard mapping of Dhaka-Narayanganj-Demra (DND) project using geo-informatics tools.
http://www.icharm.pwri.go.jp/html_j/docu/pdf/2008/4119_master_course2007/annex/11_3_aminul_synopsis.pdf (last date accessed: 7 May 2009)
- Kar, A., 1994. Lineament control on channel behaviour during the 1990 flood in the southeastern Thar Desert, *International Journal of Remote Sensing*, 15(13):2521-2530.
- Kermel-Torres, D. (editor), 2004. *Atlas of Thailand*, Silkworm Books, Chiang Mai, Thailand.

- Kiage, L. M., N. D. Walker, S. Balasubramanian, A. Babin, and J. Barras, 2005. Applications of Radarsat-1 synthetic aperture radar imagery to assess hurricane-related flooding of coastal Louisiana, *International Journal of Remote Sensing*, 26(24):5359-5380.
- Kidson, R., K. S. Richards, and P. A. Carling, 2005. Reconstructing the ca. 100-year flood in Northern Thailand, *Geomorphology*, 70(3-4):279-295.
- Knebl, M. R., Z. L. Yang, K. Hutchison, and D. R. Maidment, 2005. Regional scale flood modeling using NEXRAD rainfall, GIS, and HEC-HMS/RAS: A case study for the San Antonio River Basin summer 2002 storm event, *Journal of Environmental Management*, 75(4):325-336.
- Koutsias, N., M. Karteris, and E. Chuvico, 2000. The use of intensity-hue-saturation transformation of Landsat-5 thematic mapper data for burned land mapping, *Photogrammetric Engineering & Remote Sensing*, 66(7):829-839.
- Lang, M. W., P. A. Townsend, and E. S. Kasischke, 2008. Influence of incidence angle on detecting flooded forests using C-HH synthetic aperture radar data, *Remote Sensing of Environment*, 112(10): 3898-3907.
- Lillesand, T. M., R. W. Kiefer, and J. W. Chipman, 2007. *Remote Sensing and Image Interpretation*, 6th Ed, John Wiley & Sons, New York.
- Liu, Z., F. Huang, L. Li, and E. Wan, 2002. Dynamic monitoring and damage evaluation of flood in north-west Jilin with remote sensing, *International Journal of Remote Sensing*, 23(18):3669-3679.
- Lu, D., M. Batistella, and E. Moran, 2008. Integration of Landsat TM and SPOT HRG images for vegetation change detection in the Brazilian Amazon, *Photogrammetric Engineering & Remote Sensing*, 74(4):421-430.
- Mark, O., S. Weesakul, C. Apirumanekul, S. B. Aroonnet, and S. Djordjevic, 2004. Potential and limitations of 1D modelling of urban flooding, *Journal of Hydrology*, 299(3-4):284-299.
- Mosquera-Machado, S., and S. Ahmad, 2007. Flood hazard assessment of Atrato River in Colombia, *Water Resources Management*, 21(3):591-609.
- Mutlu, M., S. C. Popescu, C. Stripling, and T. Spencer, 2008. Mapping surface fuel models using lidar and multispectral data fusion for fire behavior, *Remote Sensing of Environment*, 112(1):274-285.
- National Economic and Social Advisory Council, 2007. Royal irrigation department prepares 1,000 irrigation projects. URL: <http://www2.nesac.go.th/document/show12.php?did=07070024> (last date accessed: 17 September 2007)

- National Emergency System of Uruguay, 2007. Flooding in Uruguay. URL: http://www.disasterscharter.org/disasters/CALLID_159_e.html (last date accessed: 29 September 2007)
- National Statistical Office, 2000. 1960-2000 Population and Housing Census, National Statistical Office, Bangkok.
- National Statistical Office, 2003. 2003 Agricultural Census: Northeastern Region, National Statistical Office, Bangkok.
- Netzband, M., G. Meinel, and R. Lippold, 1999. Classification of settlement structures using morphological and spectral features in fused high resolution satellite images (IRS-1C). URL: <http://www.data-fusion.org/ps/sig/meeting/Spain99ps/netzband.pdf> (last date accessed: 1 October 2007)
- Neuenschwander, A. L., M. M. Crawford, and S. Ringrose, 2005. Results from the EO-1 experiment - A comparative study of Earth Observing-1 Advanced Land Imager (ALI) and Landsat ETM+ data for land cover mapping in the Okavango Delta, Botswana, *International Journal of Remote Sensing*, 26(19):4321-4337.
- Nichol, J., and M. S. Wong, 2005. Satellite remote sensing for detailed landslide inventories using change detection and image fusion, *International Journal of Remote Sensing*, 26(9):1913-1926.
- Paz, A. R., and W. Collischonn, 2007. River reach length and slope estimates for large-scale hydrological models based on a relatively high-resolution digital elevation model, *Journal of Hydrology*, 343(3-4):127-139.
- Petchprayoon, P., 2001. The prediction of flash flood caused by dam failure: a case study at the Tha Dan dam, Thailand, *Proceeding of the 22nd Asian Conference on Remote Sensing*, Singapore.
- Pohl, C., and J. L. Van Genderen, 1998. Review article Multisensor image fusion in remote sensing: Concepts, methods and applications, *International Journal of Remote Sensing*, 19(5):823-854.
- Profeti, G., and H. Macintosh, 1997. Flood management through Landsat TM and ERS SAR data: a case study, *Hydrological Processes*, 11(10):1397-1408.
- Rosenqvist, A., and C. M. Birkett, 2002. Evaluation of JERS-1 SAR mosaics for hydrological applications in the Congo River Basin, *International Journal of Remote Sensing*, 23(7):1283-1302.
- Rosenqvist, A., B. R. Forsberg, T. Pimentel, Y. A. Rauste, and J. E. Richey, 2002. The use of spaceborne radar data to model inundation patterns and trace gas emissions in the central Amazon floodplain, *International Journal of Remote Sensing*, 23(7):1303-1328.

- Ryu, J. H., J. S. Won, and K. D. Min, 2002. Waterline extraction from Landsat TM data in a tidal flat: A case study in Gomso Bay, Korea, *Remote Sensing of Environment*, 83(3):442-456.
- Saindranath, J., P. V. N. Rao, and S. Thiruvengadachari, 2000. Radarsat data analysis for monitoring and evaluation of irrigation projects in the monsoon, *International Journal of Remote Sensing*, 21(17):3219-3226.
- Sakamoto, T., N. Van Nguyen, A. Kotera, H. Ohno, N. Ishitsuka, and M. Yokozawa, 2007. Detecting temporal changes in the extent of annual flooding within the Cambodia and the Vietnamese Mekong Delta from MODIS time-series imagery, *Remote Sensing of Environment*, 109(3):295-313.
- Sansena, T., and K. Bhaktikul, 2007. The application of hydraulic model with geographic information system to create flood risk mapping in Mae Klong river. http://kromchol.rid.go.th/ffd/papers/Paper%20Session%202/P2-06%20PaperThudchai_edit.pdf (last date accessed: 27 February 2009)
- Santos, C., and J. P. Messina, 2008. Multi-sensor data fusion for modeling African palm in the Ecuadorian Amazon, *Photogrammetric Engineering & Remote Sensing*, 74(6):711-723.
- Saraf, A. K., 1999. IRS-1C-LISS-III and PAN data fusion: An approach to improve remote sensing based mapping techniques, *International Journal of Remote Sensing*, 20(10):1929-1934.
- Saroglu, E., F. Bektas, N. Musaoglu, and C. Goksel, 2004. Fusion of multisensor remote sensing data: assessing the quality of resulting images, *Proceeding of the Geo-Imagery Bridging Continents*, Istanbul, Turkey.
- Schetselaar, E. M., 2001. On preserving spectral balance in image fusion and its advantages for geological image interpretation, *Photogrammetric Engineering & Remote Sensing*, 67(8):925-934.
- Schultz, G. A., 1988. Remote sensing in hydrology, *Journal of Hydrology*, 100(1-3):239-265.
- Schumann, G., P. Matgen, L. Hoffmann, R. Hostache, F. Pappenberger, and L. Pfister, 2007. Deriving distributed roughness values from satellite radar data for flood inundation modelling, *Journal of Hydrology*, 344(1-2):96-111.
- Sharma, K. D., M. Menenti, J. Huygen, and P. C. Fernandez, 1996. Distributed numerical rainfall-runoff modelling in an arid region using thematic mapper data and a geographical information system, *Hydrological Processes*, 10(9):1229-1242.
- Sharma, P. K., R. Chopra, V. K. Verma, and A. Thomas, 1996. Technical note flood management using remote sensing technology: The Punjab (India) experience, *International Journal of Remote Sensing*, 17(17):3511-3521.
- Siegel, H., and M. Gerth, 2000. Satellite-based studies of the 1997 Oder flood event in the Southern Baltic Sea, *Remote Sensing of Environment*, 73(2):207-217.

- Singhroy, V., 1995. SAR integrated techniques for geohazard assessment, *Advances in Space Research*, 15(11):67-78.
- Singhroy, V., K. E. Mattar, and A. L. Gray, 1998. Landslide characterisation in Canada using interferometric SAR and combined SAR and TM images, *Advances in Space Research*, 21(3):465-476.
- Song, Y. S., H. G. Sohn, and C. H. Park, 2007. Efficient water area classification using Radarsat-1 SAR Imagery in a high relief mountainous environment, *Photogrammetric Engineering & Remote Sensing*, 73(3):285-296.
- Souza Filho, P. W. M., W. R. Paradella, and O. F. M. d. Silveira, 2005. Synthetic aperture radar for recognition of coastal features in the wet tropics: applications in the Brazilian Amazon coast, *Bol. Mus. Para. Emílio Goeldi, sér. Ciências Naturais*, 1(1):201-207.
- Spruce, J. P., and R. McKellip, 2006. Assessing Hurricane Katrina damage to the Mississippi Gulf Coast using Ikonos imagery.
http://calval.cr.usgs.gov/JACIE_files/JACIE06/Files/212Spruc.pdf (last date accessed: 5 May 2009)
- Srivastava, Y. K., B. Doley, D. K. Pal, R. K. Das, S. Sudhakar, S. Adiga, K. V. Venkatachary, and S. K. Srivastava, 2000. High resolution remote sensing data & GIS techniques in updation of infrastructure details for flood damage assessment - a case study, *Proceeding of the 21st Asian Conference on Remote Sensing*, Taipei, Taiwan.
- Staples, G. C., J. Hurely, and R. S. Burnsand, 1998. Coastal zone monitoring with Radarsat-1, *Proceeding of the 19th Asian Conference on Remote Sensing*, Manila, Philippines.
- Taragsa, N., C. Mongkolsawat, C. Pawattana, and R. Suwanweerakamtorn, 2004. An application of GIS and hydraulic model to flood plain inundation, *Journal of Remote Sensing and GIS Association of Thailand*, 5(3):63-75.
- Townsend, P. A., 2001. Mapping seasonal flooding in forested wetlands using multi-temporal Radarsat SAR, *Photogrammetric Engineering & Remote Sensing*, 67(7):857-864.
- Townsend, P. A., and J. R. Foster, 2002. A synthetic aperture radar-based model to assess historical changes in lowland floodplain hydroperiod, *Water Resour. Res.*, 38.
- Townsend, P. A., and S. J. Walsh, 1998. Modeling floodplain inundation using an integrated GIS with radar and optical remote sensing, *Geomorphology*, 21(3-4):295-312.
- Toyra, J., and A. Pietroniro, 2005. Towards operational monitoring of a northern wetland using geomatics-based techniques, *Remote Sensing of Environment*, 97(2):174-191.
- Toyra, J., A. Pietroniro, and L. W. Martz, 2001. Multisensor hydrologic assessment of a freshwater wetland, *Remote Sensing of Environment*, 75(2):162-173.

- U.S. Army Corps of Engineers, 2005. *HEC-GeoRAS GIS tools for support of HEC-RAS using ArcGIS*, U.S. Army Corps of Engineers, Davis, CA.
- U.S. Army Corps of Engineers, 2007. HEC history. URL: <http://www.hec.usace.army.mil/whoweare/history.html> (last date accessed: 5 October 2007)
- U.S. Geological Survey, 2008. Surface Water and Water Quality Models Information Clearinghouse: Table of Model Characteristics. http://smig.usgs.gov/cgi-bin/SMIC/gen_table?dimensions=all&domains=all&constituents=all&models=all&list_gen=SMIChtml (last date accessed: 26 February 2009)
- Van de Griend, A. A., and E. T. Engman, 1985. Partial area hydrology and remote sensing, *Journal of Hydrology*, 81(3-4):211-251.
- Van der Sanden, J. J., K. S. Schmidt, W. Bakker, and W. Bijker, 2001. New environmental remote sensing, *Environmental Modelling with GIS and Remote Sensing*. (A. Skidmore, editor), Taylor & francis.
- Wang, Y., 2004. Using Landsat 7 TM data acquired days after a flood event to delineate the maximum flood extent on a coastal floodplain, *International Journal of Remote Sensing*, 25(5):959-974.
- Wang, Y., J. D. Colby, and K. A. Mulcahy, 2002. An efficient method for mapping flood extent in a coastal floodplain using Landsat TM and DEM data, *International Journal of Remote Sensing*, 23(18):3681-3696.
- Weesakul, S., 1995. Real time flood forecasting modeling in the south of Thailand. <http://www.fao.org/agris/search/display.do?f=/2002/v2802/TH2000003287.xml;TH200003287> (last date accessed: 27 February 2009)
- Wignyosukarto, B. S., 2006. The hydraulic performance of tidal irrigation system in the reclamation of acid sulphate soil. http://bws.staff.ugm.ac.id/wp-content/bs-wignyosukarto-icec2006_b28_.pdf (last date accessed: 7 May 2009)
- Yang, C., C. Zhou, and Q. Wan, 1999. Deciding the flood extent with Radarsat SAR data and image fusion, *Proceeding of the 20th Asian Conference on Remote Sensing*, Hong Kong, China.
- Yang, J., R. D. Townsend, and B. Daneshfar, 2006. Applying the HEC-RAS model and GIS techniques in river network floodplain delineation, *Canadian Journal of Civil Engineering*, 33(1):19(10).
- Yongwei, S., and X. Zong-Guo, 1996. A comprehensive evaluation of filters for radar speckle suppression, *Proceeding of the Geoscience and Remote Sensing Symposium, 1996. IGARSS '96. 'Remote Sensing for a Sustainable Future.'*, International, Lincoln, NE, USA.

Zhang, X. M., C. J. S. Cassells, and J. L. van Genderen, 1999. Multi-sensor data fusion for the detection of underground coal fires, *Geologie en Mijnbouw*, 77(2):117-128.

Zhou, G., J. Luo, C. Yang, B. Li, and S. Wang, 2000. Flood monitoring using multi-temporal AVHRR and Radarsat imagery, *Photogrammetric Engineering & Remote Sensing*, 66(5):633-638.

Zhu, L., and R. Tateishi, 2006. Fusion of multisensor multitemporal satellite data for land cover mapping, *International Journal of Remote Sensing*, 27(5):903-918.

BIOGRAPHICAL SKETCH

Siripon Kamontum was born and raised in Nakhon Ratchasima, a northeastern province in Thailand. She graduated high school from Sura Nari Wittaya and later gained bachelor's degree in Applied Mathematics from Prince of Songkla University, Pattani Campus. In 2000, she finished master's degree in Remote Sensing and GIS from Khon Kaen University and worked as a lecturer at Khon Kaen University, Nongkai Campus for a year. Later, she worked as a Geo-informatics Scientist at GISTDA, Thailand. The Royal Thai Government acting through GISTDA sponsored her to pursue a doctoral degree in a field relating to GIS. She received the doctoral degree in Forest Resources and Conservation concentrated in Geomatics from the University of Florida in the summer of 2009. Upon graduation, she returned to Thailand and works for GISTDA and the gator nation is everywhere.